SANDIA REPORT
SAND2021-10770
Printed August 2021

Sandia National Laboratories

Characterization of Particle and Heat Losses from a High-Temperature Particle Receiver

Clifford K. Ho,[1] Jesus D. Ortega,[2] Peter Vorobieff,[2] Gowtham Mohan,[2] Andrew Glen,[3] Andres L. Sanchez,[3] Darielle Dexheimer,[4] Nathan Schroeder,[5] and Vanderlei Martins[6]

[1]Sandia National Laboratories, Renewable Energy Technologies
[2]University of New Mexico, Department of Mechanical Engineering, Albuquerque, NM
[3]Sandia National Laboratories, WMD Threats and Aerosol Science
[4]Sandia National Laboratories, Atmospheric Sciences
[5]Sandia National Laboratories, Concentrating Solar Technologies
[6]AirPhoton, Baltimore, MD

Prepared by
Sandia National Laboratories
Albuquerque, New Mexico
87185 and Livermore,
California 94550

Issued by Sandia National Laboratories, operated for the United States Department of Energy by National Technology & Engineering Solutions of Sandia, LLC.

NOTICE: This report was prepared as an account of work sponsored by an agency of the United States Government. Neither the United States Government, nor any agency thereof, nor any of their employees, nor any of their contractors, subcontractors, or their employees, make any warranty, express or implied, or assume any legal liability or responsibility for the accuracy, completeness, or usefulness of any information, apparatus, product, or process disclosed, or represent that its use would not infringe privately owned rights. Reference herein to any specific commercial product, process, or service by trade name, trademark, manufacturer, or otherwise, does not necessarily constitute or imply its endorsement, recommendation, or favoring by the United States Government, any agency thereof, or any of their contractors or subcontractors. The views and opinions expressed herein do not necessarily state or reflect those of the United States Government, any agency thereof, or any of their contractors.

Printed in the United States of America. This report has been reproduced directly from the best available copy.

Available to DOE and DOE contractors from
U.S. Department of Energy
Office of Scientific and Technical Information
P.O. Box 62
Oak Ridge, TN 37831

Telephone: (865) 576-8401
Facsimile: (865) 576-5728
E-Mail: reports@osti.gov
Online ordering: http://www.osti.gov/scitech

Available to the public from
U.S. Department of Commerce
National Technical Information Service
5301 Shawnee Rd
Alexandria, VA 22312

Telephone: (800) 553-6847
Facsimile: (703) 605-6900
E-Mail: orders@ntis.gov
Online order: https://classic.ntis.gov/help/order-methods/

ABSTRACT

High-temperature particle receivers are being pursued to enable next-generation concentrating solar thermal power (CSP) systems that can achieve higher temperatures (> 700 °C) to enable more efficient power cycles, lower overall system costs, and emerging CSP-based process-heat applications. The objective of this work was to develop characterization methods to quantify the particle and heat losses from the open aperture of the particle receiver. Novel camera-based imaging methods were developed and applied to both laboratory-scale and larger 1 MW_t on-sun tests at the National Solar Thermal Test Facility in Albuquerque, New Mexico. Validation of the imaging methods was performed using gravimetric and calorimetric methods. In addition, conventional particle-sampling methods using volumetric particle-air samplers were applied to the on-sun tests to compare particle emission rates with regulatory standards for worker safety and pollution. Novel particle sampling methods using 3-D printed tipping buckets and tethered balloons were also developed and applied to the on-sun particle-receiver tests. Finally, models were developed to simulate the impact of particle size and wind on particle emissions and concentrations as a function of location. Results showed that particle emissions and concentrations were well below regulatory standards for worker safety and pollution. In addition, estimated particle temperatures and advective heat losses from the camera-based imaging methods correlated well with measured values during the on-sun tests.

ACKNOWLEDGEMENTS

The authors thank Rip Winckel, Luis Garcia Maldonado, Robert Crandell, Daniel Ray, Roger Buck, Lam Banh, Kevin Good, Benson Tso, Sean Kinahan, Margaret Gordon, Michael Omana, Dora Wiemann, Garth Rohr, Casey Longbottom, RaeAnn Cook, Valerie Sparks, Brent Peterson, Steve Storch, Matthew Tezak, Patrick Burton, Andrea Ambrosini, Christian Pattyn, Swarup China (PNNL EMSL), Zezhen Cheng (PNNL EMSL), Fan Mei (PNNL),Chuyang Chen (Georgia Tech), Guillermo Anaya (UNM), Irma Vazquez (UNM), and Juampablo Heras (UNM) for their support on this project.

This work is funded in part or whole by the U.S. Department of Energy Solar Energy Technologies Office under Award Number 33869.

Sandia National Laboratories is a multimission laboratory managed and operated by National Technology and Engineering Solutions of Sandia, LLC., a wholly owned subsidiary of Honeywell International, Inc., for the U.S. Department of Energy's National Nuclear Security Administration under contract DE-NA0003525.

CONTENTS

1. Introduction and Objectives 12
   1.1. Introduction and Problem Statement 12
   1.2. Objectives 12
   1.3. Overview of Report 12
2. Particle Characterization and Emissions 13
3. Particle Imaging Methods 16
   3.1. Review of Imaging Methods 16
   3.2. Characterizing Particle and Heat Losses 19
   3.3. Laboratory-Scale Testing and Validation 29
   3.4. On-Sun Testing and Validation 50
   3.5. Data and Software Availability 68
   3.6. Summary of Particle Imaging 68
4. Particle Sampling Methods 70
   4.1. Near-Field Sampling 70
   4.2. Far-Field Sampling – Tethered Balloons 82
   4.3. Wind Sector Analysis 95
   4.4. Occupational and Environmental Impact 96
5. Modeling 102
   5.1. Computational Fluid Dynamics Modeling 102
   5.2. AERMOD (EPA Particle Dispersion Modeling Software) 102
   5.3. Modeling Results 104
6. Application to Commercial CSP Plants 109
7. Conclusion and Recommendations 115
   7.1. Particle Imaging 115
   7.2. Particle Sampling 115

References 117

Appendix A. Project Information 119

Appendix B. Milestone Summary and Performance Evaluation Criteria 120

Appendix C. Budget Summary 123

Appendix D. List of Publications from this Work 124

Distribution 125

List of Figures

Figure 1. Two methods to evaluate particle attrition and generation of small particles: particle shaker (a) and dropping column (b). 13

Figure 2. Optical microscopy image of the original particles (left) and SEM images of generated particles (which appear white in the center and right images). 14

Figure 3. Left: Particle fluidization test stand. Right: Image showing particle dust/fines (tan color) particle fragments (black specks), and a larger nominally sized particle. 15

Figure 4. Schematic of the mounting of the cameras with respect to the FPR aperture 16

Figure 5. Left: Sample image of a 7 g/s curtain. Right: Selected region of interest for the calculations cropped in MATLAB. 20
Figure 6. Visualization of the calculation of the difference on the numerator of Eq. 3.4. 21
Figure 7. To estimate the opacity of the curtain, small regions within the ROI (red) are selected, from top to bottom, within the curtain to estimate the opacity. 21
Figure 8. An LX1330B lux meter was used to estimate the opacity of the curtain. The lux meter was mounted in an arm and measurements were taken in 5 different positions. 22
Figure 9. Opacity comparison between Lux measurements and camera methodology 22
Figure 10. The thermogram sequences are imported into MATLAB in the form of 3D matrices. 23
Figure 11. Once the thermograms are imported into MATLAB, the average pixel temperature curve is generated by averaging every row of the matrix and taking the average of those values within all the 2D matrices in the stack. The error bars represent 1σ from the average 23
Figure 12. Left IR pixel with only background. Center: IR pixel with background and a single particle. Right: IR pixel with background and multiple particles 24
Figure 13. Average particle temperature extracted using both models in Eq 3.14 and Eq 3.15. 27
Figure 14. Vector fields obtained for every pair of images in the sequence using in the analysis. 28
Figure 15. Tube furnace used to preheat up to 40 kg of particles equipped with a tilting mechanism to allow the particles to slide into the system once temperature is achieved. 29
Figure 16. Emergency circuit breaker for tube furnace 29
Figure 17. A ±0.5 g resolution scale is being used in place to track the weight change due to the particle flow 30
Figure 18. Flow plate installed above the stainless-steel mesh to enable particle flow. The flow plate is currently controlled using a couple of cables which are pulled from the south side of the test rig. 30
Figure 19. Stainless Steel mesh installed under the nozzle to spread out the flow of particles and generate a more uniform cutain. 31
Figure 20. LED panel was installed to create contrast between the background and the particles. 31
Figure 21. DAQ system wiring of SPR connects all thermocouples and digital scale to the central computers. 32
Figure 22. Two computers are used to monitor and record data from thermocouples, cameras, and digital scale. 33
Figure 23. Left: ImageIR8300 Thermal camera from Infratec. Right: Nikon D3500 with an 18-55mm lens and an 70-300mm lens. 33
Figure 24. The IR and Nikon cameras mounted 5 meters away along with the laptop to capture both images and thermograms. 34
Figure 25: Graphical representation of the numerator calculation on the opacity equation (Eq. 3.4). The red box is the ROI where the particle curtain develops. 35
Figure 26: Graphical representation of the calculation of opacity using Eq. 3.4. The red box is the ROI where the particle curtain develops. 35
Figure 27: Opacity as a function of discharge position for a 6.9 g/s curtain for 200°C preheated temperature. Error bars represent 1 standard deviation of the mean 36

Figure 28: Left: Sample thermogram from the sequences collected for 200°C preheated temperature. The red box represents the ROI which is analyzed on the right. 37
Figure 29: The average pixel temperature profile as a function of discharge position. Error bars represent 1 standard deviation of the mean 37
Figure 30. Schematic of the SPR denoting the location of the thermocouples on the nozzle and the bottom hopper, as well as the flow mesh near the nozzle. 38
Figure 31: Comparison of the empirically derived profile (blue) and the extracted temperatures using the Stefan-Boltzmann's (orange) and Planck's (yellow) model for a preheated temperature of: (top): 200°c, (middle): 450°c, (bottom): 700°c for the region imaged. 39
Figure 32. Sample images for 450°C tests. Left: Sample image of CarboHSP curtain 24.4 g/s. Right: Sample image of sand curtain 17.4 g/s. 40
Figure 33. Average opacity profiles for the CarboHSP particles (left) and Sand (right). 40
Figure 34. Sample images for 450°C tests. Left: Sample thermogram of CarboHSP curtain 24.4 g/s. Right: Sample thermogram of sand curtain 17.4 g/s. 41
Figure 35. Average pixel temperature profile for the CarboHSP particles (left) and Sand (right). 41
Figure 36. Left: Carbo particle curtain preheated to 450°C flowing at 6.4 g/s. Right: Sand particle curtain preheated to 450°C flowing at 3.2 g/s. As observed in the circled region, larger particle agglomerations can be observed in the sand particle curtain. 42
Figure 37. Left: Pixel temperature map of Carbo particle curtain preheated to 450°C flowing at 6.4 g/s. Right: Pixel temperature map of Sand particle curtain preheated to 450°C flowing at 3.2 g/s. Similarly, larger particle agglomerations can be observed in the sand particle curtain which would yield higher pixel temperatures; however, the opposite can be seen in the bottom half of the curtain as lower temperatures were measured. 43
Figure 38. Comparison of particle temperature measured with the thermocouples and the particle temperature extracted applying the methodology developed. 45
Figure 39: correlation of particles within a region of interest to extract vector fields. These vector fields are then converted to velocity based on the reference scale and time between the image pair. 46
Figure 40: Top: establishing the image region of interest for the PIV analysis. Middle: Scaling and calibration of the image. Bottom: image evaluation setting for correlation interrogation window. 47
Figure 41: The velocity as a function of discharge position can be extracted from the vector fields using the pre-specified scaling values. 48
Figure 42: Discharge velocities estimated through PIV at the different temperatures. 48
Figure 43. Left: Image taken with Nikon Camera for a 5.2 g/s curtain. Right: Opacity profile as a function of discharge position. 49
Figure 44. Comparison of Mass Flow Rate measured and Estimated using Equation 3.22. 49
Figure 45. Left: Image taken with Nikon Camera for a 3.5 g/s curtain. Right: Comparison of Mass Flow Rate measured and Estimated using Equation 3.22. 50
Figure 46. Camera enclosure built to protect and mount the cameras. 51
Figure 47. Diagram of cameras mounted with respect to the particle receiver. 51
Figure 48. Wiring diagrams and positioning of the cameras with respect to the particle receiver on top of the tower. The DAQ room is located at the 280 level (20 ft below the roof of the tower) 52

Figure 49. Visible-light image (DSC_0959) obtained during tests at 500 suns. Inlet particle temperature ~430 C and outlet particle temperature ~441 C. Data collected: 12:06 September 4th 2020. 53
Figure 50. Thermogram (200904_120602/ir_data_0001) collected during tests at 500 suns. Inlet particle temperature ~430 C and outlet particle temperature ~441 C. Data collected: 12:06 September 4th 2020. 54
Figure 51. For the analysis, the image is adjusted so the flow of particles is to the positive side of the X-axis. The blue line denotes the top, the green line is the bottom, the orange line is the East side and the yellow line the West side of the FPR aperture. 54
Figure 52. The difference of SSIM between the filtered background and RAW images. 55
Figure 53. Resulting filtered image (right) without particles from the original RAW image (left). 55
Figure 54. Resulting filtered image (right) with particles only from the original RAW image (left). 56
Figure 55. Resulting filtered thermogram (right) without particles from the original RAW thermogram (left). 56
Figure 56. Original RAW thermogram (left) and result of filtering leaving particles only (right). 57
Figure 57. Using the PIVlab setup used in the past for a 10 thermogram sequence we can obtain a velocity field map which then can be used to estimate the average X-velocity. 57
Figure 58. Opacity estimated from visible-light image. The calculations show the values of the opacity at discrete positions along the vertical flow path of the image. Average plume opacity of 1.43%. 59
Figure 59. Pixel temperature estimated from thermogram sets. The calculations show the values of the pixel temperature at discrete positions along the vertical flow path of the thermogram. The error bars represent one standard deviation from the mean value. The mean squared error is calculated spatially (within the 100 mm region) and temporally (on the same region at different times during the experiment). Average pixel temperature of 94.7°C 59
Figure 60. Particle temperature estimated using the methodology developed. The average particle temperature of 402.7°C. The error bars represent one standard deviation from the mean value calculated based on the radiation balance equation. 60
Figure 61. Left: Average instantaneous mass egress rate. The average mass egress rate is 23.9 g/s. Right: Average instantaneous particle heat loss. The average particle heat loss is 9.3 kW for this specific case. 60
Figure 62. Left: Average instantaneous mass flow for the entire 2 minutes of data collection. Total mass loss is 0.63 kg. Right: Average instantaneous particle heat loss for the entire 2 minutes of data collection. Average heat loss 1.4 kW. 61
Figure 63. Average instantaneous total advective losses for the entire 2 minutes of data collection. The total average heat losses are 49.7 kW. 61
Figure 64. Left: Visible-light image sample from the set. Right: Thermogram sample from the set. We can see from the samples that for this case, the particle egress is low. 62
Figure 65. Left: Particle temperature estimated using the methodology developed. The average particle temperature of 546.1°C. The error bars represent one standard deviation from the mean value calculated based on the radiation balance equation. Right: Average instantaneous mass flow for the entire 2 minutes of data collection. Total mass loss is 0.47 kg 62

Figure 66. Left: Average instantaneous particle heat loss for the entire 2 minutes of data collection. Average heat loss 1.3 kW. Right: Average instantaneous total advective losses for the entire 2 minutes of data collection. The total average heat losses are 70.2 kW. 63
Figure 67. Left: Visible-light image sample from the set. Right: Thermogram sample from the set. We can see from the samples that for this case, the particle egress is low. 63
Figure 68. Left: Particle temperature estimated using the methodology developed. The average particle temperature of 492.6°C. The error bars represent one standard deviation from the mean value calculated based on the radiation balance equation. Right: Average instantaneous mass flow for the entire 2 minutes of data collection. Total mass loss is 0.67 kg. 64
Figure 69. Left: Average instantaneous particle heat loss for the entire 2 minutes of data collection. Average heat loss 0.8 kW. Right: Average instantaneous total advective losses for the entire 2 minutes of data collection. The total average heat losses are 74.4 kW. 64
Figure 70. Pareto Chart of Standardize effects for all the factors considered in the Design of Experiments. Factors which have values greater than the reference line display statistical significance. 68
Figure 71: Near Field Particle Instrumentation Placement during On-Sun Testing 71
Figure 72: Wind Rose Depicting Wind Speed and Direction on September 3, 2020 72
Figure 73: Cumulative Mass Size Distributions Measured by the APS for Both the East and West Locations 72
Figure 74: Cumulative Number Size Distributions Measured by the OPC for the Both the East and West Locations 73
Figure 75: Downwind Wind Sector Analysis for the East Monitoring Locations Using Both the APS and OPCs 73
Figure 76: Number Size Distributions Measured by the POPS for Both the East and West Locations 74
Figure 77: APS and OPC Aerosol Size Distributions Measured at Maximum Downwind Concentration Events. 74
Figure 78: Wind Rose of Wind Speed and Direction during the TBS Study on November 3rd, 2020 75
Figure 79: POPS Concentration and Size Data vs. Time (Left) and Total Concentration vs. Time (Right). 75
Figure 80: East OPC concentration vs. time from November 3rd 76
Figure 81. APS mass concentration distributions from the APS instrument (November 3, 2020). 76
Figure 82: Wind Rose Depicting Wind Speed and Direction on March 7th, 2021. 77
Figure 83: Upwind and Downwind Wind Speed and Direction vs. Time. 77
Figure 84: Upwind and Downwind POPS Concentrations vs. Time (Top) and the Receiver Temperature Measurements vs. Time (Bottom). 78
Figure 85: West and East OPC Concentrations vs. Time. 79
Figure 86: APS mass concentration distributions from the APS instrument (April 7th, 2021). 79
Figure 87: PLA Tipping Bucket Design, Preliminary Prototype and Full-Scale Setup. 80
Figure 88: Tipping Bucket Weights vs. Time for September 3rd, 2020. 80
Figure 89: Percentage of Sieved Particle Size Weights from Three Full-Scale Tipping Buckets. 81
Figure 90: Frequency of Tips During September 3rd, 2020 Deployment. 82

Figure 91. Measurement locations during November 3, 2020 TBS deployment. 83
Figure 92: Two-Dimensional Sampling Locations on March 7th, 2021. 84
Figure 93: CPC Concentrations According to Altitude of Upwind and Downwind TBS on November 3rd, 2020 (Left) and March 7th, 2021 (Right). 84
Figure 94: CPC Concentrations with Respect to Time from November 3rd, 2020 (Left) and March 7th, 2021 (Right). 85
Figure 95: CPC Concentrations with Respect to Time from November 3rd, 2020 (Left) and March 7th, 2021 (Right). 85
Figure 96: POPS Data from November 3rd, 2020 (Left) and March 7th, 2021 (Right). 86
Figure 97: POPS Concentrations According to Altitude of Upwind and Downwind Tethered Balloon Systems (TBS) on November 3rd, 2020 (Left) and March 7th, 2021 (Right). 87
Figure 98: 3D Spatial TBS POPS Data Upwind and Downwind on November 3rd, 2020 (Left) and March 7th, 2021 (Right) 87
Figure 99: Wind Rose from November 3rd, 2020 (Left) and March 7th, 2021 (Right). 88
Figure 100: POPS Concentrations with Respect to Time from November 3rd, 2020 (Left) and March 7th, 2021 (Right). 88
Figure 101: Upwind and Downwind OPC Concentrations on November 3rd, 2020 (Left) and March 7th, 2021 (Right). 89
Figure 102: Aerosol size distribution evolution for balloon borne OPCs during the 11/3/21 study 89
Figure 103: Aerosol size distribution evolution for balloon borne OPCs during the 3/7/21 study 90
Figure 104: Size resolved aerosol concentration values and perturbations for the November 3, 2020 data 91
Figure 105: Size resolved aerosol concentration values and perturbations for the March 7, 2020 data. 91
Figure 106: POPS and OPC Size Resolved Concentration Comparison. 92
Figure 107: SEM/TEM Microscopy Image and Energy Dispersive X-Ray Spectra of Particles Collected with STAC. 93
Figure 108: Temporal and Spatial CPC Data in Relation to Concentration. 94
Figure 109: CCSEM chemical composition 95
Figure 110: Wind Sector Analysis for November 3 and March 7 96
Figure 111: Resulting concentrations for the wind sector analysis applied to March 7 data. 96
Figure 112: Mass concentration differences based on the number distribution shown in Figure 104. 98
Figure 113: Mass concentration differences based on the number distribution shown in Figure 105. 99
Figure 114. Simulated small particle (<10 μm) mass fractions in air with a west wind speed of 2 m/s using CFD (top) and AERMOD (bottom) 105
Figure 115. CFD simulation of 350 μm particles emitted from receiver aperture at the NSTTF (0.003 kg/s, 2 m/s west wind). 106
Figure 116. 24-hour maximum emission results from initial AERMOD modeling. 107
Figure 117. Variation of normalized FOV with respect to the focal length 110
Figure 118. Estimated dimensions of a 100 MWth FPR with a 10m x 10m aperture. 111
Figure 119. Comparison of FOV based on the camera system used. Left: ImageIR8300. Right: FLIR One Pro array. 112
Figure 120. IR Cameras consider for the scaled-up system 113

Figure 121. Configurations of cameras with respect to the 100 MWth FPR mounted on 200-meter tower. Left: Configuration with a single IR and Visible-light cameras. Right: Configuration with a 10 IR and 2 Visible-light cameras. 114

LIST OF TABLES

Table 1. Summary of camera-based imaging methods assessed 16
Table 2. Variable correlation study using the 460 cases generated. Values closer to -1 represent a negative correlation, while values closer to 1 represent a positive correlation. 19
Table 3. New exposure settings for Nikon camera used for the on-sun tests 53
Table 4. Table summarizing the three tests for which data is presented. 58
Table 5. Results from regression analysis for the 6 factors selected. $R^2 = 0.203$ 65
Table 6. Results from regression analysis for the 15 compounded factors selected. $R^2 = 0.369$ 66
Table 7. Results from regression analysis for the 14 compounded factors selected. $R^2 = 0.434$ 67
Table 8: Full-Scale Tipping Bucket Results from Each Deployment. 81
Table 9: Instrument Concentration Comparison 92
Table 10: Wind sector analysis from November 3rd, 2020 and March 7th, 2021. 96
Table 11: Summary table of far-field concentration data compared to NAAQS. 99
Table 12: Estimated PEL Values based on OPC measured data. 101
Table 13. Simulated small-particle plume concentration for a 100 MW_e plant using AERMOD with estimated emission rates from tests [14]. 108
Table 14. Simulated small-particle plume concentrations for a 100 MW_e plant using AERMOD with maximum emission rates. 108
Table 15. IR camera dependence on lens chosen for UNM's test rig. 109
Table 16. Field of view of the Nikon camera used at UNM's test rig. 109
Table 17. IR camera with 100 mm lens used to visualize a 10 m HFOV. 111
Table 18. IR camera with 100 mm lens used to visualize a 10 m HFOV. 112
Table 19. Configuration of the Nikon camera used for the scaled-up system. 113
Table 20. Summary of milestones 120
Table 21. Summary of performance evaluation criteria. 120

1. INTRODUCTION AND OBJECTIVES

1.1. Introduction and Problem Statement

Particle receivers are being pursued to enable higher temperatures (>700 °C) and greater power cycle efficiencies (≥50%) for concentrating solar power (CSP) plants [1]. Small sand-like particles fall through a receiver and are heated by a beam of concentrated sunlight. The hot particles can be stored and used when needed for electricity production, process heating, thermochemistry, and solar fuels production. Sandia National Laboratories has previously demonstrated a 1 MW_t high-temperature falling particle receiver system that has achieved particle temperatures over 700 °C [2-5]. The ceramic particles (from CARBO Ceramics) were composed of sintered bauxite and were ~200 – 400 microns in size. Findings from previous studies indicated that direct irradiance of falling particles enabled very high heating rates of the particles, but additional methods to reduce heat losses (convective and radiative) and particle losses were needed to increase receiver thermal efficiencies, reduce costs, and mitigate potential health risks from inhalation of fine particles.

1.2. Objectives

In 2018, the U.S. Department of Energy (DOE) Solar Energy Technologies Office (SETO) Concentrating Solar Thermal Power (CSP) program awarded project 33869 to Sandia to address these needs (see Appendix A for project details). The primary objectives of this work were as follows:

1. Develop imaging methods to characterize particle and heat losses emitted from the aperture of a high-temperature particle receiver
2. Quantify particle emissions using standard air monitoring procedures for comparison to regulatory standards

A milestone summary and list of performance criteria are provided in Appendix B.

1.3. Overview of Report

This report provides a final summary of DOE CSP project 33869. Particle characterization and emissions are first discussed in Section 2. The development of particle-imaging methods is presented in Section 3, including both laboratory-scale and on-sun applications. Near- and far-field particle sampling applications for on-sun testing is presented in Section 4. Modeling of particle emissions using computational fluid dynamics (CFD) and regulatory software is summarized in Section 5. Scale-up of imaging methods for commercial-scale applications is presented in Section 6, and conclusions are drawn in Section 7.

2. PARTICLE CHARACTERIZATION AND EMISSIONS

A series of laboratory experiments were conducted by AirPhoton to separate and characterize the generation of small particles (<10μm) during particle agitation [6]. Small particles are produced by deagglomeration, abrasion and fracture from the larger particle components due to attrition. Both shaking and dropping methods were tested to evaluate the production of small particles using CARBO HSP 40/70 ceramic particles (Figure 1).

In the shaking method, the particle shaker is constantly vibrating the particles at a constant frequency and amplitude, while clean air flushes particles to a cyclone separator that can be tuned to different particle cut-off sizes. The constant particle shaking provides attrition between the particles and produces the deagglomeration of small particles as well as the abrasion and fracture of larger particles into smaller fragments.

In the dropping method, particles are slowly dropped inside a tube from a height of about 1.2 m while being flushed by a constant flow of clean air. The air flow drags the small particles to a cyclone separator ("aerodynamic size separator" in Figure 1) where particles are size selected between 1 to 10μm aerodynamic diameters. The aerodynamic diameter is defined as the diameter of the sphere with unit density that has the same settling velocity as the particle being measured.

Results showed continuous production of small particles in two size ranges: less than 1.3 μm and between 7.5 and 10 μm (aerodynamic diameter). These particles are likely produced by the attrition, fracture and abrasion of the parent CARBO particles. Figure 2 shows optical and scanning electron microscopy (SEM) images of the original particles and generated particles during the shaking/dropping tests. We postulate that the small generated particles (<1 μm) were pre-existing and were attached to the larger parent particles. The small particles can be created during the original manufacturing of the CARBO particles from combustion, gas-to-particle conversion, or molecular nucleation. The deagglomeration of these small particles from the parent particles was caused by collisions during shaking or dropping of the particles. The larger particles (~8 – 10 μm) are produced from mechanical fracturing or abrasion of the original particles. Initial estimates of the generation rate for particles in both size ranges is ~1.4×10^{-5}% of the original mass of the particles per drop inside the laboratory column.

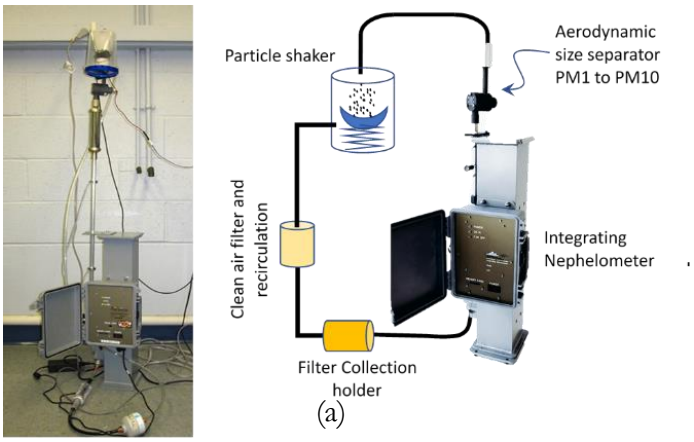

Figure 1. Two methods to evaluate particle attrition and generation of small particles: particle shaker (a) and dropping column (b).

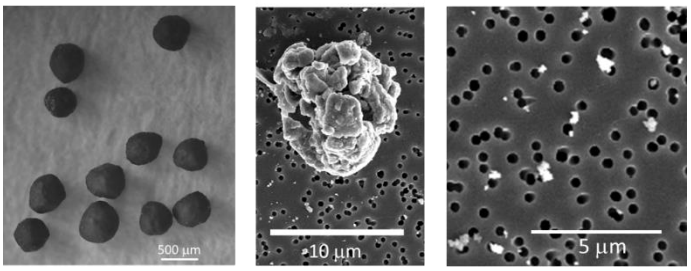

Figure 2. Optical microscopy image of the original particles (left) and SEM images of generated particles (which appear white in the center and right images).

Additional laboratory tests were conducted at Sandia to determine the particle fines composition and production rate during fluidized agitation of CARBO HSP 40/70 sintered-bauxite particles at room temperature [7]. The test apparatus consisted of a 15 cm (6 inch) diameter vertical tube with an attached .37 horsepower blower (Figure 3, left). The blower fluidized 4.5 kg of particles entraining the particle dust to embed in a sock filter at the end of the tube. Particles were fluidized in the "slugging" regime which created a cyclical lifting and dropping of the particles. Air flow in the vertical tube was .6-.7 m/s. The change in mass of the sock filters is measured in 5-hour intervals upon which the filter was replaced. As received particles were fluidized for a total of 275 hours while particles heated to ~550 ° C were fluidized for 200 hours.

The collected dust was analyzed using a Scanning Electron Microscope (SEM) (P. Burton, SNL) to determine size and elemental composition. An X-Ray Diffraction Spectroscope (XRD) was used (A. Ambrosini, SNL) to evaluate crystalline compounds. These measurements were compared to previously generated dust from experiments with particle temperatures ~550 ° C to determine if there were changes in the chemical composition caused by heating. Dust was collected from the walls of the falling particle receiver at the National Solar Thermal Test Facility and analyzed via SEM and XRD as well. The particles in the receiver had been heated to temperatures near 550°C in pervious experiments which deposited the dust. These particle fines were found to be compositionally similar to those generated by the fluidization test. The fines collected from the falling particle receiver were also mainly composed of Corundum and Hematite despite the change in color from tan to a redder tone.

Aerosol sampling probes were placed upstream and downstream of the sock filter while the as-received particles were fluidized. Each probe was connected in parallel to two aerosol samplers, an Optical Particle Sampler model 3300 (OPS) and a NanoScan SMPS Nanoparticle Sizer 3910 (Nano) (M. Omana and D. Wiemann, SNL). The OPS' particle bin sizes ranged from .374 µm to 9.016 µm while the Nano's bin sizes ranged from .0115 µm to .3652 µm resulting in a total detectable range of .0115 µm to 9.016 µm. Samples were collected at one-minute intervals in various test scenarios. A baseline measurement was taken to determine the ambient dust present in the test cell by allowing the blower to run air through the vertical tube without the presence of the particles. Dust generated through the fluidization of the particles was determined as the particles were initially fluidized and after the particles had been fluidized for over 17 hours allowing for the distinction of dust created in manufacturing and dust created through particle abrasion. The 17 hours test was also conducted to determine the change in particle fine size and rate of generation over time. Upstream and downstream probe measurements were then taken to determine the efficiency of the sock filter.

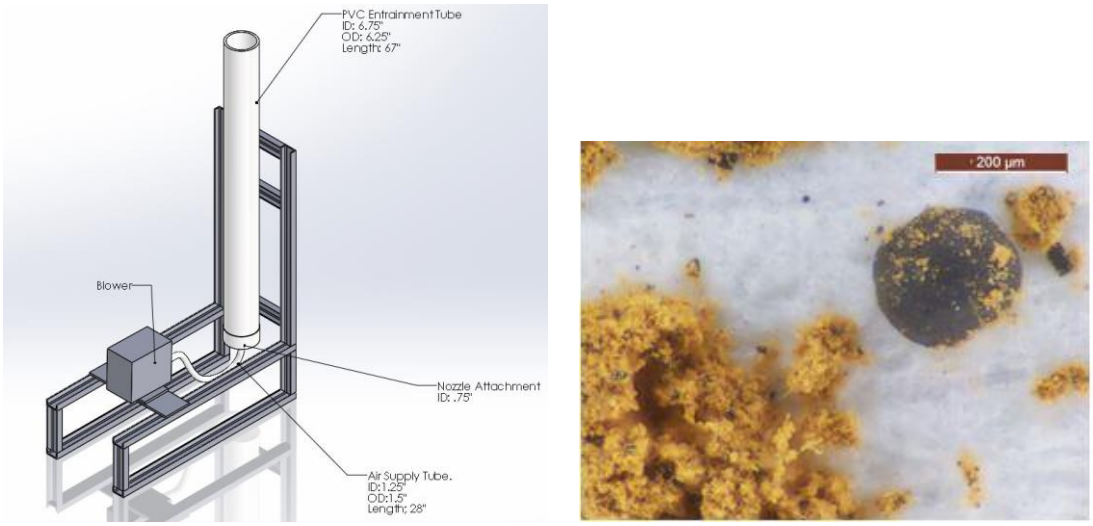

Figure 3. Left: Particle fluidization test stand. Right: Image showing particle dust/fines (tan color) particle fragments (black specks), and a larger nominally sized particle.

Particle fines generated from as-received particles were found to have the same crystallographic composition as particles fines that were heated at temperatures up to 700 ° C despite the heated particle fines shift to a redder color. Optical microscopy revealed that the smaller particle fines and dust (~1 micron) were orange/tan in color (perhaps due to oxidation of iron oxide) and tended to agglomerate. Particle specks (~10 microns) appeared black. Figure 3 (right) shows an image of these different sized particles relative to a nominal particle diameter.

SEM images revealed the elemental composition of the particles. The elemental concentration of the particle fines adjusted for the carbon paper backdrop were: 52.5% Al, 27.5% O, 8.75% Fe, 7.5% Si, 3.75% Ti. Through aerosol sampling, it was found that the majority of the particle fines follow a size distribution with peaks from 0.0205-0.274 µm, at 1.007 µm, and at 1.944 µm. The majority of the particle fine mass was composed of 1.56-5.82 µm particles. After initial fluidization the concentration of particles from 0.0205-.274 µm increased while the concentration of 1.94 µm particles decreased. The decrease in the concentration of larger diameter particles, >1.56 µm, caused a decrease in the rate of particle fine generation by mass. When considering a particle receiver system this decrease in the generation of particle fines may corelate with a decrease in mass loss through the receiver aperture. Previous studies showed that total particle loss during ~200 hours of on-sun test were ~1 – 10 kg/hour, or about 0.006 – 0.06% of the particle mass flow rate through the receiver (4.4 kg/s) [2]. New features are being pursued to reduce the amount of particle and heat losses in next-generation particle receiver systems [8].

3. PARTICLE IMAGING METHODS

3.1. Review of Imaging Methods

One of the main limitations of adding instrumentation close to the aperture is that any hardware would be exposed to the hot particle emissions as well as to the high concentrated irradiance incident on the 1m x 1m falling particle receiver (FPR) aperture. To ensure that the cameras used for the in-situ measurements survive, they must be mounted at a safe distance from the aperture. As we can see in Figure 4, installing the cameras approximately 5 meters away from the aperture will ensure that the cameras are safe from any potential flux spillage.

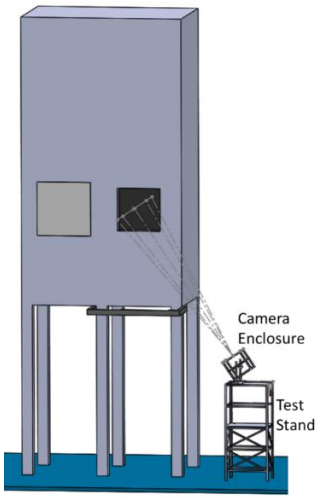

Figure 4. Schematic of the mounting of the cameras with respect to the FPR aperture

Methods Available based on Cameras

To develop a procedure to extract the particle temperature from the data obtained from the images, we must compare the possible approaches that we could pursue. On one hand, the IR camera will provide sets of temperature maps, or thermograms, which will provide an average temperature value of a region. On the other, a visible-light camera will provide sets of images which could be used to quantify the number of particle visible within a region. To determine which approach is the best for our measurements, we must discuss what type of information we could obtain from each image set and how we can use it, while comparing the advantages and disadvantages. These approaches (or methods), along with the tools needed, advantages, and disadvantages are summarized in Table 1.

Table 1. Summary of camera-based imaging methods assessed.

Method	Tools Required	Advantages	Disadvantages
M1: Experimental Correlation	IR cameras (front and side view)	Uses IR cameras only	Requires a large set of experiments and attempts to match thermograms to calibrations
M2: Particle Temperature Estimate	IR cameras (front and side view)	Uses IR cameras only	Relies on estimate of particle temperature from the FPR to calculate opacities
M3: IR Camera with Particle-Pixel Function (PPF)	IR cameras (front and side view)	Uses IR cameras only and development of a	PPF can be difficult to decouple from mass flow rate or opacity

Method	Tools Required	Advantages	Disadvantages
		correlation function based on thermograms only	
M4: Visible and IR Camera Combination	IR cameras and visible camera (front and side view)	Uses IR and visible cameras to obtain pixel a temperatures and opacities	Requires extra cameras
M5: IR Camera with Emissivity Calibration	IR cameras (front and side view)	Uses IR cameras only and variable emissivity values	Qualitatively assess the emissivity values to match temperature profiles

Method 1: Experimental Calibrations

This method requires us to perform a large matrix of experiments to generate some form of experimental calibration using the thermograms only. In the lab-scale experiments, we would measure the mass flow rate and record thermogram sets to estimate the cross-sectional flow area and the particle velocity to get an estimate of particle bulk density. Using the bulk density, we can then estimate the opacity of the curtain; hence estimate the particle temperature from the measured pixel temperature, background temperature, and opacity. However, this will entail generating a large set of experiments with variable mass flow, curtain thickness, and temperatures to generate calibration factors to adjust the temperature ranges. Nonetheless, this calibration will be based entirely on apparent temperature (i.e. pixel temperature – as the following discussion shows, this is problematic).

Method 2: Particle Temperature Estimate

This method would require us to apply the well-known lumped capacitance model to estimate the temperature of the particles expelled from the cavity, using measured inlet and outlet particle temperatures as inputs. However, we would have to somehow validate the particle temperature estimates with the IR camera measurements. Having an estimate of the particle temperature, we can obtain the plume opacity from the energy equation. From the opacity and plume thickness measurement we can obtain the particle volume fraction; hence the bulk density. Knowing the bulk density, the flow area, and extracting the plume velocity we obtain the particle mass flow rate and the corresponding heat loss.

Method 3: IR Camera with Particle-Pixel Function

Ideally, we could estimate the curtain opacity directly from the IR camera by means of a particle-pixel function (PPF) which could infer it from the mass flow rate/opacity. Using the PPF we could get an estimate particle temperature directly from the thermograms. We could then use this temperature to get a curtain opacity from the energy equation by selecting subsections throughout the curtain. From the opacity and plume thickness measurement we can obtain the particle volume fraction; hence the bulk density. Knowing the bulk density, the flow area, and extracting the plume velocity, we get the particle mass flow rate and its corresponding heat loss.

Method 4: Visible and IR Camera Combination

Using a visible-light camera in combination with the IR camera and visualizing the same field of view, we can measure the curtain opacity much better than using the IR camera, as for the latter the pixel value is a representation of the background and particle temperatures and not transmitted light. It is also to our benefit that the visible-light camera has a much higher resolution (up to 24 megapixels), facilitating a greatly improved view of the particle flow. With the opacity values

extracted from the visible-light images, we can match the regions in the visible-light images and thermograms, then estimate average apparent temperatures, and combined with the average opacity on the regions, we can extract the particle temperature through a radiative balance model. Moreover, from the opacity and plume thickness measurement we can obtain the particle volume fraction; hence the bulk density. Knowing the bulk density, the flow area, and extracting the plume velocity we get the particle mass flow rate and its corresponding heat losses.

Method 5: IR Camera with Emissivity Calibration

Using this method entails calibrating the emissivity of the camera used to match particle temperatures to measured pixel temperatures. Similar to Method 1, we will use hot-flow tests to determine correlation between camera emissivity and parameters like background temperature and opacity. In this case, the emissivity value becomes the calibration factor to get the particle temperature from pixel temperature increase with decreasing particle opacity. This makes it possible to determine the correlation between the multiplier and opacity. However, this calibration factor becomes an inverse of the opacity, and since we do not have an opacity value, it can easily become a qualitative measurement to compare thermograms. If the average particle temperature can be inferred, using the average pixel temperatures, the opacity could be estimated. Using the opacity, the volume fraction and bulk density can be estimated as well. Extracting the curtain velocity, we get the particle mass flow rate and its corresponding heat losses.

Method Selection

Because of the large subset of experiments needed to capture a significant number of cases that could occur during the FPR measurements, we decided that Method 1 would not be considered any further. In the case of Method 2, since the initial particle temperature used in the analysis would be an estimate based on the inlet/outlet particle temperatures of the FPR, we also decided against further consideration, unless it was necessary, as we felt necessary to build a methodology completely agnostic from the thermocouple data from the FPR. For Method 5, having to change the effective emissivity value of the IR camera for every measurement to capture a better estimate of the particle temperature would be a tedious task since the variation of effective emissivity will be directly correlated to the particle temperature and opacity on the first place. This is unreliable as the results would be based on a qualitative analysis to capture the data used to calculate the results.

While assessing the remaining two methods, we performed a sensitivity and variable correlation study on the three variables found in the energy equation. A set of 460 analytical cases was generated using the following three equations:

$$f_p = \frac{\dot{m}_b}{\rho_p A_c V_b} = \frac{\dot{m}_b}{\rho_p w_c \tau_c V_b} \tag{3.1}$$

$$\omega_p = 1 - e^{\frac{-3\tau_c \varphi}{2D_p}} = 1 - e^{\frac{-3\dot{m}_b}{2\rho_p D_p w_c V_b}} \tag{3.2}$$

$$\epsilon_{px} T_{px}^4 = (1-\omega_p)\epsilon_B T_B^4 + \omega_p \epsilon_p T_p^4 \tag{3.3}$$

Here φ is the particle volume fraction, $\dot{m}_b$ is the bulk mass flow rate, ρ_p is the particle density, V_b, is the bulk velocity, A_c, is the curtain flow area, w_c is the curtain width, $\tau_c$is the curtain thickness, D_p is the nominal particle diameter, and ω_p is the curtain opacity. For Eq. 3, ϵ is the emissivity, and T is the temperature for the pixel (px), particle (p) and background (B).

While the background temperature (T_b) is kept constant, the influences of particle temperature (T_p) and the particle mass flow rate ($\dot{m}_b$), which directly impacts the opacity (ω_p) of a particle plume, on the pixel temperature (T_{px}) could not be easily decoupled. In the variable correlation study, we generated 460 cases using 23 temperatures from 200°C to 750°C in increments of 25°C and 10 mass flow rates between 0.6 to 6 g/s. The results of this study, displayed in Table 2, show that while the particle temperature shows a higher correlation to the pixel temperature value than the mass flow rate, both values show a positive correlation value above 50%.

This strongly suggests that Method 3 will not be a good candidate as there is a strong coupling between particle temperature, opacity and pixel temperature. Hence, we decided to pursue Method 4 for our procedure development.

Table 2. Variable correlation study using the 460 cases generated. Values closer to -1 represent a negative correlation, while values closer to 1 represent a positive correlation.

Variable Correlation Study

	T_p(C)	$\dot{m}_b$ (g/s)	T_{px}(C)
$\boldsymbol{T_p}$ (C)	1		
$\boldsymbol{\dot{m}_b}$(g/s)	0.0000	1	
$\boldsymbol{T_{px}}$ (C)	0.8169	0.5073	1

3.2. Characterizing Particle and Heat Losses

Having decided on a method, now we needed to develop a procedure to analyze the image sets that the cameras collect. For our measurements, we are using a Nikon D3500 DSLR camera and an ImageIR8300 IR camera to capture images and thermograms simultaneously. As mentioned above, the three quantities that are inter-related are the opacity of the plume, the apparent (pixel) temperature and the true (particle) temperature. The following subsections will explain in detail how the methodology was developed based on the data that we had available. The procedure was developed using MATLAB.

Opacity Estimation

The opacity of a medium can be estimated using Beer's law that states that the opacity, ω, is a function of the light intensities with, I, and without a medium, I_o as seen in equation 3.4.

$$\boldsymbol{\omega = 1 - \frac{I}{I_o}} \tag{3.4}$$

Using the image sets collected by the visible-light Nikon camera, we can complete the estimate the opacity within a region of interest selected as seen in Figure 5. Once this image is processed in MATLAB it is essentially a 16-bit array with intensity values ranging from 0 to 2^{16}-1 which can be handled as a matrix to perform our calculations.

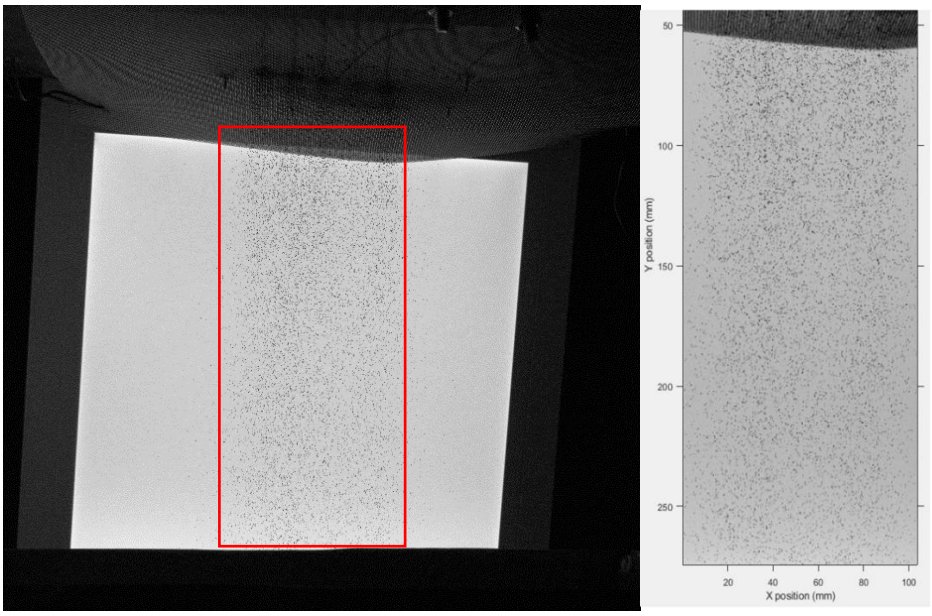

Figure 5. Left: Sample image of a 7 g/s curtain. Right: Selected region of interest for the calculations cropped in MATLAB.

Once the ROI (region of interest) is selected, the computation of Eq. 3.4 can be completed by using a reference image without particles as I_o and the images with particles as I as seen in Figure 6. When the image is then divided by the reference image, the opacity of every single element of the matrix (or pixel) is calculated. In our case, since we are only interested in an average function of opacity as a function of a reference position, we can discretize the resulting image into smaller subsets which we can use to develop a profile as seen on Figure 7. Having an average opacity function allows for simplification in the calculations, as we will see on the next subsection.

Finally, to validate the method used to extract the opacity values, we used an LX1330B lux meter to measure the light intensity variations due to the particle curtain and used Eq. 3.1 to calculate the opacity of the curtain. At two different days, we conducted measurements at different positions by adjusting the location of the arm that it was mounted on as seen in Figure 8. As we can observe in Figure 9, the opacity measurements agree very well in both measurements. There seems to be only one outlier point which is at the top and we believe this is due to the position of the lux meter which could have been closer by the mesh and disrupting the measurements.

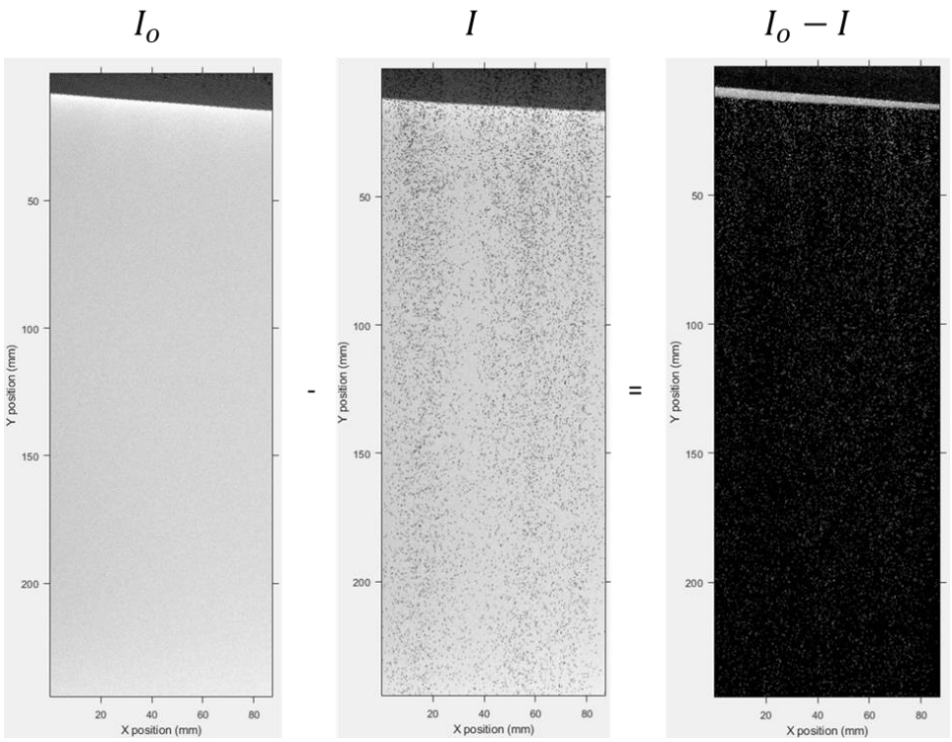

Figure 6. Visualization of the calculation of the difference on the numerator of Eq. 3.4.

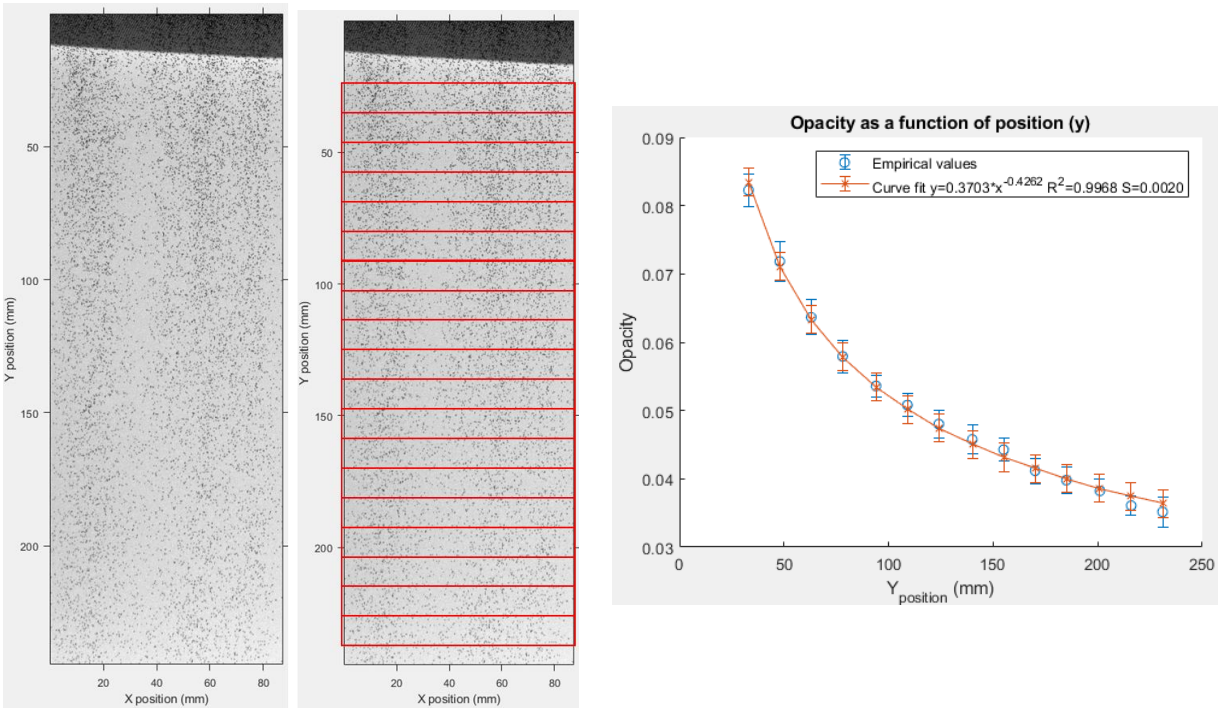

Figure 7. To estimate the opacity of the curtain, small regions within the ROI (red) are selected, from top to bottom, within the curtain to estimate the opacity.

Figure 8. An LX1330B lux meter was used to estimate the opacity of the curtain. The lux meter was mounted in an arm and measurements were taken in 5 different positions.

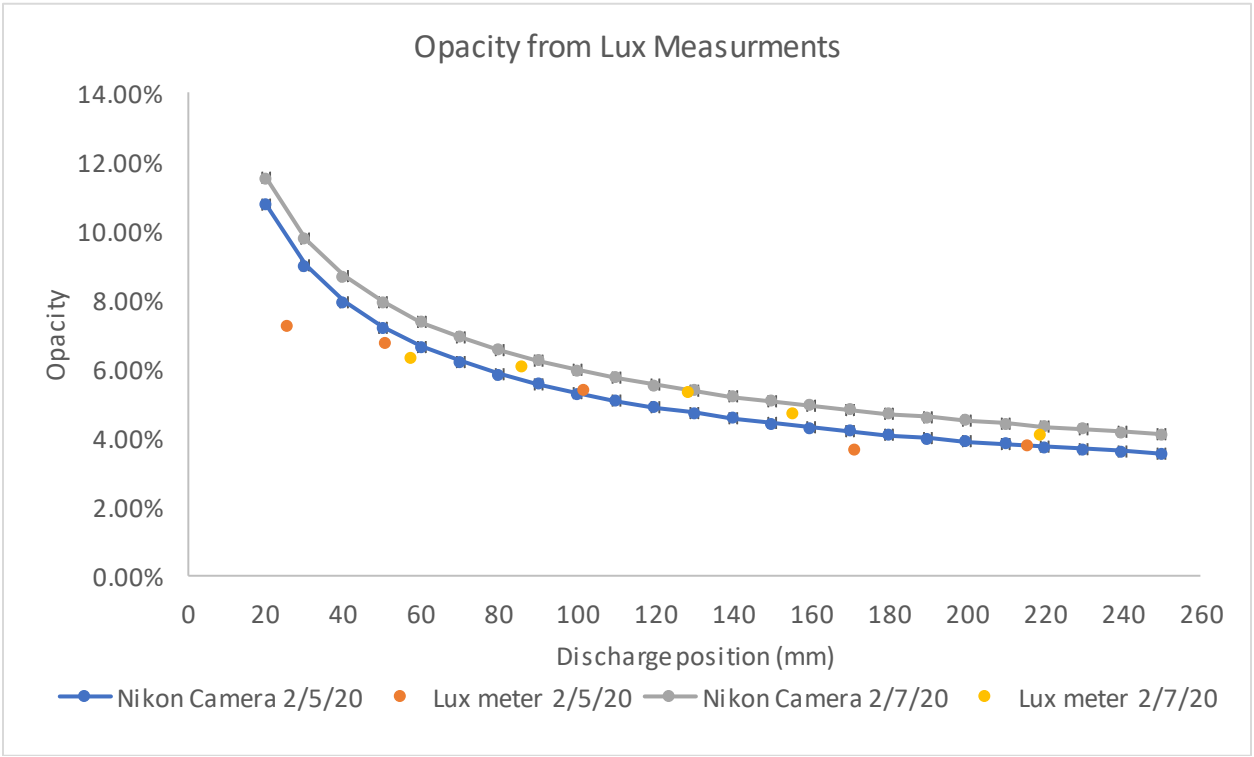

Figure 9. Opacity comparison between Lux measurements and camera methodology.

Apparent Temperature Estimation

In the case of the thermograms, the average pixel temperatures of the same regions can be extracted as a function of discharge position by averaging the entire rows of the matrix as seen in Figure 10 and Figure 11. From here, an average pixel temperature profile can be developed by averaging the profiles obtained for every thermogram on the stack. This average pixel temperature function, along with the average opacity function, can be used to estimate the average particle temperature as a function of discharge position. It should be noted that these temperatures are only apparent temperatures and not the true particle temperatures.

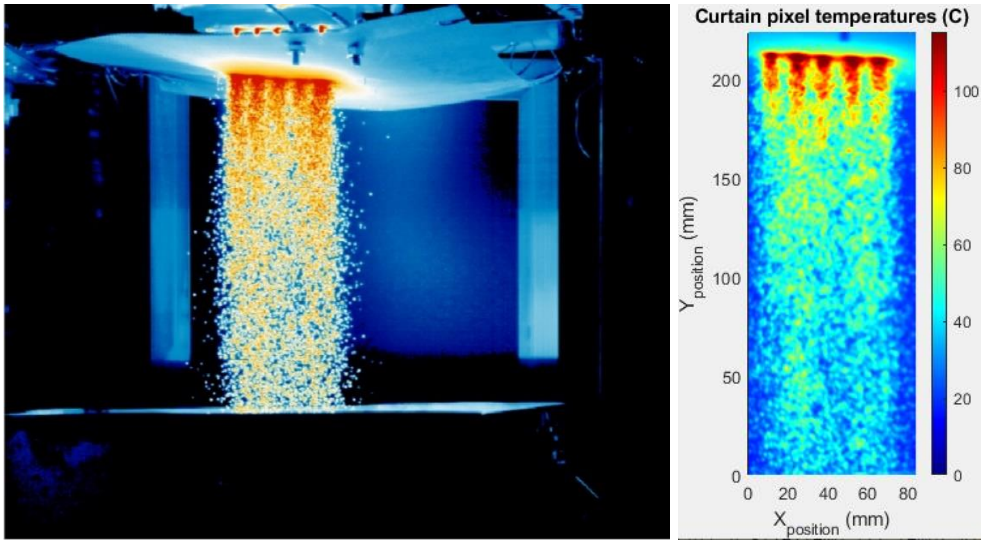

Figure 10. The thermogram sequences are imported into MATLAB in the form of 3D matrices.

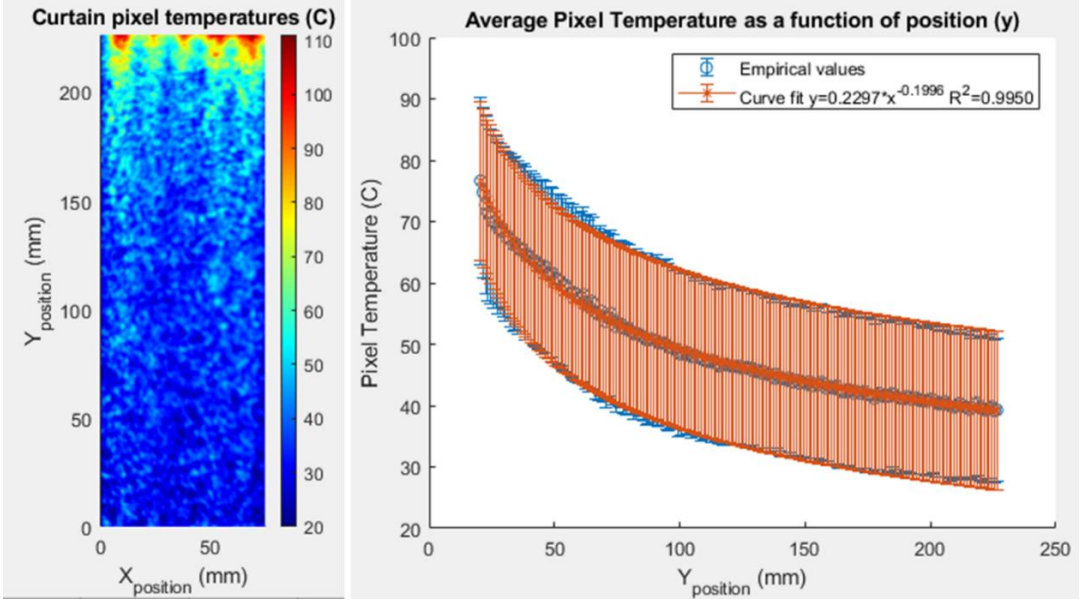

Figure 11. Once the thermograms are imported into MATLAB, the average pixel temperature curve is generated by averaging every row of the matrix and taking the average of those values within all the 2D matrices in the stack. The error bars represent 1σ from the average

Radiation Balance Model

The reason that these pixel temperatures are not the true particle temperatures is that at the mounting distance of 5 meters away from the target, the IR pixels are larger than the mean particle diameter. This means that the irradiance received by a single pixel in the IR camera will be arriving from either the background only, or the background and one or more particles within the pixel as seen in Figure 12. To model the influence of the irradiance collected by the IR pixel, we must consider the effects of the background and particle temperatures. Eq. 3.5 shows a radiation balance model where I is the irradiance and A is the geometric area of the corresponding components: pixel (px), particle (p) and background (b). If we normalize Eq. 3.5 by the pixel area, the irradiance of the pixel becomes a function of the particle and background irradiances and the corresponding area fraction A_f. For our application, we will assume that the area fraction is equivalent to the plume opacity to reach Eq 3.7 as the basis of our model.

$$\boldsymbol{I_{px}A_{px} = I_pA_p + I_bA_b} \tag{3.5}$$

$$\boldsymbol{I_{px} = A_fI_p + (1 - A_f)I_b} \tag{3.6}$$

$$\boldsymbol{I_{px} = \omega I_p + (1 - \omega)I_b} \tag{3.7}$$

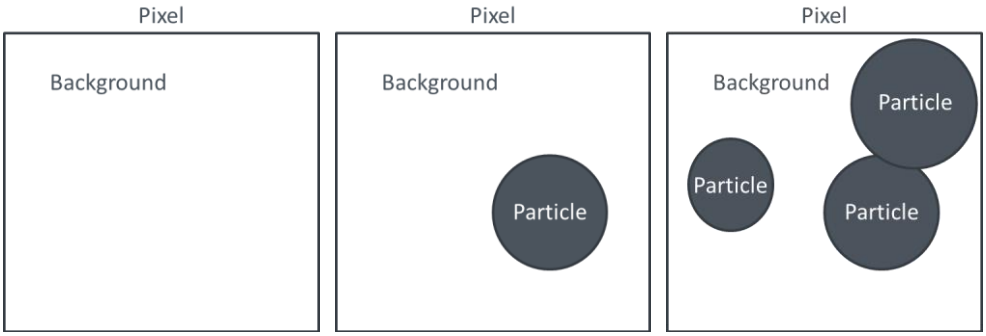

Figure 12. Left IR pixel with only background. Center: IR pixel with background and a single particle. Right: IR pixel with background and multiple particles.

True Particle Temperature Estimation

Now that the average opacity and pixel temperatures are known, the average particle temperature can be found by applying a radiation balance model. Since the average opacity and pixel temperatures are functions of discharge position, the particle temperature will also be a function of discharge position.

Planck's Law

Planck's law describes the spectral density of electromagnetic radiation emitted by a black body in thermal equilibrium, Eq 3.8:

$$\boldsymbol{B} \tag{3.8}$$

Here h is Planck's constant ($6.626x10^{-34}Js$), K is Boltzmann's constant ($1.381x10^{-23}\frac{m^2kg}{s^2K}$), c is the speed of light ($2.998x10^{8}\frac{m}{s}$), λ is the wavelength, and T is the blackbody temperature.

If B is integrated over a predetermined wavelength range, the total hemispherical irradiance can be found from Eq. 3.9

$$\boldsymbol{I = \pi \int_{\lambda 1}^{\lambda 2} B} \tag{3.9}$$

Stefan-Boltzmann's Law

The total hemispherical irradiance over a spectrum range can be estimated by integrating Planck's equation for the entire infinite spectrum (0-∞ μm) as seen in Eq 3.9. The total black-body irradiance can then be expressed as Eq 3.10 where σ is Stefan-Boltzmann constant ($5.6704x10^{-8}\frac{W}{m^2K^4}$).

$$\boldsymbol{I = \sigma T^4 \left(\frac{W}{m^2}\right)} \tag{3.10}$$

Similarly, for a grey-body, the emissivity (ϵ) of the object must be accounted for in Eq 3.11. If the body is assumed to have a diffuse surface, such the case of the CarboHSP particles, the emissivity can be taken as a constant as seen in Eq 3.12.

$$\boldsymbol{I = \pi \int_{0}^{\infty} \epsilon} \tag{3.11}$$

$$\boldsymbol{I = \epsilon \sigma T^4 \left(\frac{W}{m^2}\right)} \tag{3.12}$$

Stefan-Boltzmann's-Law based Model

Plugging in Eq. 3.12 and substituting it into the irradiance model described by Eq. 3.7 we will arrive at the Stefan-Boltzmann's Law-based model shown in Eq. 3.13. Here ω is the curtain opacity, ϵ is the emissivity, and T is the temperature for the pixel (px), particle (p) and background (B).

$$\boldsymbol{\epsilon_{px} T_{px}^4 = \omega \epsilon_p T_p^4 + (1-\omega)\epsilon_B T_B^4} \tag{3.13}$$

Rearranging this Eq. 3.13 and substituting the known values, we can easily solve for the particle temperature (T_p) as shown on Eq. 3.14.

$$\boldsymbol{T_p = \left(\frac{\epsilon_{px} T_{px}^4 - (1-\omega)\epsilon_B T_B^4}{\omega \epsilon_p}\right)^{1/4}} \tag{3.14}$$

Plank's-based Model

On the other hand, if we numerically integrate Planck's equation (Eq. 3.9) for the limited IR camera spectral range of (2-5.7 μm), the irradiance for the pixel and background can be calculated independently. If we substitute Eq. 3.9 into equation 3.7 and rearrange to solve for the irradiance expected form the particles, we get Eq. 3.15. Since the pixel and background values are known, the expected particle irradiance can be calculated, and the average particle temperature is then estimated using a bisection root finding method using the expected particle irradiance as a reference.

$$\boldsymbol{I_p(T_p, \epsilon_p) = \frac{I_{px}(T_{px}, \epsilon_{px}) - (1-\omega) I_b(T_b, \epsilon_b)}{\omega}} \tag{3.15}$$

Bisection Root Finding Method for Temperature Estimation

The particle irradiance based on the Planck's radiation equation (Eq. 3.9) is a function of the particle temperature. Because this value is not known, it can be found numerically by applying a bisection root-finding model.

In this case, we can assume that the minimum particle temperature will be the pixel temperature (T_{px}) which is only possible when the opacity of the plume is 100% (which is not the case) and the maximum temperature was fixed at 1200°C. Assuming the temperature will be anywhere between these two values, the bisection method converges onto a temperature value which will yield the expected particle irradiance.

However, sometimes when the opacity is too low, the particle temperature may not converge due to numerical errors. If this is the case, the temperature calculation is discarded and not used.

Differences between the Stefan-Boltzmann and Planck Radiation Models

To compare these models and validate the application of the numerically integrated Planck's equation against the previously used Stefan-Boltzmann equation we generated a study for a single pixel, as shown above in Figure 12, with the following conditions:

- $T_{px} = 20{:}10{:}300C$ [Pixel Temperature]
- $T_b = 20C$ [Background Temperature]
- $w = 0.025,0.05,0.1$ [Opacity]
- $\epsilon_p = 0.8$ [Particle Emissivity]
- $\epsilon_b = 1$ [Background Emissivity]
- $\epsilon_{px} = 1$ [Pixel Emissivity]

The results in Figure 13 show that the average particle temperature extracted using the numerically integrated Planck's equation yields lower temperatures when compared to the average particle temperatures calculated through the Stefan-Boltzmann equation. This is because the Stefan-Boltzmann's model calculates the total hemispherical irradiance while the Planck's model calculates the spectral hemispherical irradiance for the operating range of the IR camera. These two options to estimate the particle temperature will be explored in further detail in the next section.

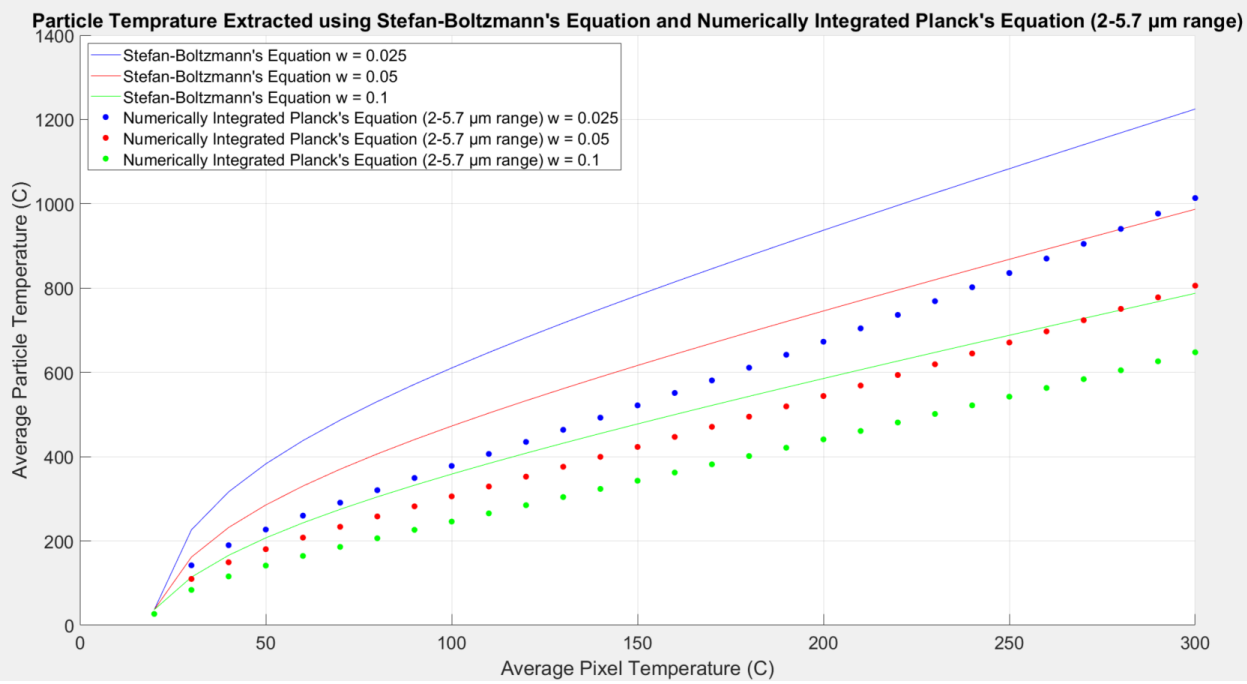

Figure 13. Average particle temperature extracted using both models in Eq 3.14 and Eq 3.15.

Particle Mass Flow Rate Estimation

To estimate the plume mass flow rate, we must define the mass flow rate of the particles within the plume using Eq 3.16:

$$\dot{m}_b = \rho_b A_c V_b \tag{3.16}$$

where ρ_b is the bulk density, A_c is the cross-sectional area of the flow, V_b is the bulk velocity of the flow. As previously shown, the bulk velocity can be extracted from the thermogram sets. Similarly, the cross-sectional area of the flow can be estimated using the images from which the width, w_c, and thickness, t_c, of the plume can be quantified, as shown in Eq 3.17:

$$\dot{m}_b = \rho_b w_c t_c V_b \tag{3.17}$$

Nonetheless, we do not have a direct way to measure the bulk density of the plume. Therefore, if we substitute the bulk density of the plume using Eq 3.18, the mass flow rate becomes Eq 3.19:

$$\rho_b = \varphi \rho_p \tag{3.18}$$

$$\dot{m}_p = \varphi \rho_p w_c t_c V_b \tag{3.19}$$

where ρ_p is the particle density and φ is the volume fraction of the particles within the plume. While we cannot directly measure the particle volume fraction, there are several indirect ways to find this value.

Modified Beer's Law

Beer's Law is a simple ratio that states that the opacity, ω, is a function of the light intensities with, I, and without a medium, I_o, as stated on Eq 3.20:

$$\omega = 1 - \frac{I}{I_o} \tag{3.20}$$

A modified version of this equation was presented by Kim et al. and shows a correlation between opacity, ω, volume fraction, φ, particle diameter, d_p, and curtain thickness, t_c [9]:

$$\omega = 1 - e^{\frac{-3\varphi t_c}{2d_p}} \tag{3.21}$$

Rewriting Eq 3.19 with Eq 3.21, we produce Eq 3.22 which shows the mass flow rate as a function of two constants, the particle diameter and density, and three measurable variables, the plume width, velocity and opacity:

$$\dot{m}_p = \frac{-2}{3} d_p \rho_p w_c V_b ln(1-\omega) \tag{3.22}$$

Particle Velocity

The particle velocity of the plume can be estimated using particle image velocimetry (PIV) analysis tools such as PIVlab, which is a MATLAB toolbox. Taking the thermogram sets and processing them in PIVlab (Figure 14) allows us to get a velocity vector field; hence obtaining an average velocity profile as a function of discharge position.

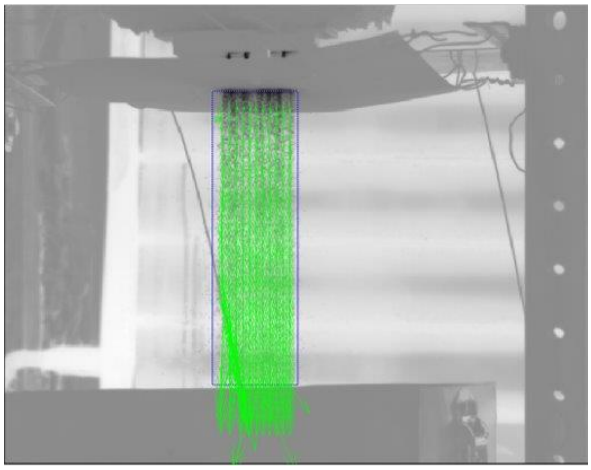

Figure 14. Vector fields obtained for every pair of images in the sequence using in the analysis.

Particle Heat Flow Rate Estimation

Calculating the particle mass flow rate using Eq. 3.22, and knowing the particle temperature from the previous subsection, we can use Eq. 3.23 to calculate the heat flow of the particles. Here the heat capacity of the particles (Cp_p) and ambient temperature (T_{amb}) are known quantities.

$$\dot{Q}_p = \dot{m}_p \int_{T_{amb}}^{T_p} Cp_p(T) dT \tag{3.23}$$

3.3. Laboratory-Scale Testing and Validation

Test Setup at UNM

To validate the methods described above, a lab-scale test setup was developed at the University of New Mexico solar simulator lab. A bench-scale test small particle receiver (SPR) was built and instrumented for the evaluation of the camera imaging procedures.

Particle Preheating Furnace

Prior to the particle receiver operation, a pre-set of mass of particles is preheated to the prescribed temperature of interest for the test. To prepare for the test, we use a GHA 12/1200 7 kW tube furnace from Carbolite-Gero (Figure 15). The furnace was equipped with a custom-built mechanism allowing it to tilt to a specific angle, letting the particles slide out of the furnace once the temperature of interest is achieved. The furnace is located near the SPR and can be aligned with the top hopper of the SPR. The tube furnace is sitting on a steel table and has been attached to an 850 lb. actuator which is capable of tilting the furnace up to 30 degrees as shown in Figure 15b. The furnace controller is installed on the southwest corner of the test frame (Figure 16) and will enable the operator to tilt the furnace without being inside the testing rig. The emergency circuit breaker shown in Figure 16 was installed on the outside of the test rig to interrupt power to the furnace in the event of emergency. The furnace is loaded with a predetermined amount of material which must undergo a dwell cycle to heat the material up to a preset temperature.

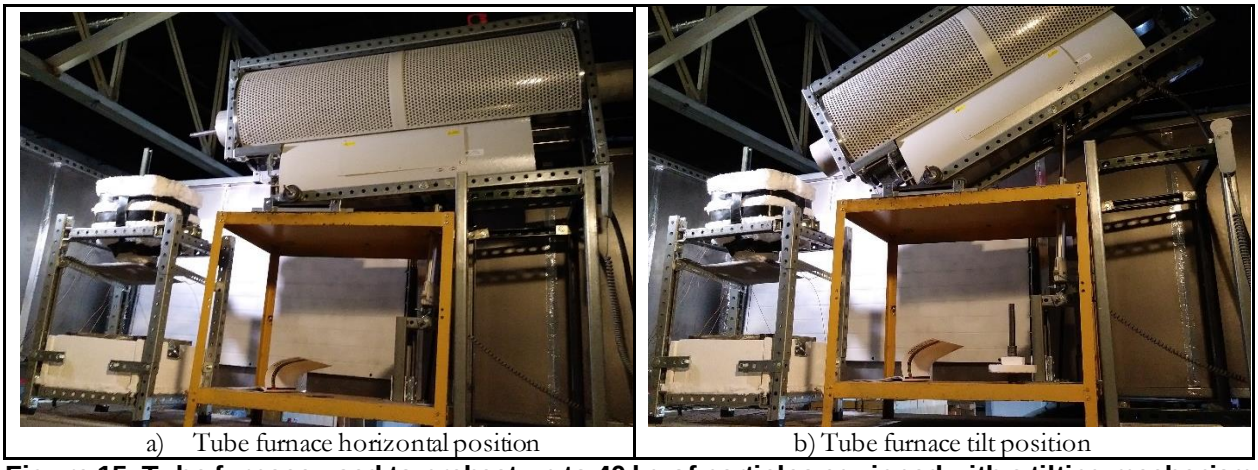

a) Tube furnace horizontal position

b) Tube furnace tilt position

Figure 15. Tube furnace used to preheat up to 40 kg of particles equipped with a tilting mechanism to allow the particles to slide into the system once temperature is achieved.

Figure 16. Emergency circuit breaker for tube furnace

Once the cycle is completed, the furnace is opened and is tilted until the material fills the top hopper of the FPR.

Experimental Test System

The SPR system had to be modified because the load cells that were used originally did not have enough resolution (±25 g) to capture the required flow rates of ~10-100 g/s. A ±0.5 g resolution scale was installed in place of the load cells where the bottom hopper was sitting as shown in Figure 17. The current scale has a weight limit of 15 kg, but will be replaced with a 40 kg scale once we receive it. The bottom hopper is equipped with four thermocouples and will be insulated. The scale connects to the data acquisition system through a serial RS-232 connection.

Figure 17. A ±0.5 g resolution scale is being used in place to track the weight change due to the particle flow.

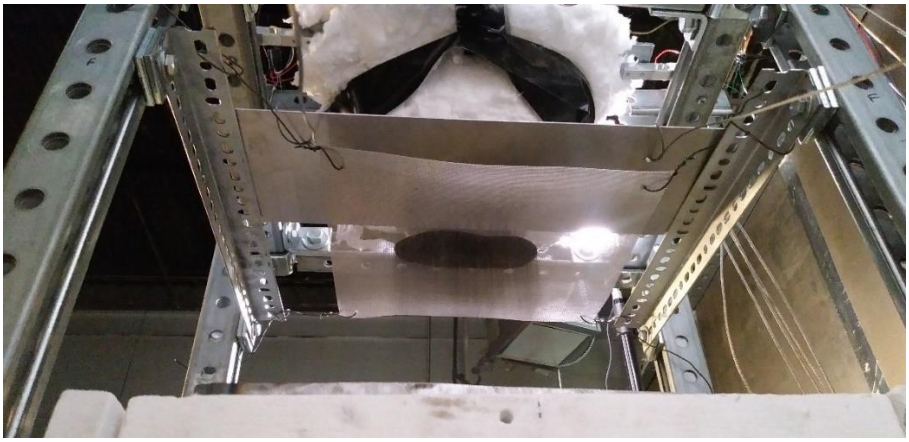

Figure 18. Flow plate installed above the stainless-steel mesh to enable particle flow. The flow plate is currently controlled using a couple of cables which are pulled from the south side of the test rig.

To hold the hot particles on the top hopper, a sliding gate (Figure 18) was installed under the nozzle. This gate is operated using a set of cables which are pulled from the south side of the test rig. Because the gate only enables particle flow, a different method to restrict the particle flow was implemented. A flow control mesh (Figure 19) was installed on the FPR to further reduce particle

flow and create spatial and temporal variability. A large LED panel was installed to create a large contrast between the background and the particles flowing (Figure 20).

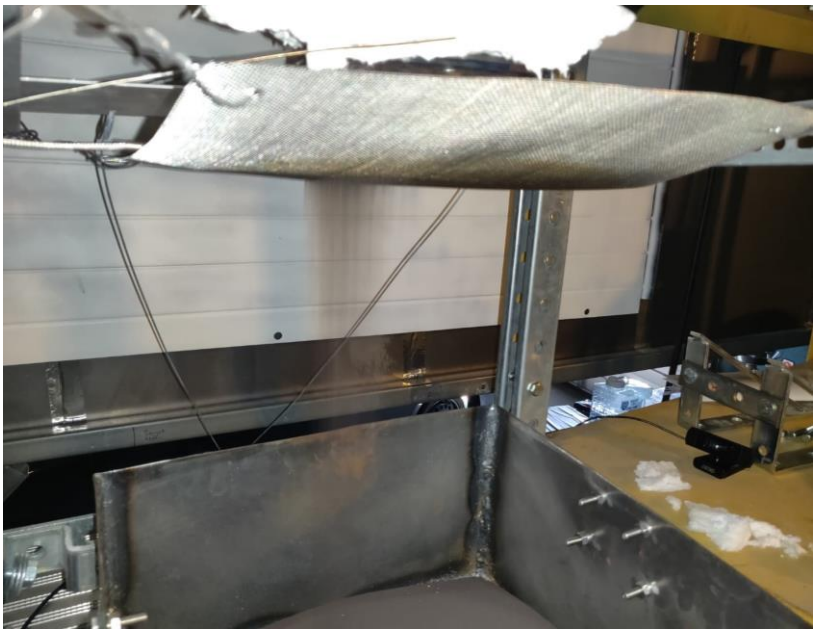

Figure 19. Stainless Steel mesh installed under the nozzle to spread out the flow of particles and generate a more uniform cutain.

Figure 20. LED panel was installed to create contrast between the background and the particles.

Data Acquisition Systems

A data acquisition (DAQ) system has been designed to accommodate 24 thermocouples (15 on the SPR and 9 on the Solar Simulator) and a digital scale that connect to our central control computers as it can be seen in Figure 21 and Figure 22. Moreover, two cameras have been installed for monitoring of the experiment and to capture snapshots of the curtain thickness, which are synchronized to the image capturing of the IR camera.

The second DAQ system is comprised of the IR camera, a 10-Gigabit data transfer system and a laptop which provides controls and storage for the data captured. The IR camera has been positioned on the West side of the test rig for the initial measurements. The cameras are positioned to be as perpendicular to the SPR aperture as possible, while maintaining a 5 m distance between the camera and the particle curtain. The two cameras are an ImageIR8300 capable of capturing thermograms of the plume at 300 frames per second at a resolution of 640x512 for a temperature range between -10°C and 1200°C and a Nikon D3500 with a 24 MP resolution (6000x4000) equipped with a 70-300mm lens which is capable of recording at 33 frames per minute (Figure 23). The positioning of both cameras with respect to the SPR test rig can be seen in Figure 24.

Figure 21. DAQ system wiring of SPR connects all thermocouples and digital scale to the central computers.

Figure 22. Two computers are used to monitor and record data from thermocouples, cameras, and digital scale.

Figure 23. Left: ImageIR8300 Thermal camera from Infratec. Right: Nikon D3500 with an 18-55mm lens and an 70-300mm lens.

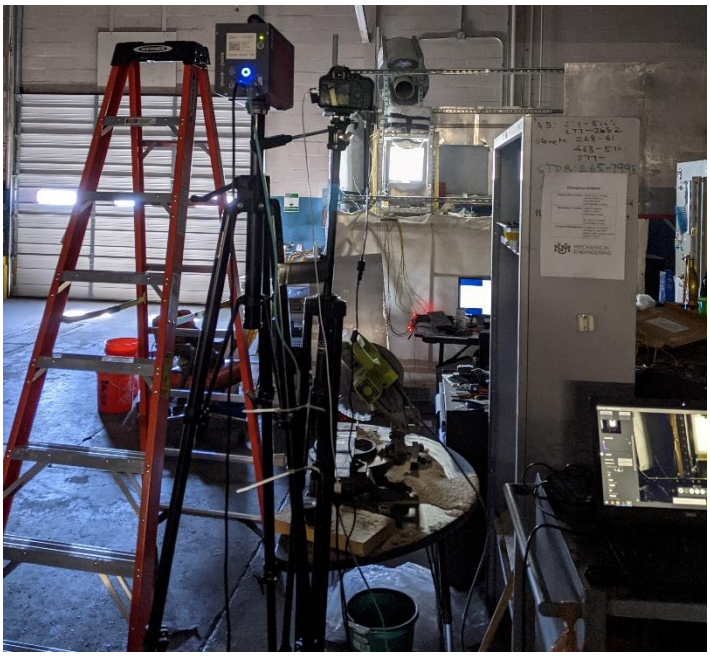

Figure 24. The IR and Nikon cameras mounted 5 meters away along with the laptop to capture both images and thermograms.

Lab-scale Tests and Results

Using the test setup described, the team prepared a series of tests to validate the effectiveness of the methodology developed. The tests prepared had a variable preheat temperature of that varied between 100-750°C and an approximate mass flow rate of ~ 7 g/s.

Opacity

As described by before, the opacity of the curtain is calculated by the opacity Eq. 3.4. We are required to have a background image as a reference without particles in order to perform the calculations. We should remember that these RGB images are converted to grayscale in order to yield a 16-bit image which is a large matrix where every pixel that contained an RGB value, now contains an intensity value between 0 (black) to 65,535 (white).

To calculate the average opacity, first, the image with particles is subtracted from the image without particles (i.e. reference) which yields an image with high values of pixels where the particles are located, as shown in Figure 25. When the resulting image is divided by the reference image as seen in Figure 26, the opacity values in it will range from 0 to 1. Taking the mean across all the columns within the region of interest (the boxed region in red where the flow mesh does not interfere) will yield a set of mean-opacity data points with their respective standard deviations, which can then be curve fitted to produce an opacity profile as a function of discharge position as shown in Figure 27. It should be noted that this procedure does not involve converting the images into a binary form as this will introduced an error based on the threshold applied. We found that the opacity of the curtain doesn't seem to be affected by the temperature of the particles.

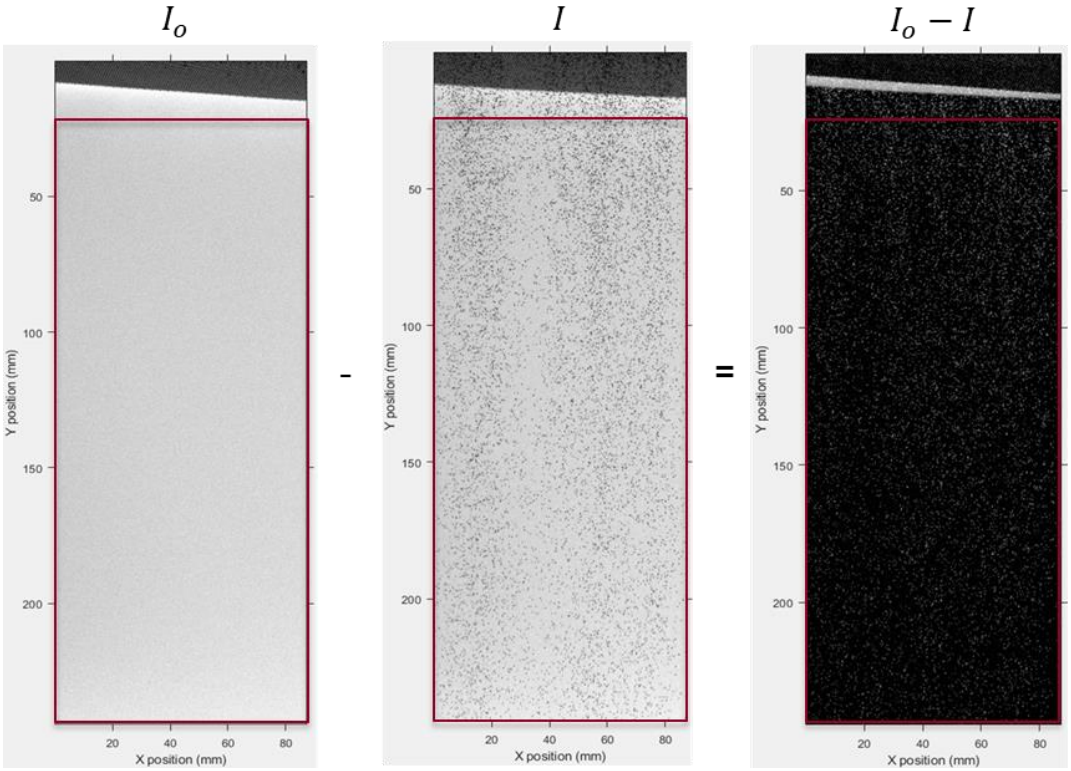

Figure 25: Graphical representation of the numerator calculation on the opacity equation (Eq. 3.4). The red box is the ROI where the particle curtain develops.

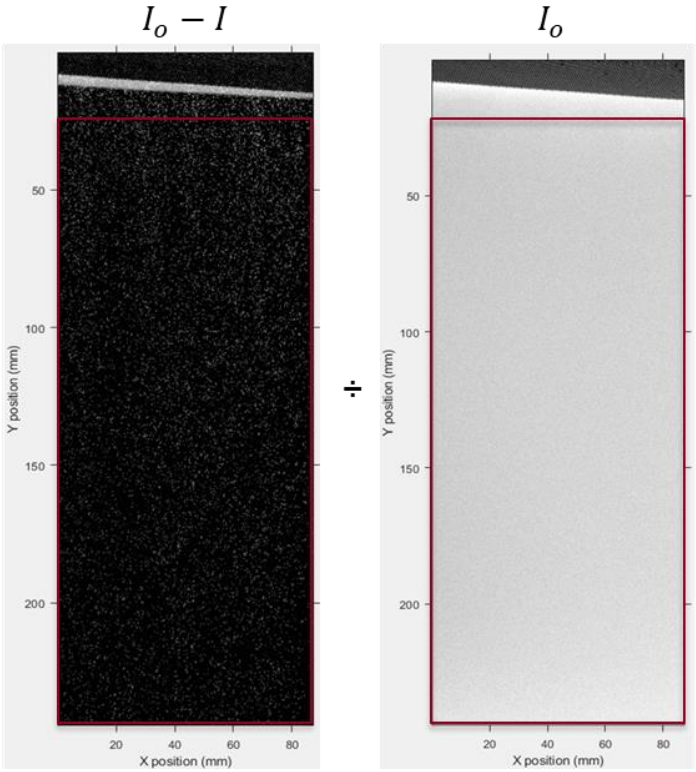

Figure 26: Graphical representation of the calculation of opacity using Eq. 3.4. The red box is the ROI where the particle curtain develops.

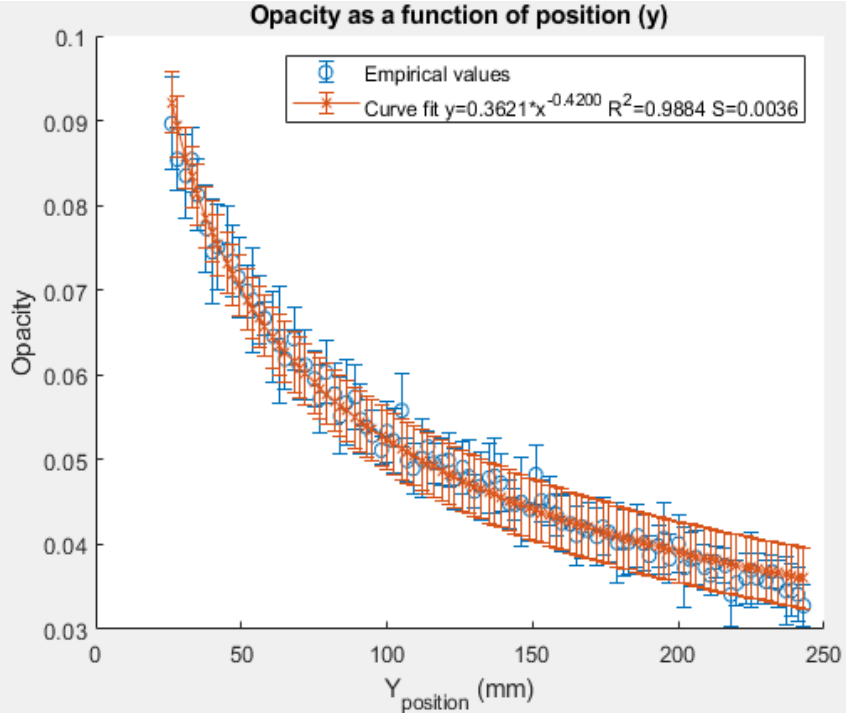

Figure 27: Opacity as a function of discharge position for a 6.9 g/s curtain for 200°C preheated temperature. Error bars represent 1 standard deviation of the mean.

Pixel Temperature Results

Similar to the images, the thermograms are essentially matrices with temperature values. This makes the calculations easier to complete. To develop a pixel temperature profile as a function of discharge position, first, a region of interest (ROI) must be selected as seen on Figure 28. Now, the pixel profile as a function of discharge position is obtained by averaging every row of pixel temperature values. By averaging every row within a single thermogram, the average pixel temperature spatial profile can be obtained. However, since we have multiple thermograms per sequence a temporal average (i.e. the average of the average pixel temperature) profile can be obtained. To account for the error in the calculation, the mean squared average is calculated to find the standard deviation as seen on Figure 29.

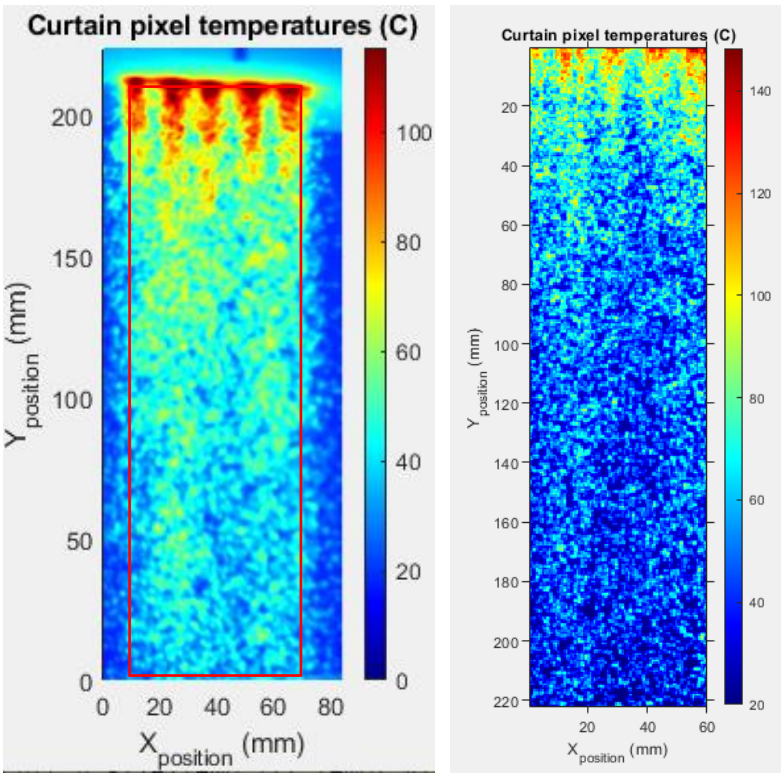

Figure 28: Left: Sample thermogram from the sequences collected for 200°C preheated temperature. The red box represents the ROI which is analyzed on the right.

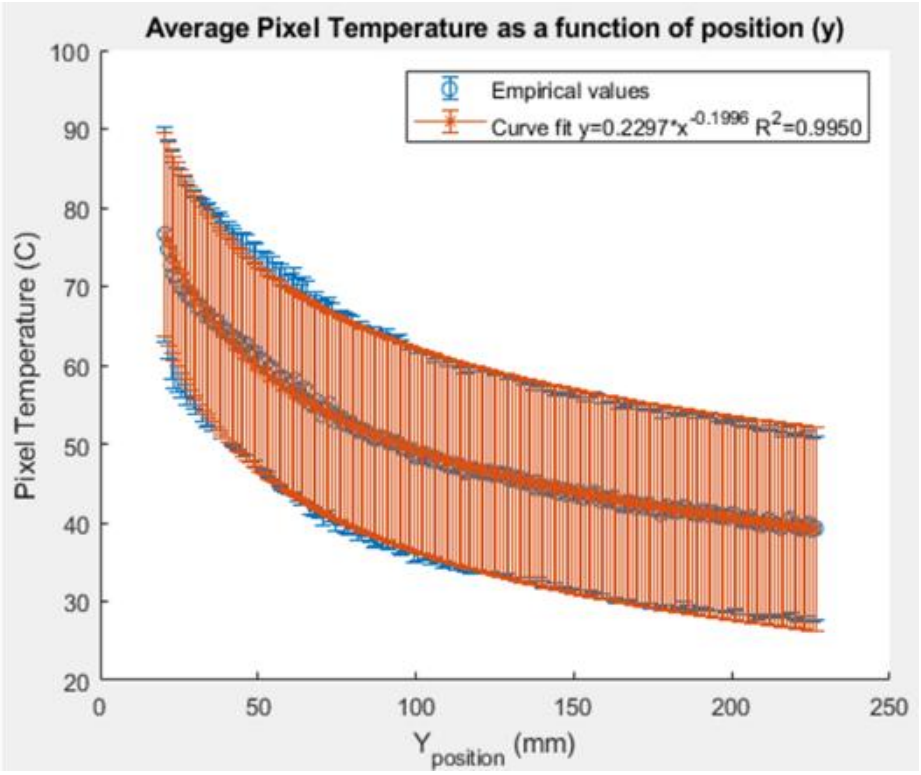

Figure 29: The average pixel temperature profile as a function of discharge position. Error bars represent 1 standard deviation of the mean.

Particle Temperature Results

Applying the methodology described by Eqns. 3.14 and 3.15, the average particle temperature as a function of discharge position can be obtained. It should be noted that the average particle temperature values we obtain represent the temperature that the particle or particles within the pixels at any given discharge position must be to meet the irradiance balance equation requirements. To validate the methodologies presented, the average particle temperatures extracted through both models are compared with the semi-empirical particle temperatures calculated using a lumped capacitance exponential decay model for a single particle using the temperatures recorded at the top and bottom hoppers. As seen on the Figure 30, the aperture region is about 250 mm but the bottom hopper thermocouples are below this region; thus, we derived a semi-empirical curve based on these two thermocouples and select only the aperture region for the comparison.

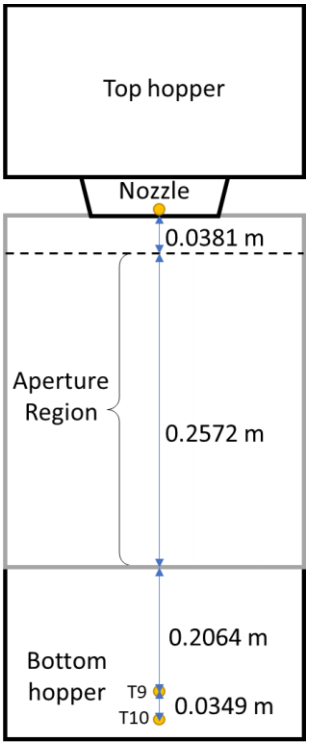

Figure 30. Schematic of the SPR denoting the location of the thermocouples on the nozzle and the bottom hopper, as well as the flow mesh near the nozzle.

Figure 31 suggests that there are two major effects that can be observed. First, as expected, applying the Stefan-Boltzmann model (SBM) overestimates extracted temperatures when compared to the Planck's model (PM). Similarly, while the low and medium temperature curves align well with the temperature profiles extracted with the Planck model, the extracted values at high temperature remains higher than the empirical curve. Presently, the source of discrepancy has yet to be identified.

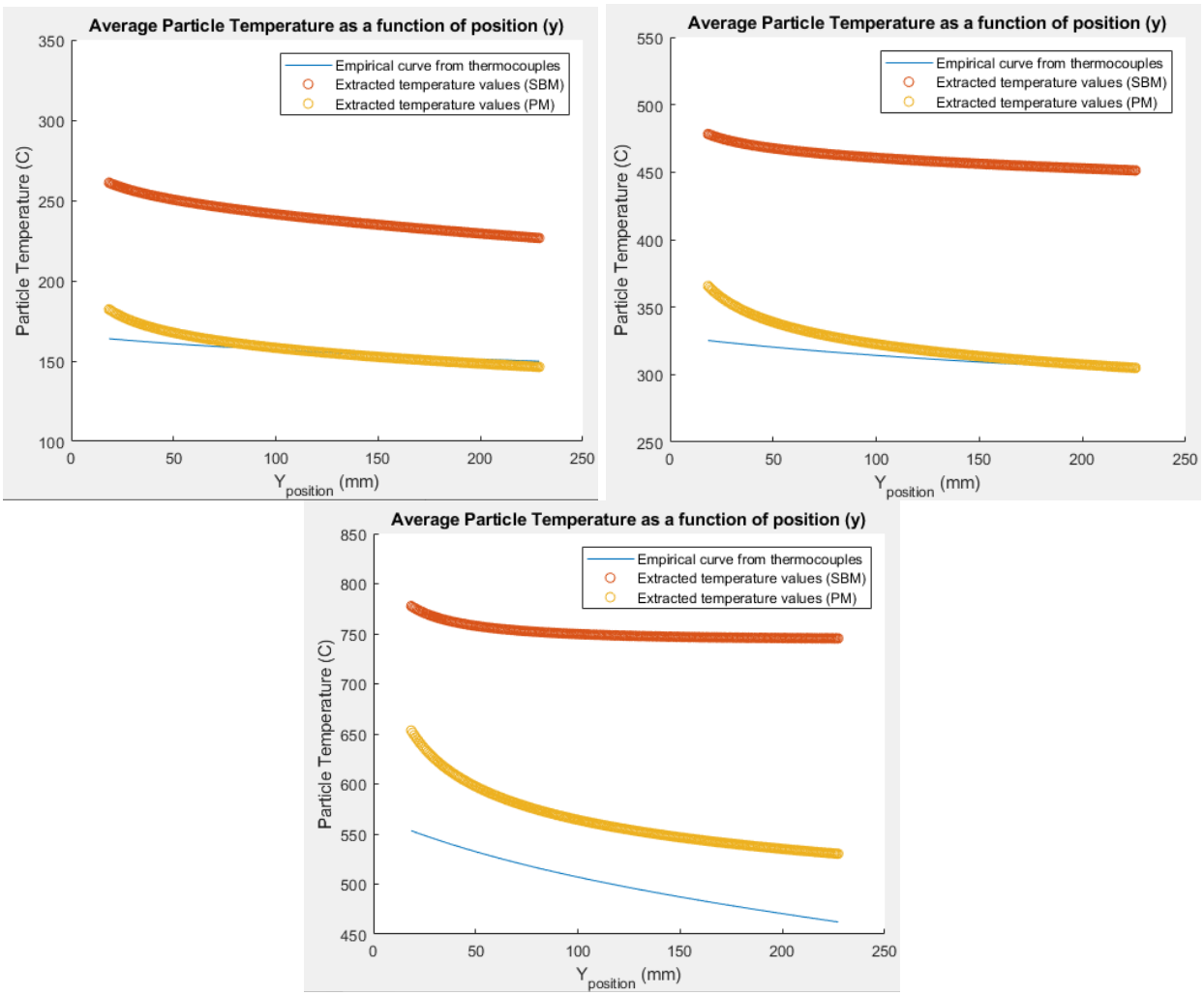

Figure 31: Comparison of the empirically derived profile (blue) and the extracted temperatures using the Stefan-Boltzmann's (orange) and Planck's (yellow) model for a preheated temperature of: (top): 200°c, (middle): 450°c, (bottom): 700°c for the region imaged.

While these measurements were completed for the CarboHSP particles, a set of measurements were performed using playground sand to evaluate the effectiveness of the methodology on a different particle type and size distribution. Common sand was chosen because of its large particle size distribution and variable shape and form to compare with the nearly spherical Carbo HSP 40/70 particles used which have a very constant average particle diameter. Because of the large size distribution of sand, we sieved out particles larger than 1 mm in diameter to avoid any clogs in the system while flowing. The sand particles yield a much higher opacity profile while maintaining a lower particle mass flow rate as seen on Figure 32 and Figure 33. This may seem counterintuitive, but curtains with smaller particle diameters tend to be more opaque for similar mass flow rates since more smaller particles are required to maintain the same bulk density.

On the other hand, the pixel temperatures shown on Figure 34 and Figure 35 appear to be the same for both Carbo HSP and Sand. While they were preheated to the same temperature for the same amount of time, the second half of the sand curtain appears to be cooling faster than the Carbo HSP

curtain. This correlates once again to the particle size distribution. While CarboHSP particles appear to maintain a uniform shape on the thermograms, we can see that the sand particles do not; which suggests that the particles are cooling faster. The most reasonable explanation for this is that smaller particles are losing heat faster than the larger ones due to the increase in the surface area of the bulk of particles.

During the post processing of the data presented, the team identified possible measurement issues preventing us from completing the particle temperature extraction and analysis. The team decided to recreate the tests from the previous lab-scale testing runs using a flow mesh to spread the curtain and create curtains with low opacities.

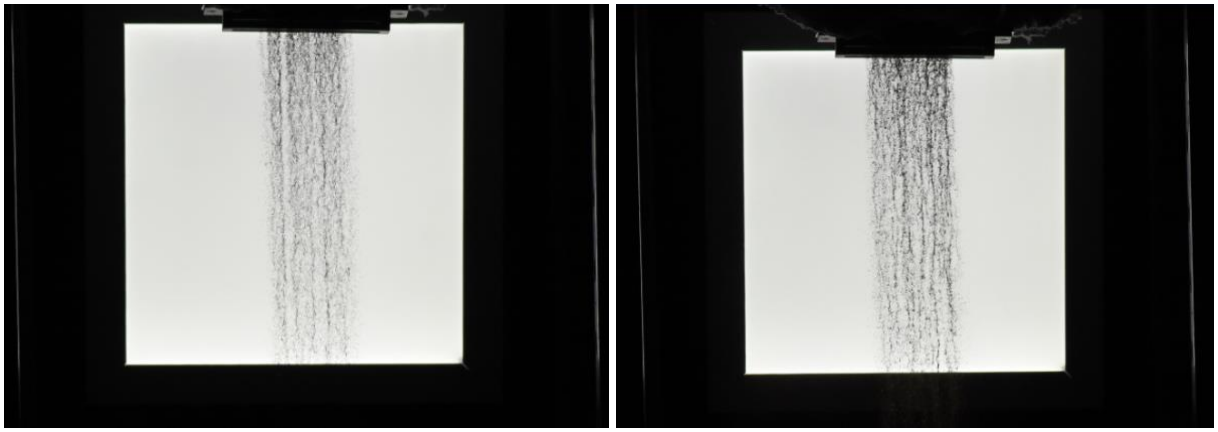

Figure 32. Sample images for 450ºC tests. Left: Sample image of CarboHSP curtain 24.4 g/s. Right: Sample image of sand curtain 17.4 g/s.

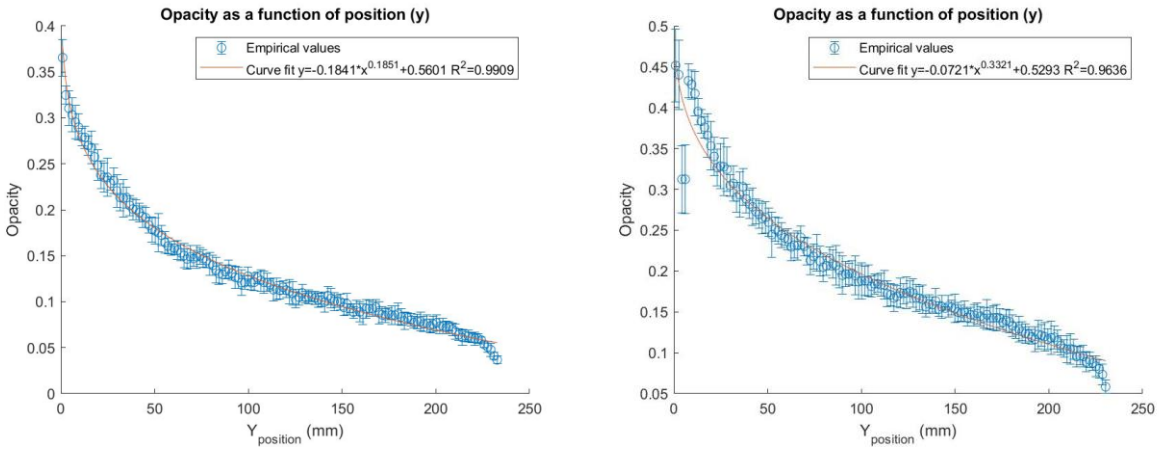

Figure 33. Average opacity profiles for the CarboHSP particles (left) and Sand (right).

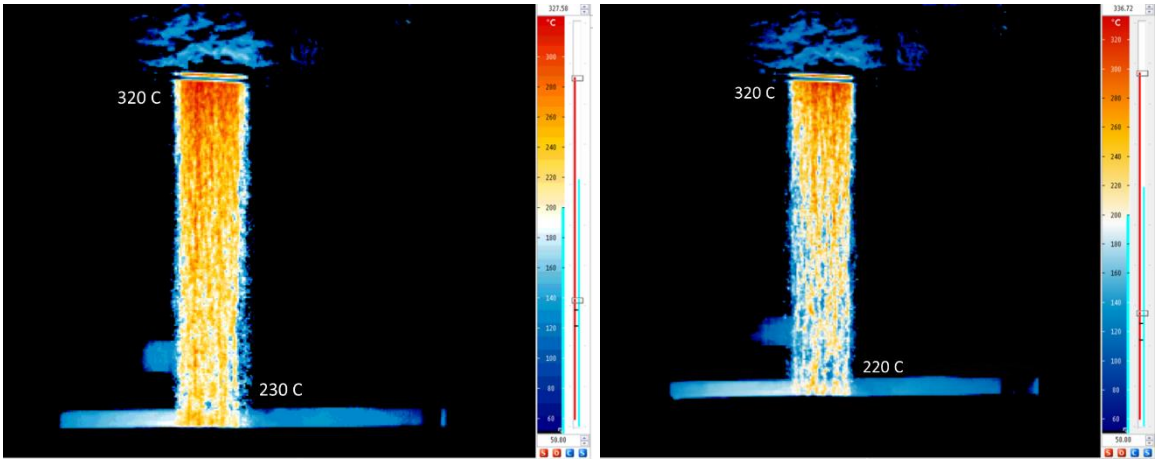

Figure 34. Sample images for 450°C tests. Left: Sample thermogram of CarboHSP curtain 24.4 g/s. Right: Sample thermogram of sand curtain 17.4 g/s.

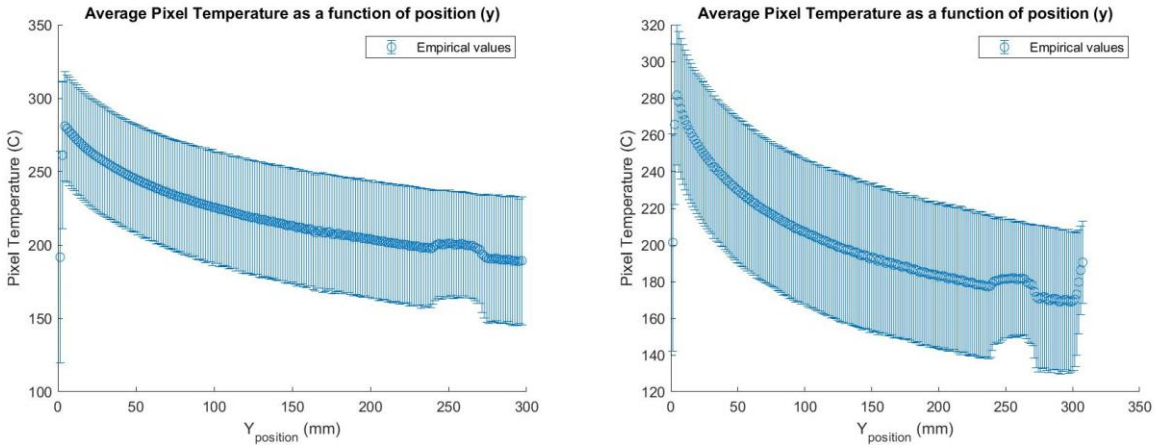

Figure 35. Average pixel temperature profile for the CarboHSP particles (left) and Sand (right).

The tests using Carbo and Sand particles were completed using a flow mesh to spread the particle flow. However, we were unable to complete the test for sand at 750°C because the particles clogged the tube furnace while it was hot. We tried multiple approaches to push the particles out of the furnace. We noticed that the sand particles were discharging at a lower rate than the carbo particles (Figure 36) which was another indicator that playground sand has much different flow properties than Carbo particles. Moreover, particle agglomeration is more common and accentuated with sand, which can be detrimental to the opacity of a curtain. The agglomerations yield different pixel temperature maps as seen in Figure 37. Nonetheless, the particle temperature methodology was successfully applied to the 5 cases that we compared as seen in Figure 38. While the data points from the extracted temperature have a wider spread, we can see a definitive trend which resembles that of the empirical temperature curve. From this, we can conclude that the particle temperature extraction method we developed is robust, regardless of particle type, shape or size.

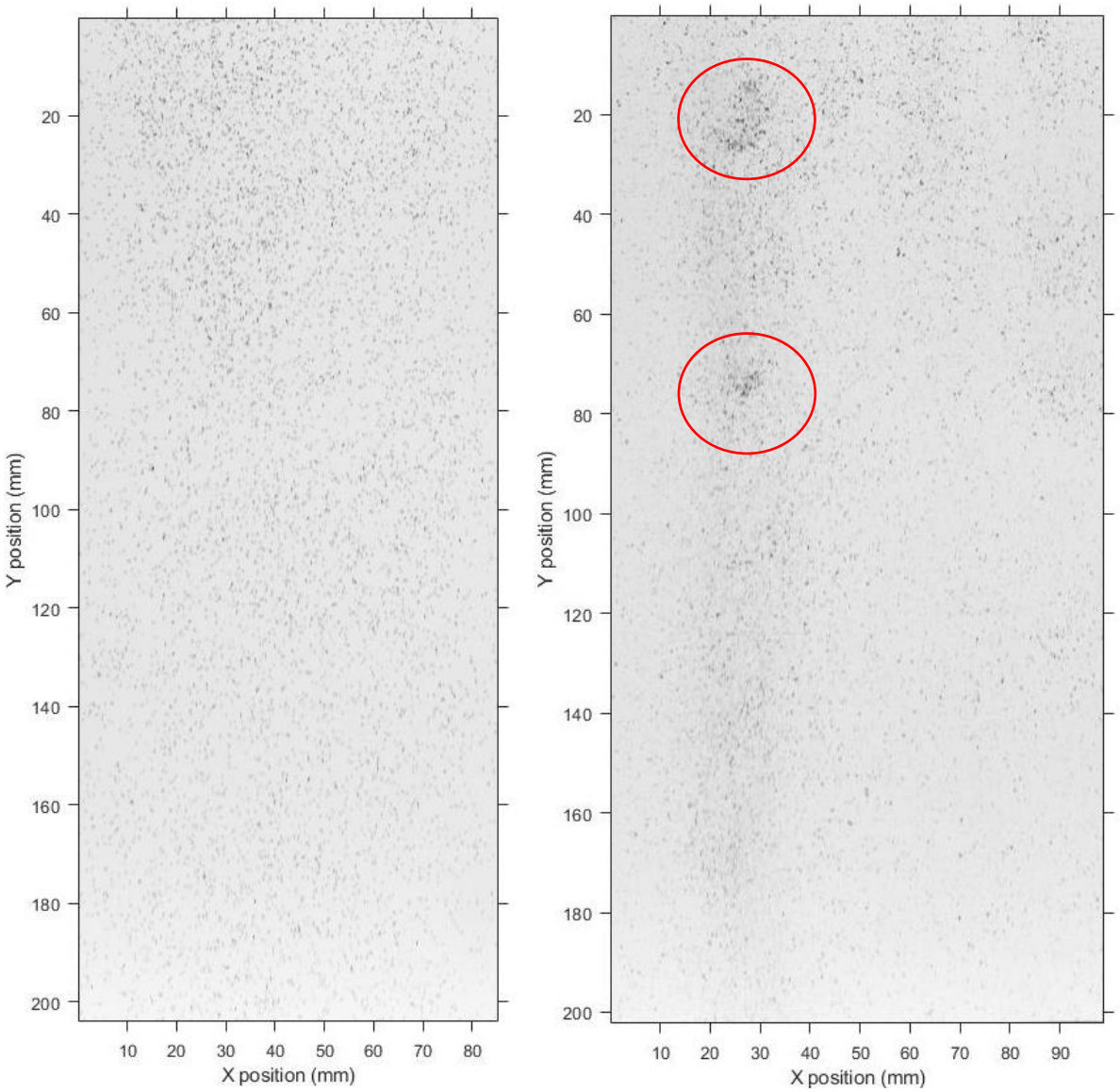

Figure 36. Left: Carbo particle curtain preheated to 450°C flowing at 6.4 g/s. Right: Sand particle curtain preheated to 450°C flowing at 3.2 g/s. As observed in the circled region, larger particle agglomerations can be observed in the sand particle curtain.

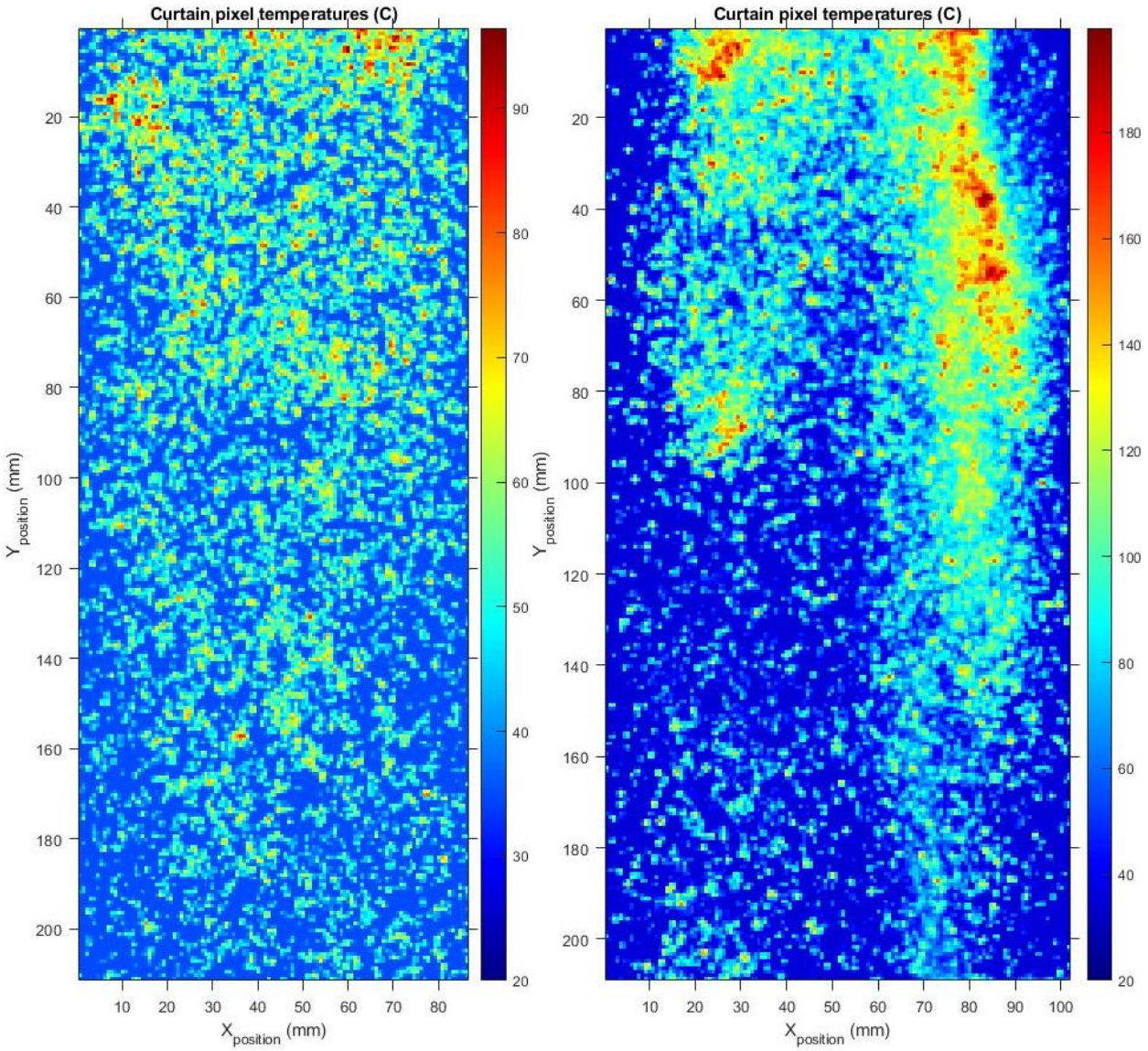

Figure 37. Left: Pixel temperature map of Carbo particle curtain preheated to 450°C flowing at 6.4 g/s. Right: Pixel temperature map of Sand particle curtain preheated to 450°C flowing at 3.2 g/s. Similarly, larger particle agglomerations can be observed in the sand particle curtain which would yield higher pixel temperatures; however, the opposite can be seen in the bottom half of the curtain as lower temperatures were measured.

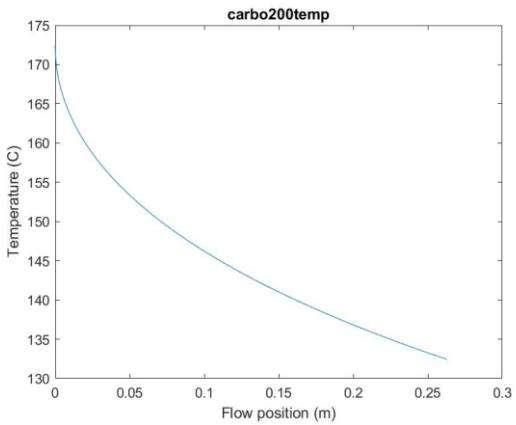

Empirical profile from thermocouples for Carbo particles preheated to 200°C

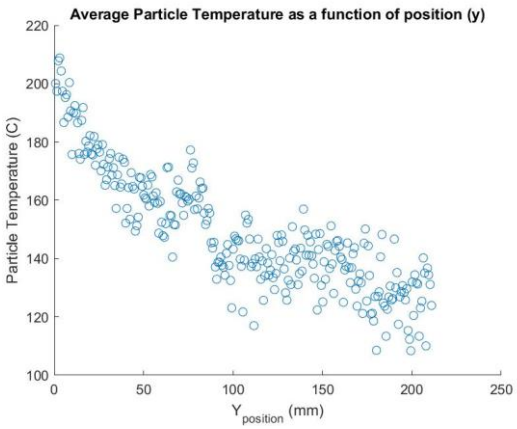

Extracted temperature profile for Carbo particles preheated to 200°C

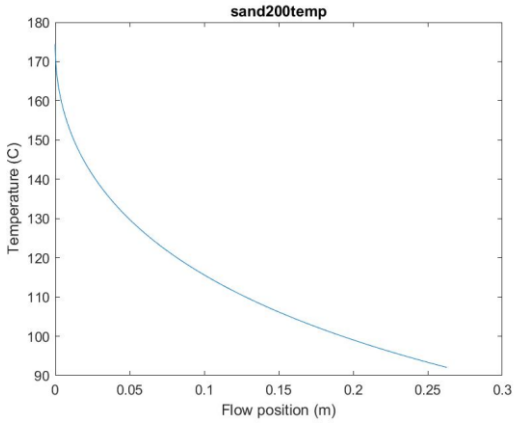

Empirical profile from thermocouples for Sand particles preheated to 200°C

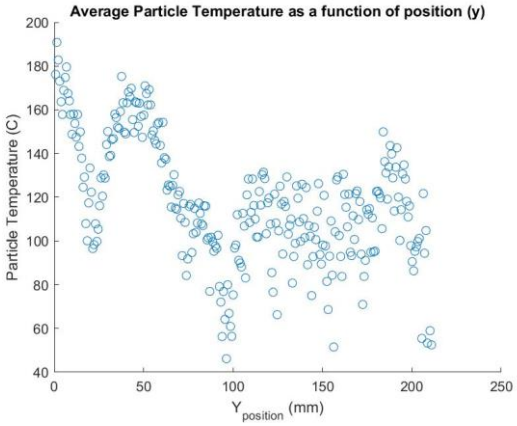

Extracted temperature profile for Sand particles preheated to 200°C

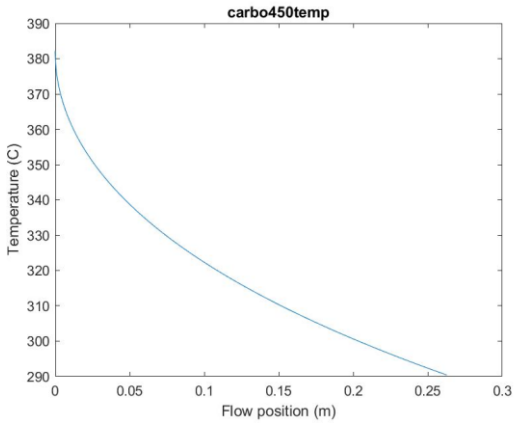

Empirical profile from thermocouples for Carbo particles preheated to 450°C

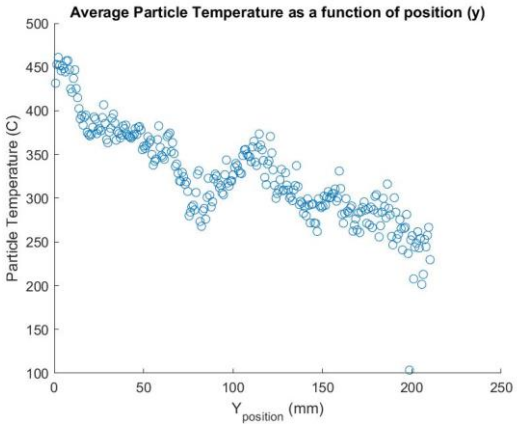

Extracted temperature profile for Carbo particles preheated to 450°C

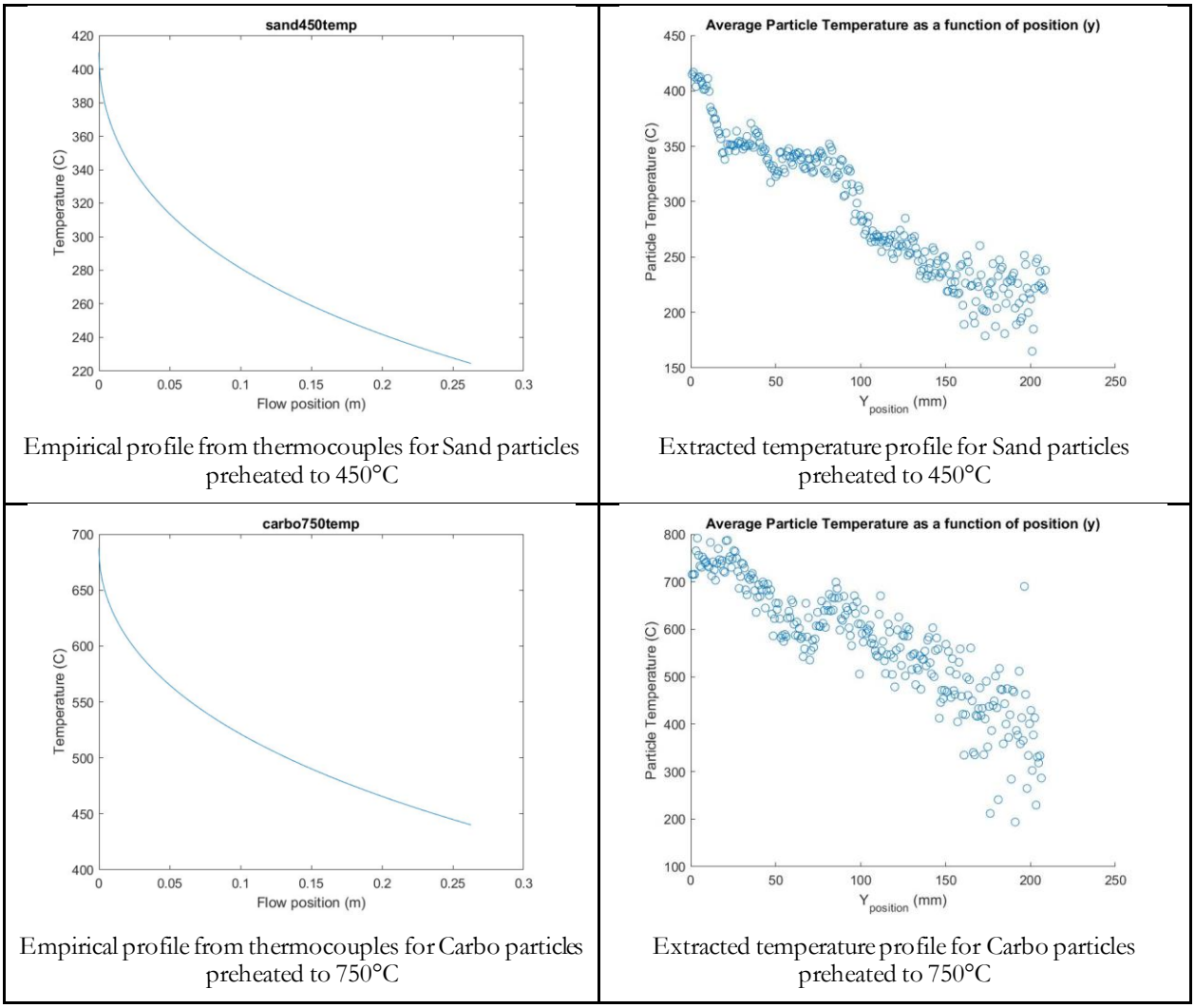

Empirical profile from thermocouples for Sand particles preheated to 450°C

Extracted temperature profile for Sand particles preheated to 450°C

Empirical profile from thermocouples for Carbo particles preheated to 750°C

Extracted temperature profile for Carbo particles preheated to 750°C

Figure 38. Comparison of particle temperature measured with the thermocouples and the particle temperature extracted applying the methodology developed.

Average Particle Velocity

Particle image velocimetry (PIV) is an imaging method that extracts complete velocity vector fields in one and two dimensions from a time-resolved image sequence. These vector fields are obtained by analyzing the region of interest (ROI) for a set of consecutive images in which the motion of a pixel cluster can be observed (Figure 39).

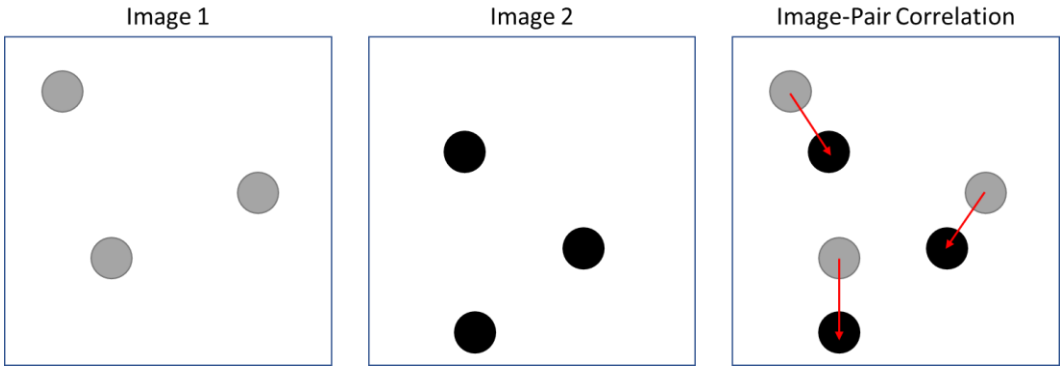

Figure 39: correlation of particles within a region of interest to extract vector fields. These vector fields are then converted to velocity based on the reference scale and time between the image pair.

PIVlab is a MATLAB toolbox with a graphical user interface from which most of the functions related to PIV can be accessed (note: PIVlab requires the MATLAB image processing toolbox to run). The PIVlab Graphic User Interface (GUI) makes these types of analyses easily accessible to everyone as it requires the three main steps to perform an analysis.

First, a region of interest (ROI) containing the curtain of falling particles was established to perform all the subsequent calculations as shown in Figure 40. The pre-processing setup was followed by a calibration process to provide a conversion factor from pixel distance to physical distance as well as the interval of time between each image. This calibration was achieved using the perforations on the structure shown on the right side of the image. These perforations are 50.8 mm (2") apart from each other. Lastly, the image evaluation on the PIV settings under the analysis tab of PIVlab. During this step, the FFT window deformation PIV algorithm was selected with multiple passes and interrogation windows with 50% steps. The interrogation windows used were square areas with side length of 32 and 16 pixels for passes 1 and 2, respectively.

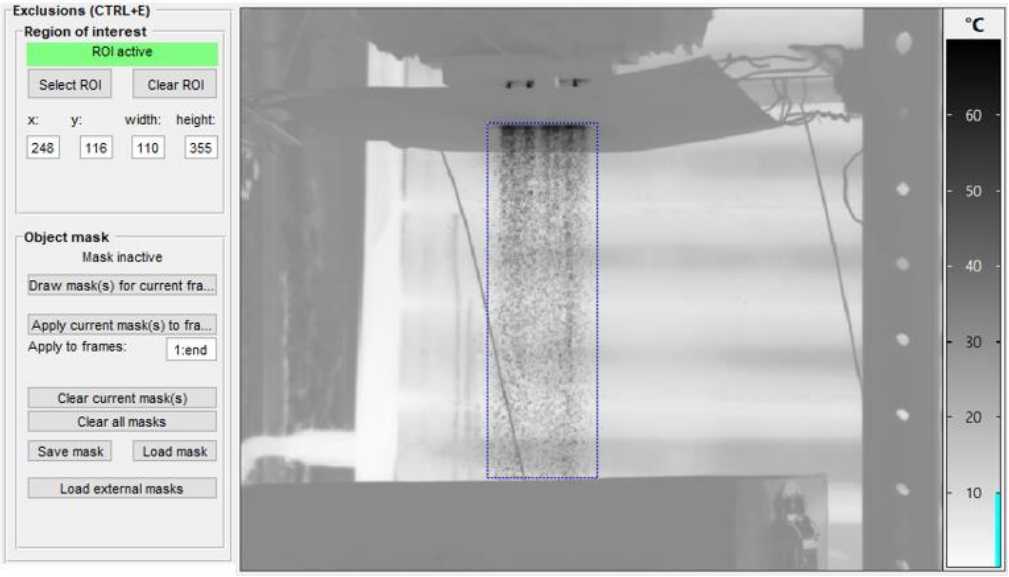

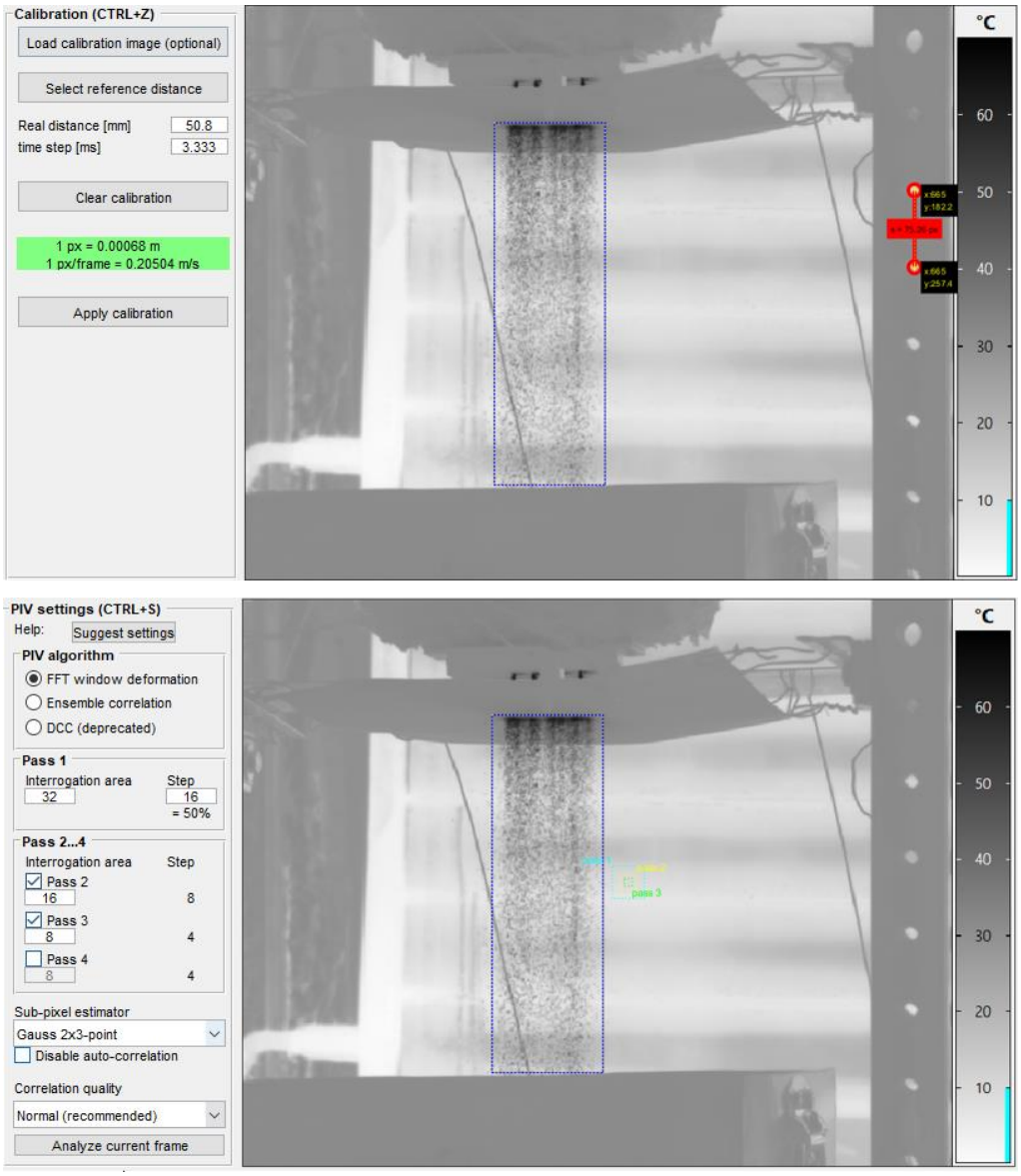

Figure 40: Top: establishing the image region of interest for the PIV analysis. Middle: Scaling and calibration of the image. Bottom: image evaluation setting for correlation interrogation window.

Applying the pre-established temporal and spatial scales, the average velocities the vectors can then be scaled, and the average velocity can then be extracted from the image pairs from a polyline selected in the image as seen in Figure 41. The velocity profiles of a low (100°C), medium (450°C), high (750°C) temperature curtains were extracted to compare the effects of the plume temperature on the curtain velocity. As seen before, although not very significant, drag forces begin to play a role on the discharge velocity as the curtain flows downstream. Comparing the discharge velocity profiles on Figure 42 as a function of particle temperature, it appears that the particle temperature does not have a noticeable effect on the discharge velocity profile. This could roughly mean that the bulk fluid (air) temperature remains at a similar value throughout the tests.

On the other hand, a similar trend that deviates from the free-fall profile can be observed as before. These means that drag forces become a factor as the curtain accelerates downwards permitting the

entrainment of air, which spreads the particles within it away from each other; hence, producing increasing the effects of drag.

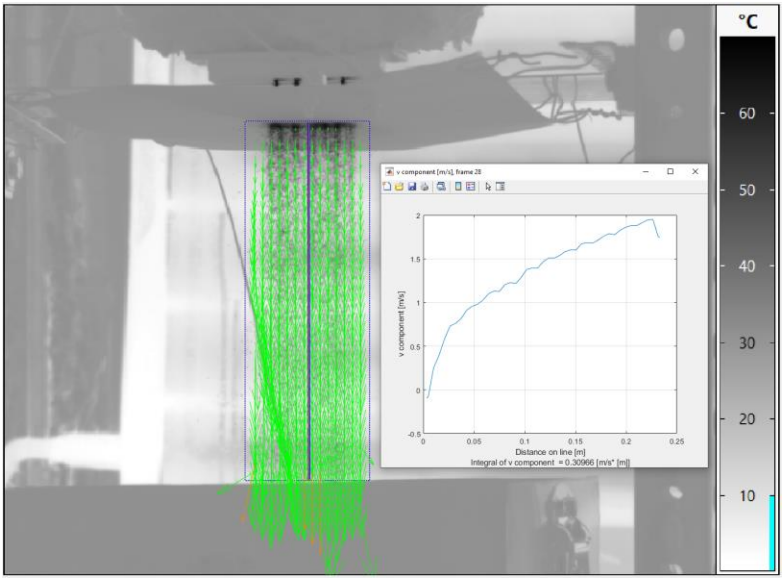

Figure 41: The velocity as a function of discharge position can be extracted from the vector fields using the pre-specified scaling values.

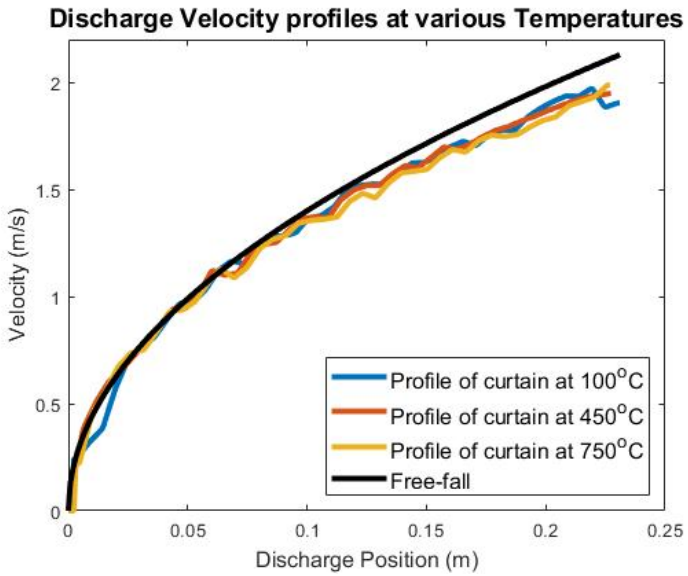

Figure 42: Discharge velocities estimated through PIV at the different temperatures.

Average Particle Mass Flow Rate

Referring back to the derivation of the mass flow rate equation (Eq. 3.22), to estimate the mass flow rate of the particles we need to complete two main measurements. First, the bulk particle velocity which is estimated through PIV tools. Moreover, the particles are used as tracers to estimate the physics of the entire plume; therefore, the velocity of the particles is assumed to be the same of the

entire plume. Last, the plume opacity estimation is required to complete this calculation. As we see on Eq. 3.21, opacity is related to the particle volume fraction, which in turn is related to the bulk density (Eq. 3.18).

Applying this equation to the case seen in Figure 43, after estimating the opacity applying the methodology described as well as the particle velocity, the mass flow rate can be calculated using Eq. 3.22 which yields the plot shown on Figure 44 where we can see a good agreement with the average mass flow rate measured using the scale during experiments. Similarly, we tested a curtain with a smaller flow rate to find that we are able to estimate the flow rate of particles as seen on Figure 45.

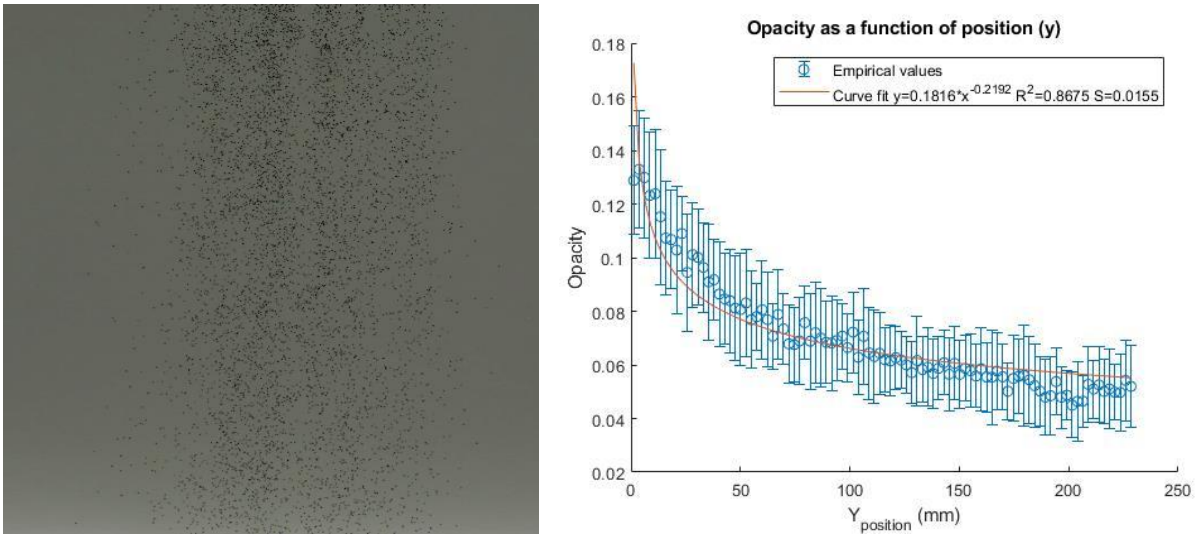

Figure 43. Left: Image taken with Nikon Camera for a 5.2 g/s curtain. Right: Opacity profile as a function of discharge position.

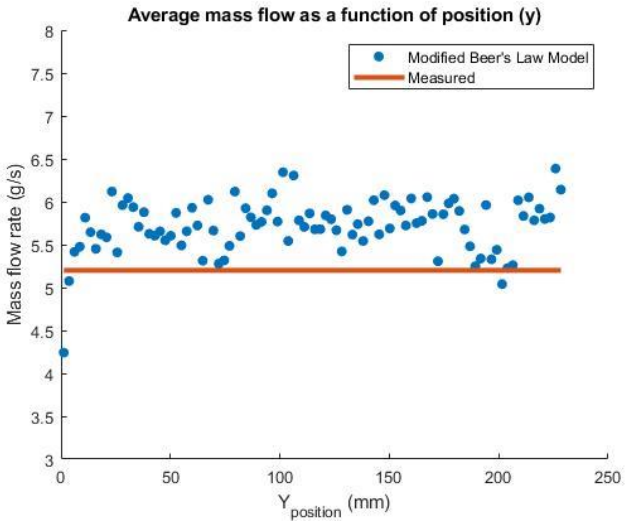

Figure 44. Comparison of Mass Flow Rate measured and Estimated using Equation 3.22.

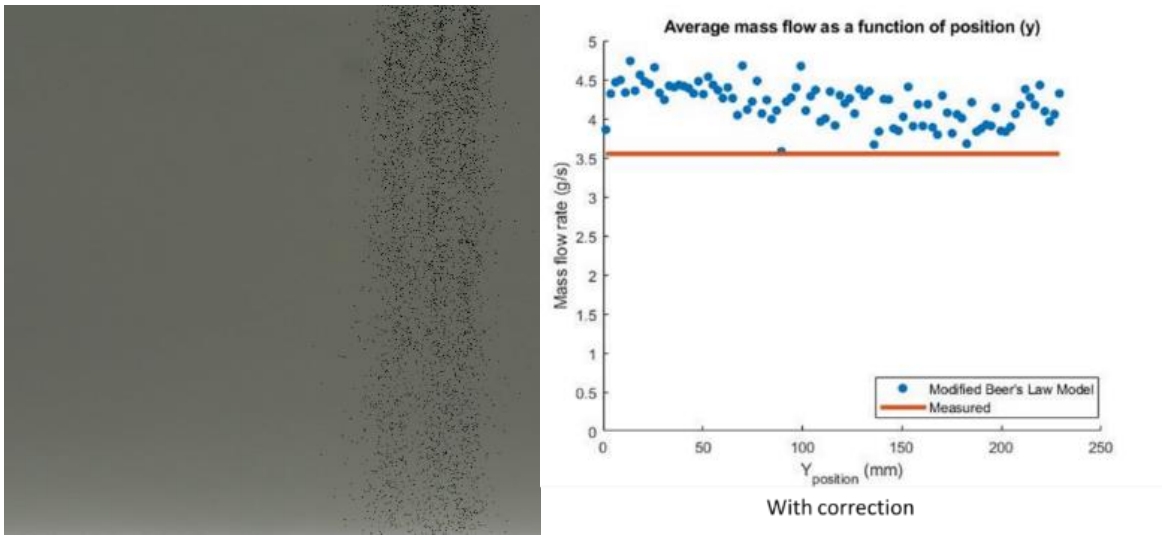

Figure 45. Left: Image taken with Nikon Camera for a 3.5 g/s curtain. Right: Comparison of Mass Flow Rate measured and Estimated using Equation 3.22.

Having completed these series of validations, new functions were introduced into our script to continue reshaping the methodology. These new updated functions, required for on-sun tests, will account for flow direction change and the opacity calculation as now the particles will be the illuminated regions on the image while the background is darker.

3.4. On-Sun Testing and Validation

Test Setup at Sandia

As the on-sun tests at Sandia began, the particle imaging team designed a camera test stand which is used to mount the cameras during the tests. The camera enclosure (Figure 46), which holds and protects the IR and Nikon cameras is mounted on the test stand which helps maintain a 5 meter distance from the aperture. The camera enclosure has an acrylic cover along with a quartz window and an IR window, for the Nikon and IR cameras, respectively. To mount/dismount the cameras, we have left the bottom side uncovered which will allow easy access while mounted on the camera test stand (Figure 47). The test stand module must be anchored to the elevator platform to ensure that there are no dangers during testing.

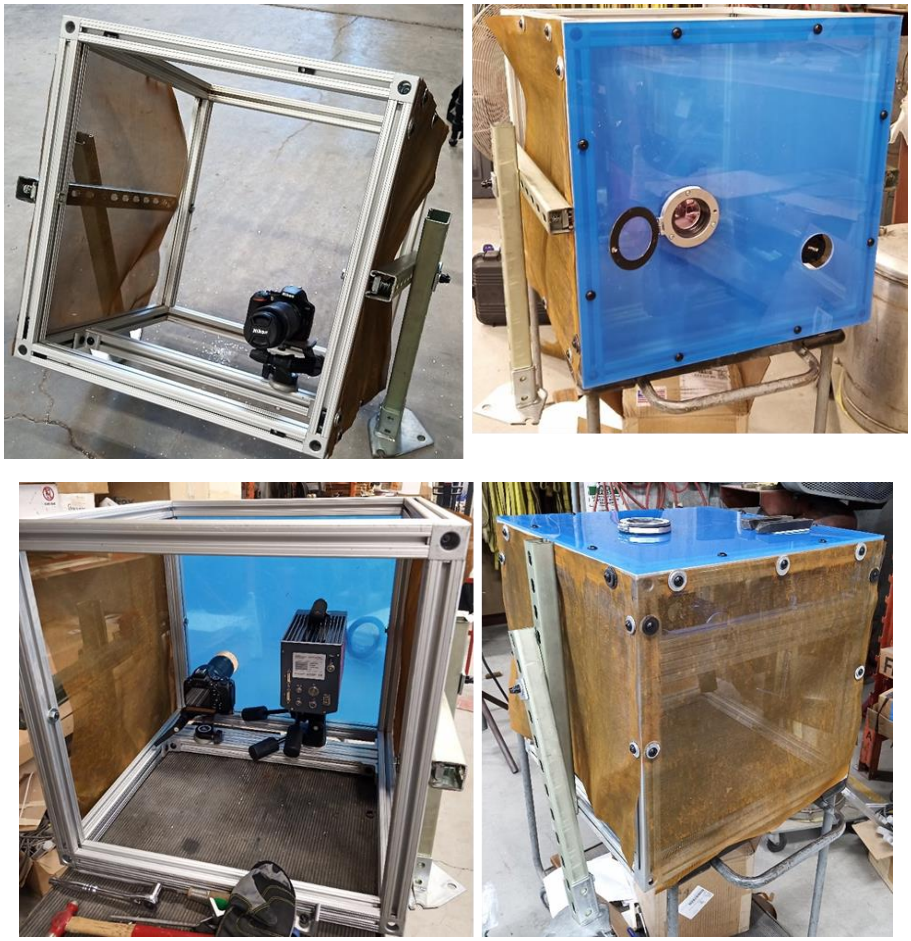

Figure 46. Camera enclosure built to protect and mount the cameras.

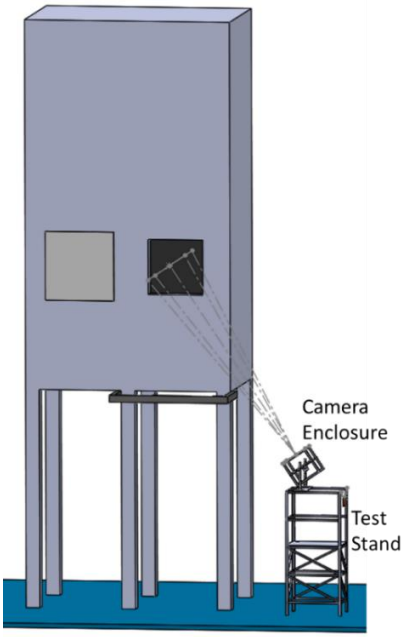

Figure 47. Diagram of cameras mounted with respect to the particle receiver.

On-Sun Test at Sandia

We began on-sun testing at Sandia while our camera setup collected images and thermograms. Prior to testing we completed an assessment to determine the best location for our DAQ system since we required a well-ventilated area to maintain the temperature of the computer and buffer within the operation range. Figure 48 shows a diagram schematic of the connectivity of the cameras to the DAQ system. Similarly, we performed a few tests to estimate the sampling frequency of the cameras in order to synchronize the images and thermograms. The IR camera collects 300 frames per second while the Nikon camera captures and transfers 1 image every 1.85 seconds in average. In order to ensure that we can capture enough data during on-sun tests we determine that the best method to capture images would be if we captured for 2 minutes continuously and then wait 2 minutes. By doing this, we allow the cameras enough time to render and transfer all images. This yields approximately 36,000 thermograms and 65 images, resulting in approximately 12 GB of data per measurement.

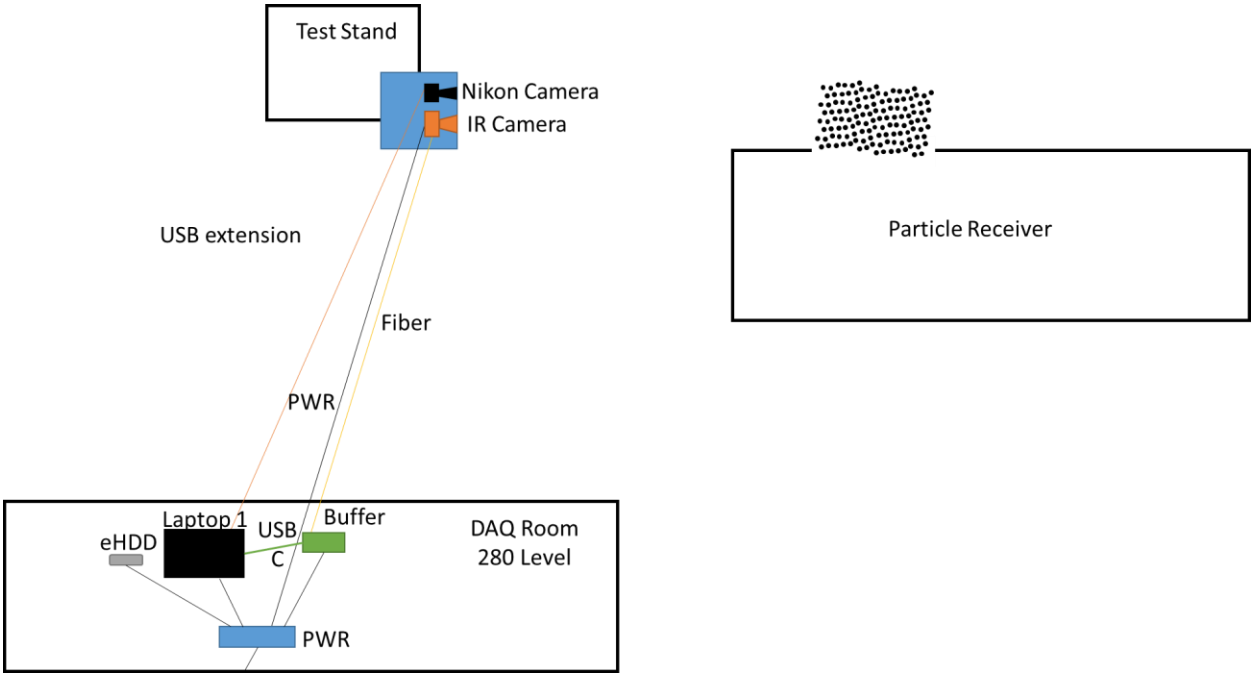

Figure 48. Wiring diagrams and positioning of the cameras with respect to the particle receiver on top of the tower. The DAQ room is located at the 280 level (20 ft below the roof of the tower)

We also completed an assessment of the Nikon camera settings. One big question that we had prior to the on-sun tests was related to the concentrated light and its impact of our measurements. Based upon our preliminary tests, we found no major issues with concentrated light. The exposure settings for the on-sun tests had to be modified slightly from our previous values and the new values are summarized in Table 3.

Table 3. New exposure settings for Nikon camera used for the on-sun tests

Setting	Value
ISO	200
F-distance	8.0
Shutter Speed	1/4000 s

We are currently post-processing the first sets of images obtained. The particles during on-sun heating are easily resolvable, and we can also observe them through the IR camera as seen in Figure 49 and Figure 50. While the system is undergoing the final round of adjustments, we need to identify the cause of the halo that out IR camera sees during on-sun operation. We believe it could be due to the refraction across the IR window from the scattered concentrated light, but we will continue to investigate that. Similarly, we must decide how we should account for the dust residue that can be seen in Figure 49, and put a quantitative limit on how much it could impact our opacity and particle temperature calculations.

At present, we have collected data from eight tests days. Four of these days include the preheating of the sCO2 loop at Sandia. They include particle temperatures ranging from 100 to 700 °C. So far, we have learned a few important things to consider before and during every test. This includes:

1. Enclosure windows need to be cleaned prior to every test to ensure no particle residue is blocking the view
2. Focusing the Nikon camera every time we disconnect it from LiveView
3. Initializing the IR camera (NUC) to ensure consistent temperature readings
4. During tests, we should transfer data to a secondary computer to begin exporting image sequences for PIV and matrix files for the temperature post-processing.

Figure 49. Visible-light image (DSC_0959) obtained during tests at 500 suns. Inlet particle temperature ~430 C and outlet particle temperature ~441 C. Data collected: 12:06 September 4th 2020.

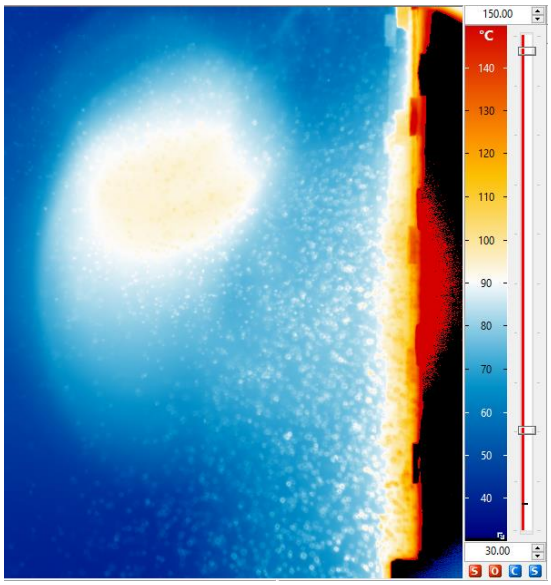

Figure 50. Thermogram (200904_120602/ir_data_0001) collected during tests at 500 suns. Inlet particle temperature ~430 C and outlet particle temperature ~441 C. Data collected: 12:06 September 4th 2020.

Filtering Images and Thermograms

The initial tests at Sandia showed a new impediment to our measurements in the form of fine dust in the background. While particles of the same order of magnitude as the mean diameter egressed from the cavity, particulates of a much smaller size also did, manifesting as a diffuse halo near the aperture which needed to be removed for our calculations. Similarly, to simplify the calculations, the image is adjusted so that the particle egress flow is to the positive side of the X-axis - to make calculations consistent for comparison.

Figure 51. For the analysis, the image is adjusted so the flow of particles is to the positive side of the X-axis. The blue line denotes the top, the green line is the bottom, the orange line is the East side and the yellow line the West side of the FPR aperture.

To remove the dust in the background and leave the particles only, a median filter was applied to the visible images to remove the outlier pixels (i.e. particles), leaving only the dusty background. To assess how effectively particles are removed from the RAW image, the structural similarity index measure (SSIM) can be used to measure the perceptual differences between the RAW and the filtered images.. Using the appropriate built-in function in MATLAB, the SSIM can be computed between the filtered image without particles and the RAW image. The resulting filtered images show in Figure 52 that a matrix size of approximately 90x90 converges to a value of 0.9006 which means that the images are approximately 90% similar since the outliers (pixels with particles) were filtered out. From the samples shown in Figure 53, the 90x90 case shows no visible signs of outliers.

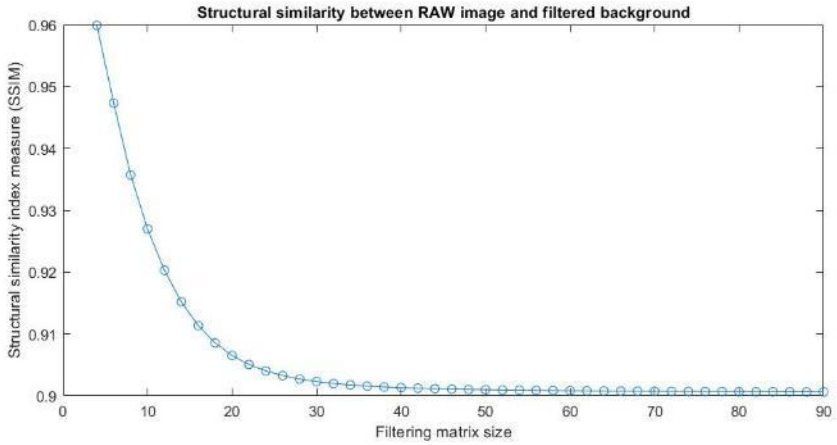

Figure 52. The difference of SSIM between the filtered background and RAW images.

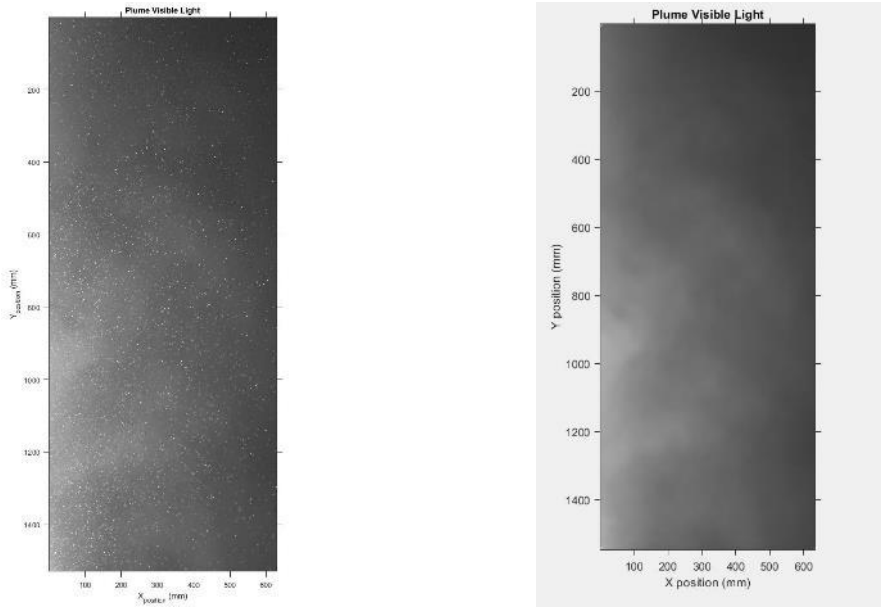

RAW Image M = 90x90 filtered

Figure 53. Resulting filtered image (right) without particles from the original RAW image (left).

Once the required filter to remove the particles (outliers) is produced, the algorithm will find the pixels that contain pixels which have an intensity higher than the background with dust, and this will yield an image with particles only. Nonetheless, some of these pixels could still be part of the background if the value is slightly above the reference values. The results show that a tolerance of

5% yields an image with particles only that closely resembles the position and the number of particles on the RAW image as seen in Figure 54.

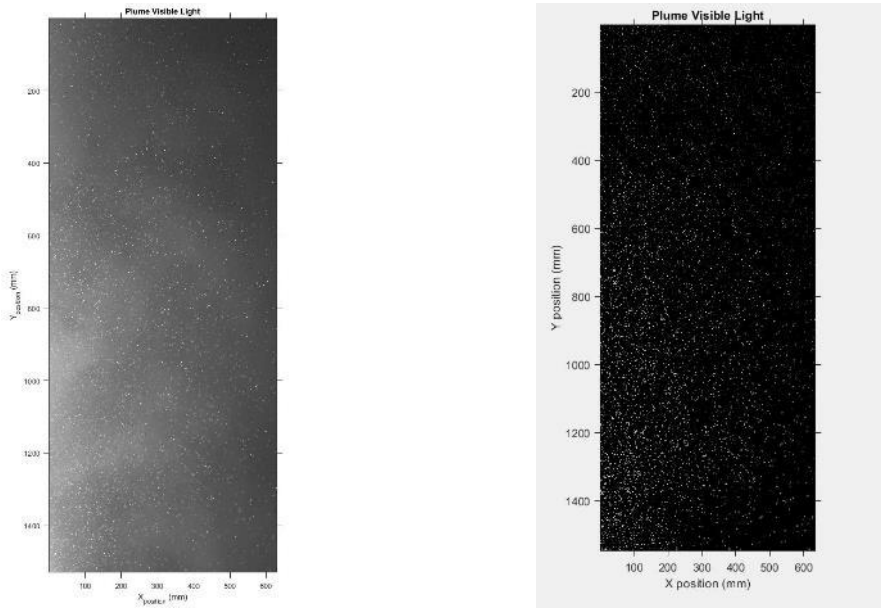

RAW Image M = 90x90 & Tol = 5.0% filtered

Figure 54. Resulting filtered image (right) with particles only from the original RAW image (left).

Similarly, the thermograms require filtering to remove the dust which can influence the average temperature on the thermogram as seen in Figure 55. This is because the pixels considered for the analysis are those with temperature values above background temperature. The resulting filtered images show that a matrix size of approximately 25x25 will sufficiently eliminate all the temperature outliers and will yield an image that does not contain particles as shown in Figure 55.

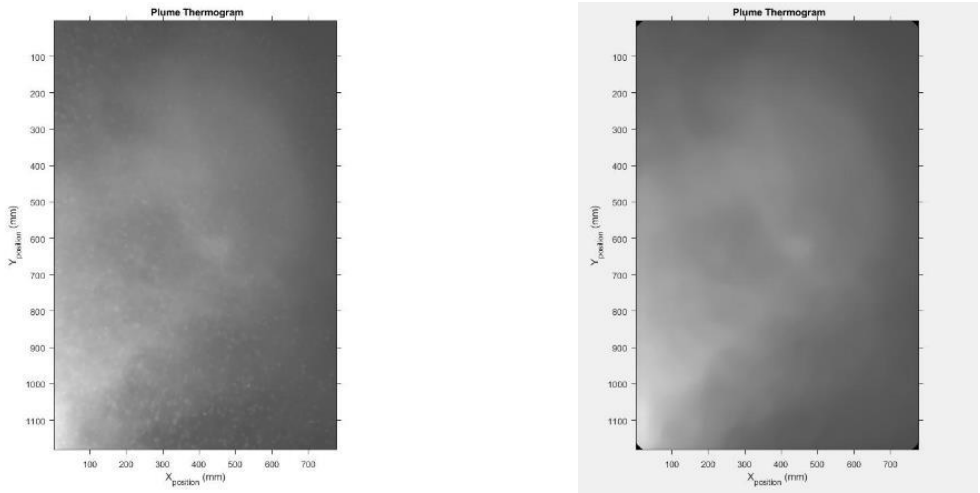

RAW Thermogram M = 25x25 filtered

Figure 55. Resulting filtered thermogram (right) without particles from the original RAW thermogram (left).

When we consider the image with particles only, some of the pixels could still be part of the background if the value is only slightly above the reference values; therefore, a tolerance is applied. As it was observed, a tolerance of 1.5% yields an image with particles only that closely resembles the position and the number of particles in the RAW image as shown in Figure 56.

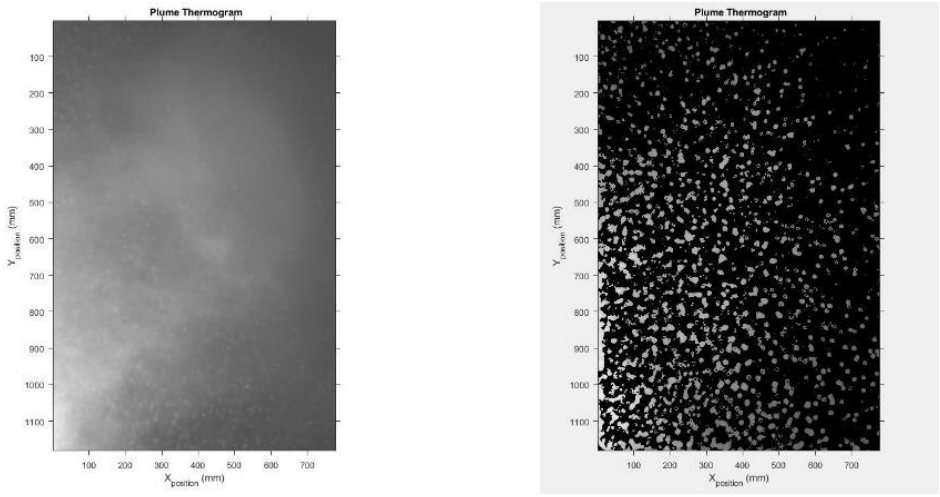

RAW Thermogram M = 25x25 & Tol = 1.5% Filtered

Figure 56. Original RAW thermogram (left) and result of filtering leaving particles only (right).

Particle Image Velocimetry (PIV) Measurements

In addition to calculating the particle temperature, the filtered thermogram sequence can be used to get an estimate of the velocity field of the plume through PIV. Using PIVlab's command interface, we were able to integrate the velocity estimation within our code to determine the average x-velocity field (Figure 33).

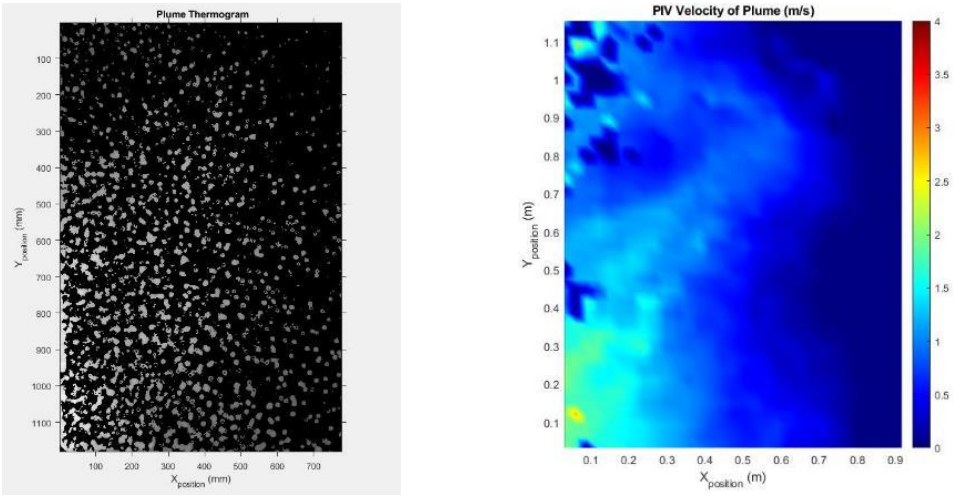

Filtered Thermogram Average X-Velocity of Plume

Figure 57. Using the PIVlab setup used in the past for a 10 thermogram sequence we can obtain a velocity field map which then can be used to estimate the average X-velocity.

On-sun Tests and Results

The team collected data for multiple configurations of the FPR. Some changes were introduced into the code to adapt it to post-process the on-sun tests. In this report, we will be presenting results for three different test cases from September 4th, 2020, November 3rd, 2020, and March 3rd, 2021. As mentioned before, 65 images and 36,000 thermograms (at 300 fps) correspond to a 2-minute data set.

To complete the calculations, the heat loss of the particles within the plume can be estimated using Eq. 3.24 to Eq. 3.26. Here, the particle egress rate ($\dot{m}_p$) was obtained from Eq. 3.24, while the heat capacity function ($Cp_p(T)$) is obtained from Ho et al. [10]. Similarly, the heat loss from the air within the plume can be estimated using Eq. 3.25. Following the calculations performed by Ho et al. [6], the air egress rate ($\dot{m}_a$) is related to the air density ($\rho_a(T_p)$), under the assumption that the flow area (A) and velocity (V) of the particles are approximately the same for the air within the plume. Moreover, Mills and Ho [11] have shown that approximately 70% of the simulated thermal losses from the FPR were due to advective/convective losses from the cavity. The total advective losses can be quantified using Eq. 3.26. It should be noted that these heat losses account for the heat lost by the particle and air egress from the cavity and do not account for the heat that could be carried away by the dust.

$$\dot{m}_a = \rho_a(T_p) A V \tag{3.24}$$

$$\dot{Q}_a = \dot{m}_a \int_{T_{amb}}^{T_p} Cp_a(T)\,dT \tag{3.25}$$

$$\dot{Q}_T = \dot{m}_p \int_{T_{amb}}^{T_p} Cp_p(T)\,dT + \dot{m}_a \int_{T_{amb}}^{T_p} Cp_a(T)\,dT \tag{3.26}$$

The results that will be presented below are for 3 discrete cases during our on-sunt testing campaign in 2020 and 2021. Table 4 provides a summary of the three cases selected for comparison. We tried to choose cases with different temperature ranges and different wind conditions, and we will continue to study the effect of these variables on particle egress.

Table 4. Table summarizing the three tests for which data is presented.

Test Date & Time	Input Power (kW)	Measured Particle Temperatures (°C)	Measured Efficiency (%)	Test Wind Conditions
9-4-20 10:59	420	Inlet:362 °C Outlet:408 °C	79-83 %	Wind due South (180°) 1.4 m/s
9-4-20 12:46	494	Inlet:528 °C Outlet:574 °C	67-69 %	Wind due Southwest (202°) 3.9 m/s
3-7-21 13:08	956	Inlet:679 °C Outlet:754 °C	55-59 %	Wind due Southwest (252°) 3.2 m/s

The following results below are for a discrete case on 9-4-20 captured at 10:59 am. It should be noted that the average values are calculated within the first 100 mm outside of the aperture. As seen on Figure 118, the average particle temperature exiting the cavity is estimated to be ~403 C while the receiver inlet and outlet temperatures were 362°C and 408°C, respectively. Similarly, as seen in Figure 121, the average total heat loss for the 2-minute period is approximately 50 kW. Under the

assumption of these losses representing 70% of the total receiver losses, this means that the total losses are ~71 kW.

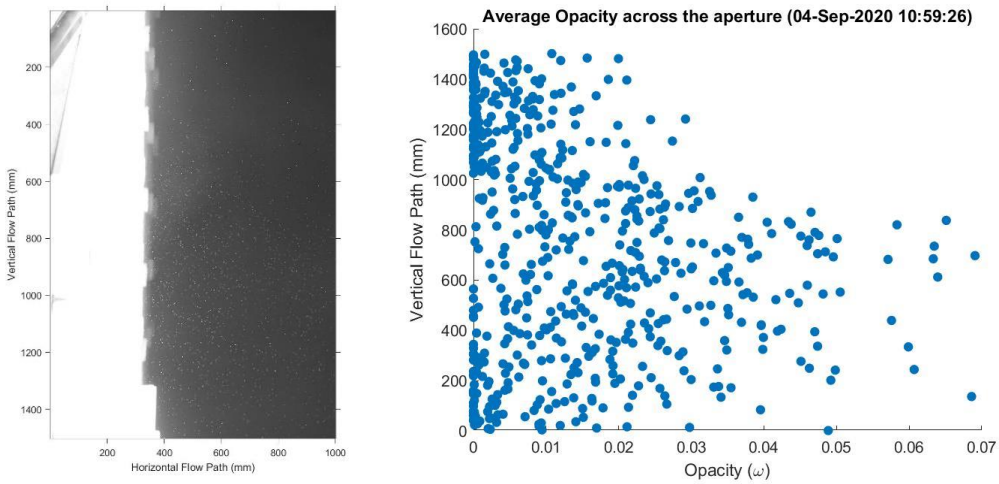

Figure 58. Opacity estimated from visible-light image. The calculations show the values of the opacity at discrete positions along the vertical flow path of the image. Average plume opacity of 1.43%.

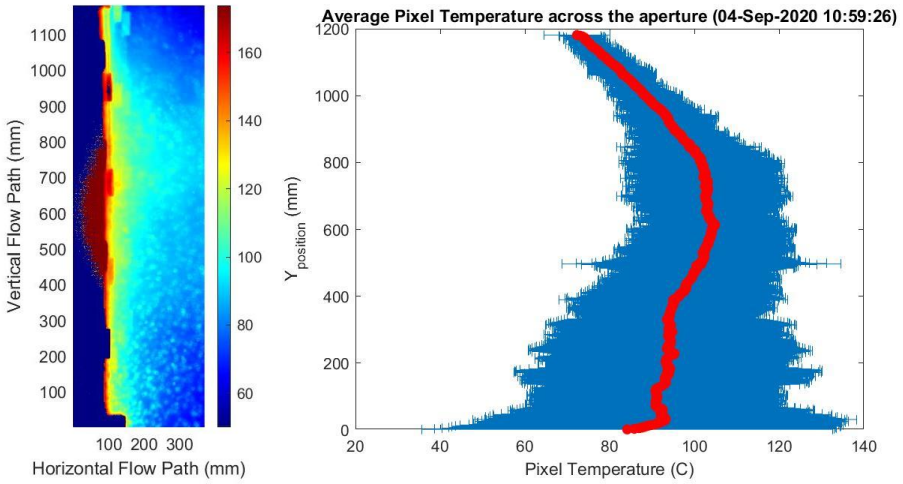

Figure 59. Pixel temperature estimated from thermogram sets. The calculations show the values of the pixel temperature at discrete positions along the vertical flow path of the thermogram. The error bars represent one standard deviation from the mean value. The mean squared error is calculated spatially (within the 100 mm region) and temporally (on the same region at different times during the experiment). Average pixel temperature of 94.7°C.

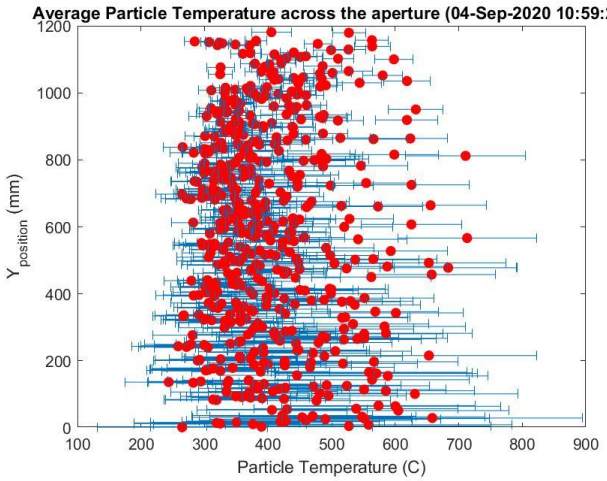

Figure 60. Particle temperature estimated using the methodology developed. The average particle temperature of 402.7°C. The error bars represent one standard deviation from the mean value calculated based on the radiation balance equation.

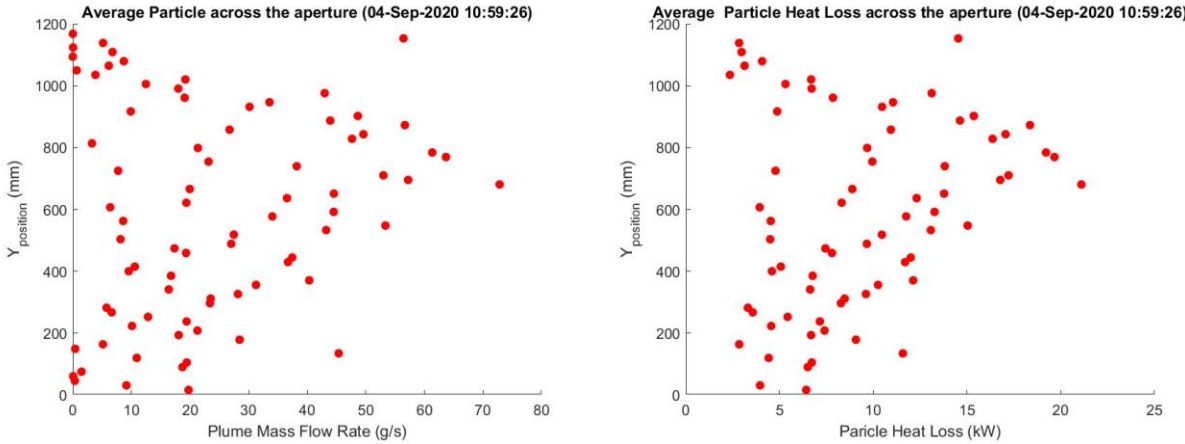

Figure 61. Left: Average instantaneous mass egress rate. The average mass egress rate is 23.9 g/s. Right: Average instantaneous particle heat loss. The average particle heat loss is 9.3 kW for this specific case.

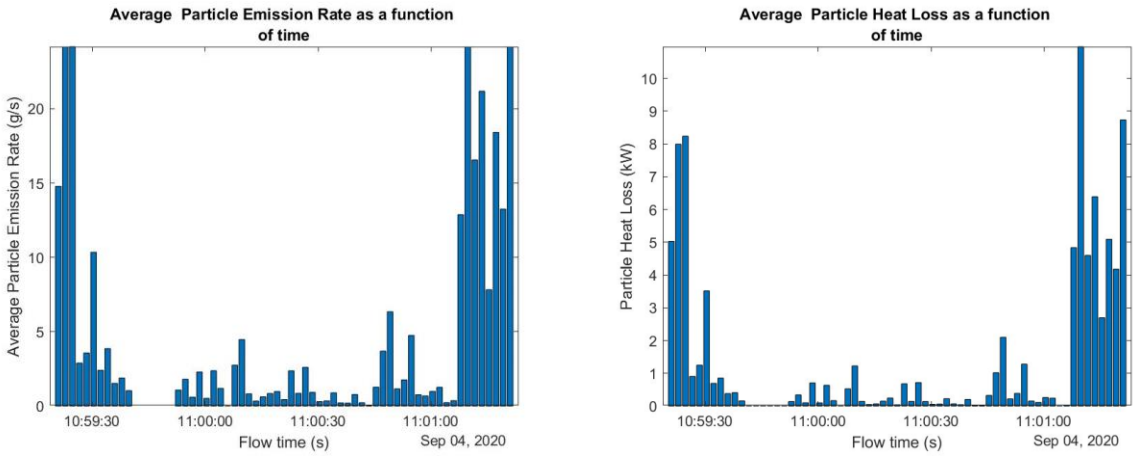

Figure 62. Left: Average instantaneous mass flow for the entire 2 minutes of data collection. Total mass loss is 0.63 kg. Right: Average instantaneous particle heat loss for the entire 2 minutes of data collection. Average heat loss 1.4 kW.

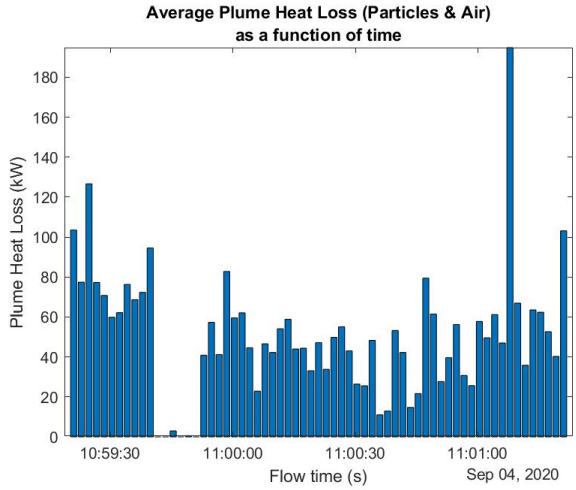

Figure 63. Average instantaneous total advective losses for the entire 2 minutes of data collection. The total average heat losses are 49.7 kW.

The following results below are for a discrete case on 9-4-20 captured at 12:46 pm. It should be noted that the average values are calculated within the first 100 mm outside of the aperture. As seen in Figure 65, the average particle temperature exiting the cavity is estimated to be ~546 C while the receiver inlet and outlet temperatures were 528°C and 574°C, respectively.

Similarly, as Figure 66 shows, the average total heat loss for the 2-minute period is approximately 70 kW. Under the assumption of these losses representing 70% of the total receiver losses, this means that the total losses are ~100 kW. For an estimated input power of 494kW, it yields an estimated efficiency of 79.7% while the measured receiver efficiency ranges from 67-69%.

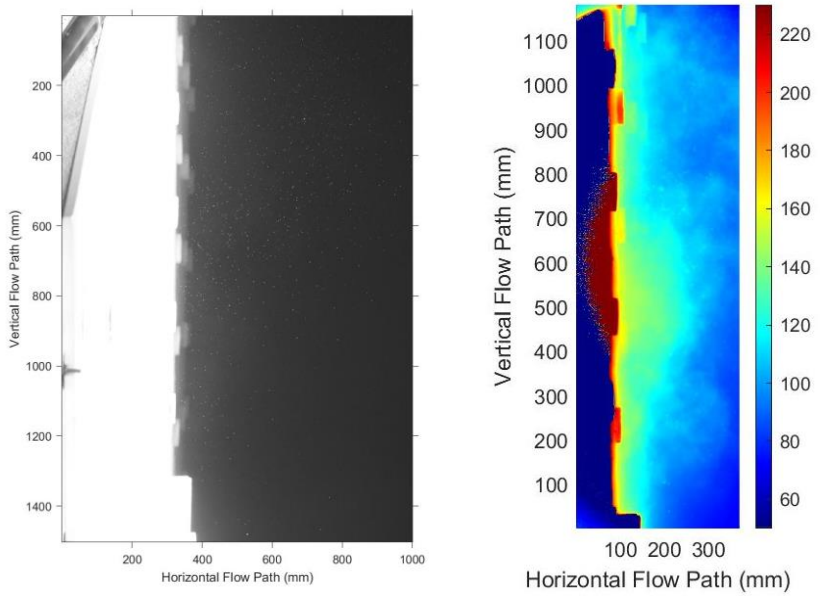

Figure 64. Left: Visible-light image sample from the set. Right: Thermogram sample from the set. We can see from the samples that for this case, the particle egress is low.

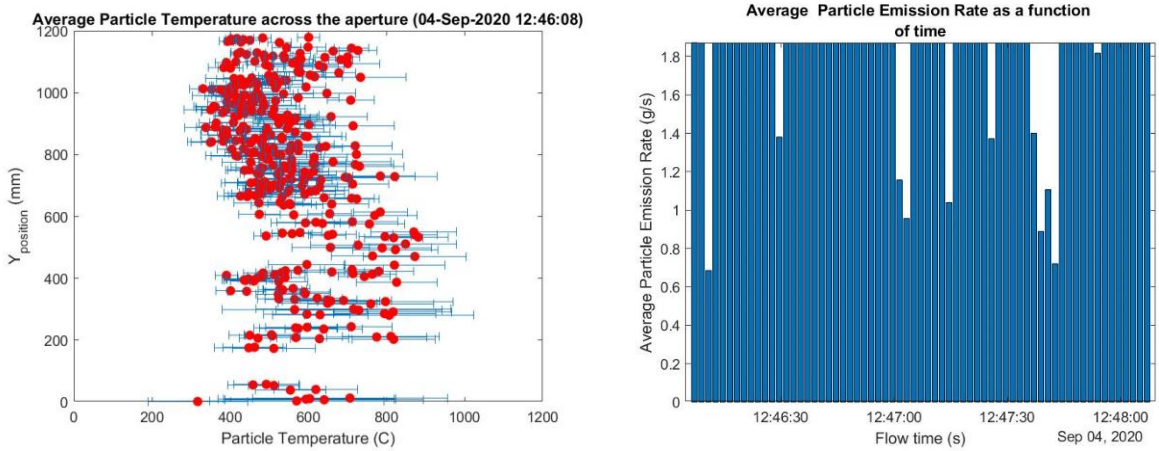

Figure 65. Left: Particle temperature estimated using the methodology developed. The average particle temperature of 546.1°C. The error bars represent one standard deviation from the mean value calculated based on the radiation balance equation. Right: Average instantaneous mass flow for the entire 2 minutes of data collection. Total mass loss is 0.47 kg.

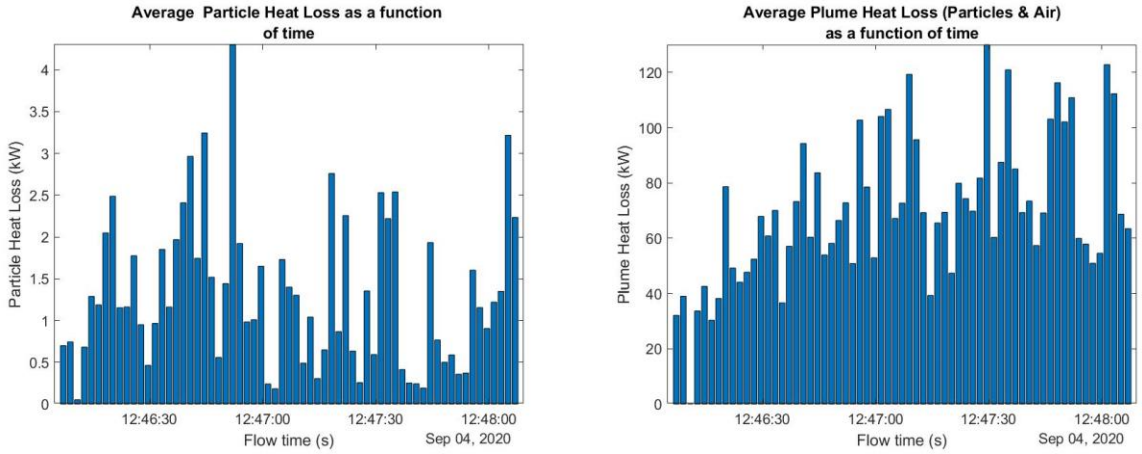

Figure 66. Left: Average instantaneous particle heat loss for the entire 2 minutes of data collection. Average heat loss 1.3 kW. Right: Average instantaneous total advective losses for the entire 2 minutes of data collection. The total average heat losses are 70.2 kW.

The following results below are for a discrete case on 3/7/21 captured at 13:08. Again, the average values are calculated within the first 100 mm outside of the aperture. Figure 68 shows that the average particle temperature exiting the cavity is ~493 °C while the receiver inlet and outlet temperatures were 679°C and 754°C, respectively.

Similarly, in Figure 69, the average total heat loss for the 2-minute period is approximately 75 kW. Under the assumption of these losses representing 70% of the total receiver losses, this means that the total losses are ~107 kW. For an estimated input power of 956kW, it yields an estimated efficiency of 88.8% while the measured receiver efficiency ranges from 55-59%. We think this discrepancy can be due to the high temperature of the particles leaving the cavity. These particles could be cooling faster than in other cases, as radiative losses become dominant over 500 °C.

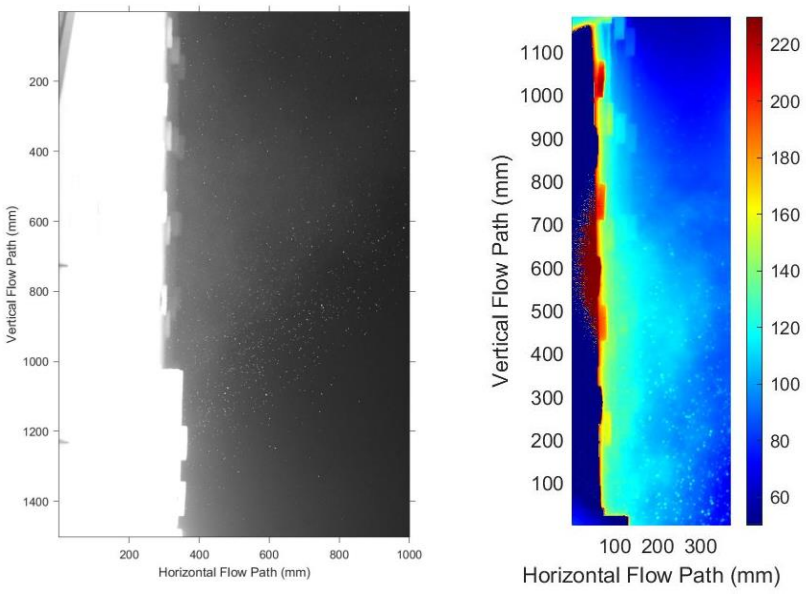

Figure 67. Left: Visible-light image sample from the set. Right: Thermogram sample from the set. We can see from the samples that for this case, the particle egress is low.

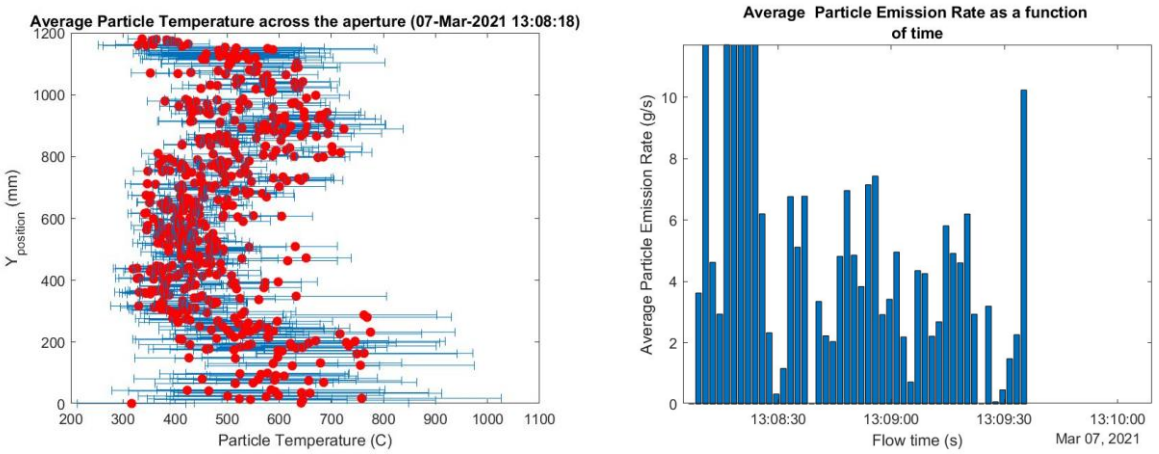

Figure 68. Left: Particle temperature estimated using the methodology developed. The average particle temperature of 492.6°C. The error bars represent one standard deviation from the mean value calculated based on the radiation balance equation. Right: Average instantaneous mass flow for the entire 2 minutes of data collection. Total mass loss is 0.67 kg.

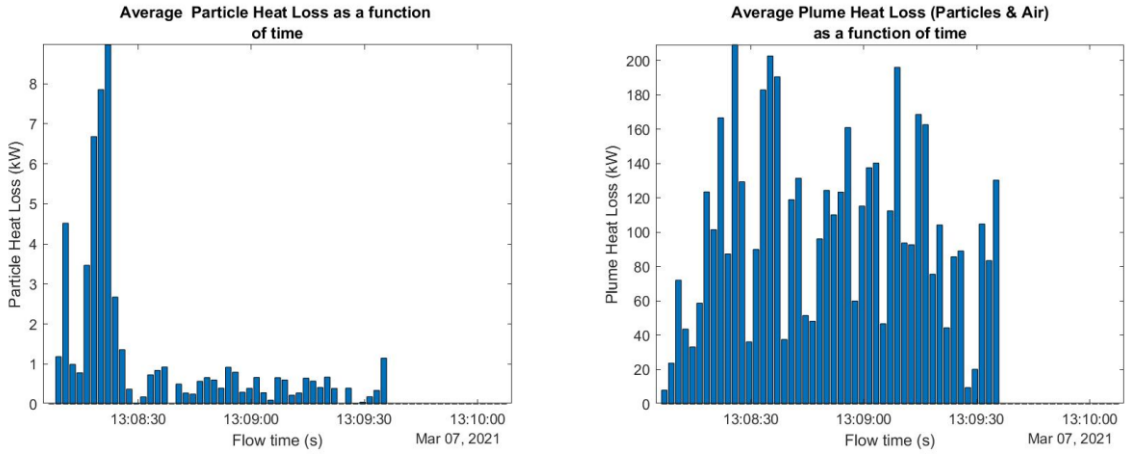

Figure 69. Left: Average instantaneous particle heat loss for the entire 2 minutes of data collection. Average heat loss 0.8 kW. Right: Average instantaneous total advective losses for the entire 2 minutes of data collection. The total average heat losses are 74.4 kW.

To further understand which factors contribute to the particle egress from the cavity, the team built a design of experiments (DoE) matrix to compare 6 variables of interest which we believe could have an adverse effect on the FPR performance.

1. Average particle temperature (A)
2. Receiver mass flow rate (B)
3. Receiver flow configuration (C)
4. Heat flux level (D)
5. Wind speed (E)
6. Wind direction (F)

To populate the DoE matrix, we constraint the six factors to only two levels, as possible, with the following thresholds:

1. Average particle temperature: High (≥500°C) and Low (<500°C)
2. Receiver mass flow rate: High (≥6 kg/s) and Low (<6 kg/s)
3. Receiver flow configuration: 1 (2 stairs), 2 (1 stair) and 3 (0 stairs)
4. Heat flux level: High (≥80 W/cm^2) and Low (<80 W/cm^2)
5. Wind speed: High (≥4.5 m/s) and Low (<4.5 m/s)
6. Wind direction: Front (≤90° & ≥270°) and Back (>90° & <270°)

All the factors are 2-levels except the flow configuration which is 3-levels. In a standard full-factorial DoE, the number of required cases becomes p^k where p is the number of levels and k is the number of factors. If our matrix had 2-level factors only it would require 64 combinations to run a full-factorial DoE matrix. For this case, we will require 96 combinations for the full-factorial DoE matrix. Nonetheless, based on the data collected during the testing campaign, we were only able to capture data for 42 of these distinct cases.

Initially, the team performed a regression analysis for the 6 factors only without including possible interactions amongst them. Based on the p-values calculated, the results showed that the only significant factor was the average particle temperature as shown on Table 5. Similarly, the R^2 value of 0.203 appeared low which led us to think that perhaps a better approach should include compounded interaction between the factors.

Table 5. Results from regression analysis for the 6 factors selected. R^2 = 0.203

	Coefficients	Standard Error	t Stat	P-value	Lower 95%	Upper 95%
Intercept	7.8229	2.5337	3.0876	0.0039	2.6793	12.9666
Particle Temperature	5.0472	1.9401	2.6015	0.0135	1.1086	8.9858
Mass Flow Rate	-0.2205	1.9762	-0.1116	0.9118	-4.2325	3.7915
Flow Configuration	-2.3886	3.9321	-0.6074	0.5475	-10.3711	5.5940
Heat Flux Level	-1.8875	3.3981	-0.5555	0.5821	-8.7859	5.0110
Wind Speed	1.5719	1.9321	0.8136	0.4214	-2.3504	5.4942
Wind Direction	1.0022	1.9762	0.5071	0.6153	-3.0098	5.0142

When we considered the 15 compounded factors, the team found that while the R^2 value improves, there are 3 compounded factors with a low P-value, as shown in Table 6; pointing to multiple and compounded factors which have a direct impact on particle egress.

1. Average particle temperature X Receiver mass flow rate (A x B)
2. Average particle temperature X Receiver flow configuration (A x C)
3. Average particle temperature X Heat flux level (A x D)
4. Average particle temperature X Wind speed (A x E)

5. Average particle temperature X Wind direction (A x F)
6. Receiver mass flow rate X Receiver flow configuration (B x C)
7. Receiver mass flow rate X Heat flux level (B x D)
8. Receiver mass flow rate X Wind speed (B x E)
9. Receiver mass flow rate X Wind direction (B x F)
10. Receiver flow configuration X Heat flux level (C x D)
11. Receiver flow configuration X Wind speed (C x E)
12. Receiver flow configuration X Wind direction (C x F)
13. Heat flux level X Wind speed (D x E)
14. Heat flux level X Wind direction (D x F)
15. Wind speed X Wind direction (E x F)

Table 6. Results from regression analysis for the 15 compounded factors selected. $R^2 = 0.369$

	Coefficients	Standard Error	t Stat	P-value	Lower 95%	Upper 95%
Intercept	9.6435	2.9485	3.2706	0.0030	3.5828	15.7043
AB	1.7489	2.0526	0.8521	0.4020	-2.4702	5.9681
AC	-2.8840	3.8011	-0.7587	0.4548	-10.6972	4.9293
AD	-6.0645	2.9485	-2.0568	0.0499	-12.1253	-0.0038
AE	2.7112	2.0348	1.3324	0.1943	-1.4715	6.8938
AF	0.2401	2.0931	0.1147	0.9095	-4.0622	4.5425
BC	-0.8254	4.0113	-0.2058	0.8386	-9.0708	7.4199
BD	-0.3520	2.9485	-0.1194	0.9059	-6.4128	5.7088
BE	0.8998	2.0402	0.4410	0.6628	-3.2939	5.0935
BF	3.1386	2.0782	1.5103	0.1430	-1.1332	7.4105
CD	2.1512	3.8811	0.5543	0.5841	-5.8265	10.1290
CE	0.5215	3.5242	0.1480	0.8835	-6.7226	7.7655
CF	-2.4787	3.8615	-0.6419	0.5266	-10.4162	5.4588
DE	-3.4655	2.6807	-1.2927	0.2075	-8.9758	2.0448
DF	-1.6046	2.9485	-0.5442	0.5909	-7.6654	4.4562
EF	-0.9526	2.0791	-0.4582	0.6506	-5.2263	3.3210

Finally, selecting the factors with the lowest P-values along with the original six factors, the team chose 14 parameters to complete the regression analysis including:

1. Average particle temperature (A)
2. Receiver mass flow rate (B)
3. Receiver flow configuration (C)
4. Heat flux level (D)
5. Wind speed (E)
6. Wind direction (F)
7. Average particle temperature X Receiver mass flow rate (A x B)
8. Average particle temperature X Receiver flow configuration (A x C)

9. Average particle temperature X Heat flux level (A x D)
10. Average particle temperature X Wind speed (A x E)
11. Receiver mass flow rate X Wind direction (B x F)
12. Heat flux level X Wind speed (D x E)
13. Heat flux level X Wind direction (D x F)
14. Wind speed X Wind direction (E x F)

If these factors are combined and used to complete a regression analysis, we can see (Table 7) that there are just four factors that stand out based on their P-value.

1. Average particle temperature (A)
2. Average particle temperature X Wind speed (A x E)
3. Receiver mass flow rate X Wind direction (B x F)
4. Heat flux level X Wind speed (D x E)

Table 7. Results from regression analysis for the 14 compounded factors selected. $R^2 = 0.434$

	Coefficients	Standard Error	t Stat	P-value	Lower 95%	Upper 95%
Intercept	9.6435	2.9485	3.2706	0.0030	3.5828	15.7043
A	4.9017	2.4759	1.9798	0.0580	-0.1784	9.9818
B	-0.0013	2.0400	-0.0007	0.9995	-4.1870	4.1844
C	-0.7179	4.0029	-0.1793	0.8590	-8.9313	7.4955
D	-1.6738	3.5301	-0.4741	0.6392	-8.9169	5.5693
E	-0.0416	2.0697	-0.0201	0.9841	-4.2883	4.2052
F	0.1956	2.2643	0.0864	0.9318	-4.4503	4.8415
AB	1.1490	1.9137	0.6004	0.5532	-2.7776	5.0756
AC	2.0513	4.0507	0.5064	0.6167	-6.2600	10.3626
AD	-1.2283	3.4380	-0.3573	0.7237	-8.2825	5.8259
AE	3.1562	1.8824	1.6767	0.1051	-0.7061	7.0185
BF	2.9581	2.0175	1.4663	0.1541	-1.1814	7.0977
DE	-4.0475	2.0531	-1.9714	0.0590	-8.2602	0.1652
DF	0.2498	2.2938	0.1089	0.9141	-4.4566	4.9562
EF	-0.9262	1.8813	-0.4923	0.6265	-4.7863	2.9339

Similarly, we built a Pareto chart to determine the magnitude and compare the importance of the effects of the factors towards the particle egress rate. As seen in Figure 70, the most important factor continues to be the particle temperature. Nonetheless, the four factors highlighted in Table 7 remain statistically significant.

To conclude, these four factors and their combination suggest that there is a cumulative effect of conditions that affect particle egress rate.First, there is a direct positive correlation between average particle temperature and particle egress rate. Similarly, if the particle temperature is constant, it appears that the wind velocity would have a direct positive correlation to the particle egress rate. It would also appear that an increase in particle egress rates could be correlated to the increase of the

receiver mass flow rate and exposing the aperture to wind coming from the north side of the aperture (front). To the contrary, it appears that higher flux levels can yield diminished particle egress.

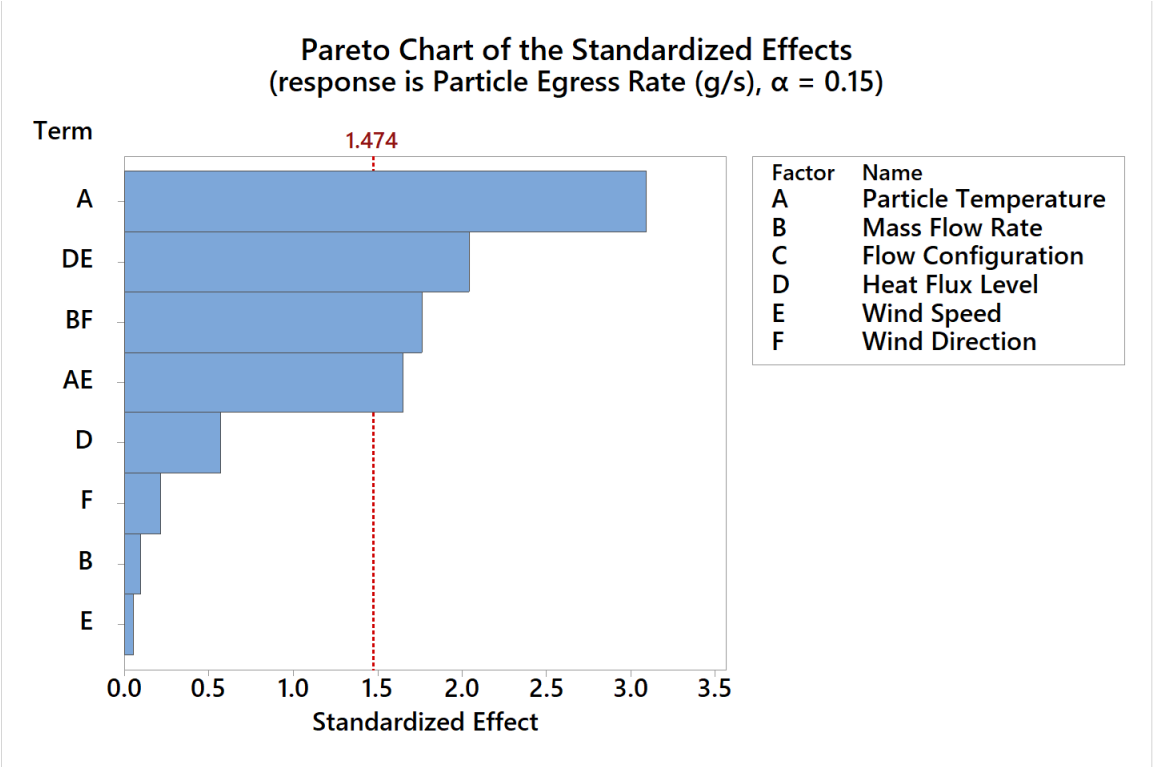

Figure 70. Pareto Chart of Standardize effects for all the factors considered in the Design of Experiments. Factors which have values greater than the reference line display statistical significance.

3.5. Data and Software Availability

The data and Matlab scripts can be accessed using the following link:

http://unm.edu/~kalmoth/fpr

3.6. Summary of Particle Imaging

In this section we discussed the development of methodology to estimate the particle egress rate and advective heat losses from the falling particle receiver. The theory behind the methodology is discussed in great detail as well as the reasons for selecting the specific models we pursued.

We continue by presenting the results of the lab-scale experiments designed and completed at the University of New Mexico which were crucial for refining the direction of the methodology and reinforcing the theory used to develop the post-processing MATLAB script.

Similarly, we continued the experimental validation during the on-sun experiments at Sandia, where multiple measurements of the particle egress were captured and analyzed. The results from these measurements were compared against the calorimetry measurements within the falling particle receiver.

These results represent the capabilities of the camera-based imaging methodology. As mentioned before, we speculate that the region within the first 100 mm of flow would more accurately capture the particle mass and heat loss. We believe that further away from the aperture, the particles can move outside the field of view and depth of focus of the cameras which can give the appearance of mass lost from the plume.

Future efforts should focus on a more thorough study that considers wind data, test temperature and mass flow rate in order to expand our database and compare the results obtained with this methodology with the results obtained by the particle sampling team.

4. PARTICLE SAMPLING METHODS

During the high-temperature falling particle receiver studies, particle sampling and modeling was conducted to quantify the particulate emission rates and loss from the receiver in relation to Occupational Safety and Health Administration (OSHA) and Environmental Protection Agency (EPA) National Ambient Air Quality Standards (NAAQS). This study was a continuation effort of bench scale tests of particulate emissions and initial experiments at the solar tower that was completed in 2018 and published in 2019 [6]. The results of the 2019 publication showed that particles with diameters less than 1 μm were observed and likely caused by deagglomeration of fine particles attached to the larger particles. The generation of larger particles (8-10 μm) was likely due to mechanical fracturing of the particles during operation. This section discusses the particle sampling methods and results of the Near-Field (< 5m) and Far-Field (>100m) techniques conducted in the Fall of 2020 and Spring of 2021.

4.1. Near-Field Sampling

4.1.1. Volumetric Air Samplers

Near-field sampling was conducted on the solar-tower platform located approximately 5 m below the solar receiver aperture which is approximately 87 m above the ground.

Near-field instrumentation placed on the platform near the aperture included several real-time particulate measurement instruments including three TSI Aerodynamic Particle Sizers (APS) and two TSI DustTrak II. Additionally, for the initial near-field studies instruments which would later be deployed on tethered balloons as part of the far-field studies were also located on the platform to provide cross-characterization data with the near-field instruments. The far-field instruments were two Alphasense N3 Optical Particle Counters, two Handix Portable Optical Particle Spectrometers (POPS) [12] and two TSI 3007 Condensation Particle Counters (CPC). Additional instruments for offline particulate analysis included two cascade impactors and custom-built tipping bucket gauges used to measure large particle deposition immediately below the receiver orifice and iMet XQ2 UAV (Unmanned Aerial Vehicle) sensors which were used to measure real-time meteorological variables.

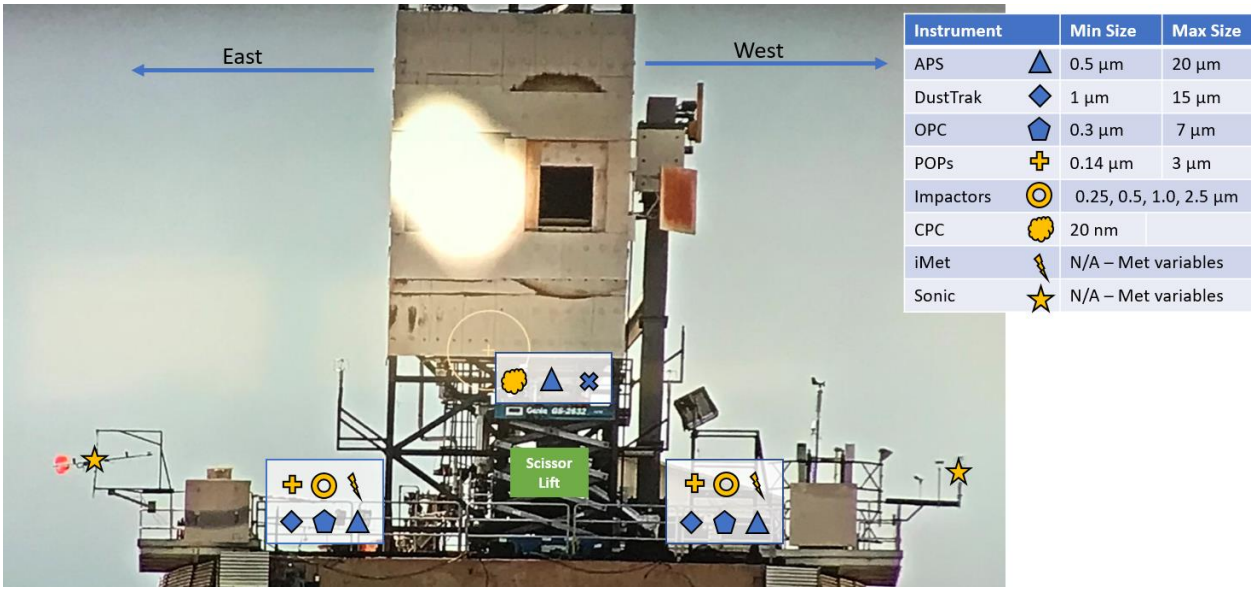

Figure 71: Near Field Particle Instrumentation Placement during On-Sun Testing.

Figure 71 illustrates the location of the aerosol samplers located on the east and west sides of the platform and scissor lift in front of the receiver aperture. The combined aerosol size distribution for all these instruments spans a range in particle sizes from 0.02 µm to 500 µm. However, it is important to note that the larger particle size measurements were limited spatially to below the aperture and were not operational for every test series.

As limited space was available on the platform the near-field instruments were situated on the north west and north east side of the platform. The instrumented areas were approximately 1 m north, 4 m west and east and 4 m below the aperture. Data collected from these instruments in real-time was sampled at varying frequencies and were synchronized and averaged over 10 seconds. These data were then analyzed post-study and a wind sector analysis was performed to filter out events where the monitors would not likely observe emissions from the aperture. As the solar aperture structure influences the local air flow, a relatively large wind sector was chosen with wind directions within a 40° sector centered around the prevailing wind direction chosen.

4.1.2. Near Field Results and Discussion

4.1.2.1. Preliminary Studies

Initial near-field sampling was conducted on August 17, August 18, September 3 and September 4, 2020. Data collected on September 3 will be discussed below, as this dataset is the most extensive. Earlier tests had instrument issues including data loss and no tipping bucket collectors were used. During the testing on September 3, the prevailing wind was generally from the west-north-west (292.5°) as measured by a sonic anemometer mounted on the solar tower. There was some variation in wind direction with winds blowing from the west-south-west (247.5°) to north-north-west (337.5°) with higher wind speeds up to 12 m/s observed as shown in Figure 72. Based on the prevailing winds it is assumed the west monitoring location will be classified as the "upwind" monitoring location not influenced by the solar tower operation and the east monitoring location will be the "downwind" monitoring location and will be impacted by the operation of the solar tower and particulates emitted from the aperture.

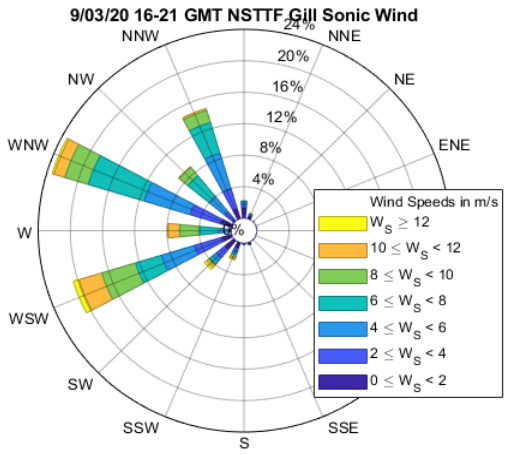

Figure 72: Wind Rose Depicting Wind Speed and Direction on September 3, 2020.

The total mass and number concentration as a function of particle size are measured by the APS and OPC and are shown in Figure 73 and Figure 74 respectively at both the east and west monitoring locations for the test conducted on September 3. The data plotted is the cumulative distribution for aerosol concentrations larger than the size range indicated in the legend. As the figures show there are multiple spikes in aerosol mass and number concentration at particle diameters ranging up to 5 µm, with number concentrations on the order of 150 cm^{-3} and mass concentrations of 0.15 mg/m^3. Increases in larger particle concentrations can also be seen in the OPC data (Figure 74). The spikes in the aerosol concentrations can be attributed to events occurring at the solar tower aperture and the local micrometeorological wind conditions. As Figure 74 shows the small particle (0.35 to 0.40 µm) concentration on the east side of the aperture is higher, by approximately 50 %, throughout the study and during high concentration events under prevailing winds from the west-north-west. A wind sector analysis was then conducted on this data to filter out wind conditions not conducive to transport of aerosol to the monitors. This type of analysis filters out data based on the preliminary wind direction and speed as measured by the solar tower sonic anemometer.

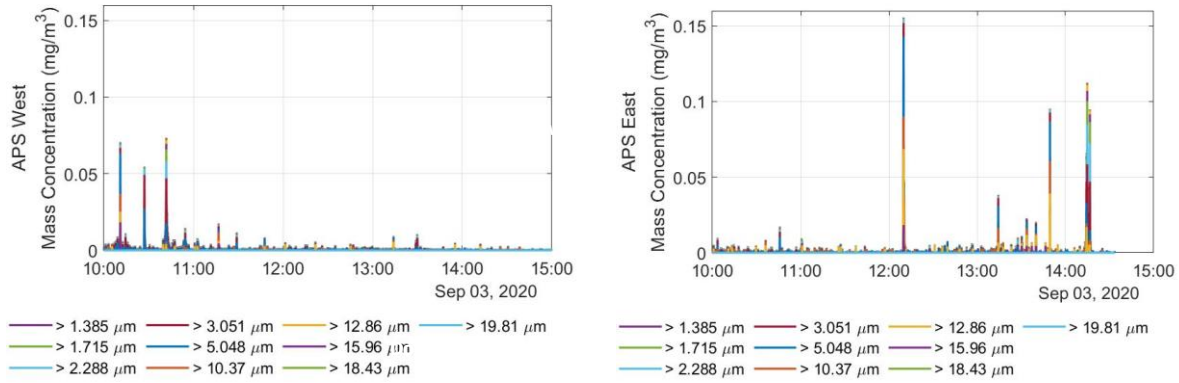

Figure 73: Cumulative Mass Size Distributions Measured by the APS for Both the East and West Locations.

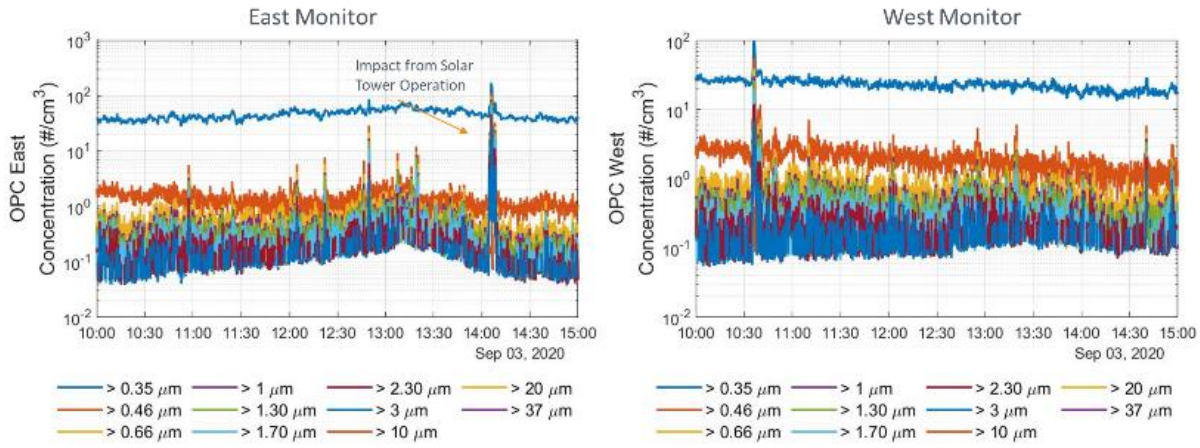

Figure 74: Cumulative Number Size Distributions Measured by the OPC for the Both the East and West Locations.

Wind sectors of interest were determined by identifying the direction of the monitor placements (east and west) of the aperture and the associated wind direction which would advect a plume to these locations. The results of this analysis for the September 3, 2020 data are shown in Figure 75, where the wind sector for plume advection was blowing from 275-315 ° towards the east (downwind) monitor. The left panels of the figure show the full wind direction and speed during the testing (top panel), the lower panel indicates wind direction and speeds that occur only when the wind is blowing from 275-315 °. The right panels of Figure 75 show the mass and number concentration for all the data (top panel) and for the concentrations under the wind direction condition (lower panel). As the figure shows there are increased concentration events on the downwind monitoring locations in both the APS and OPC measurements associated with wind advected from the sectors of interest transporting aerosol from the solar receiver.

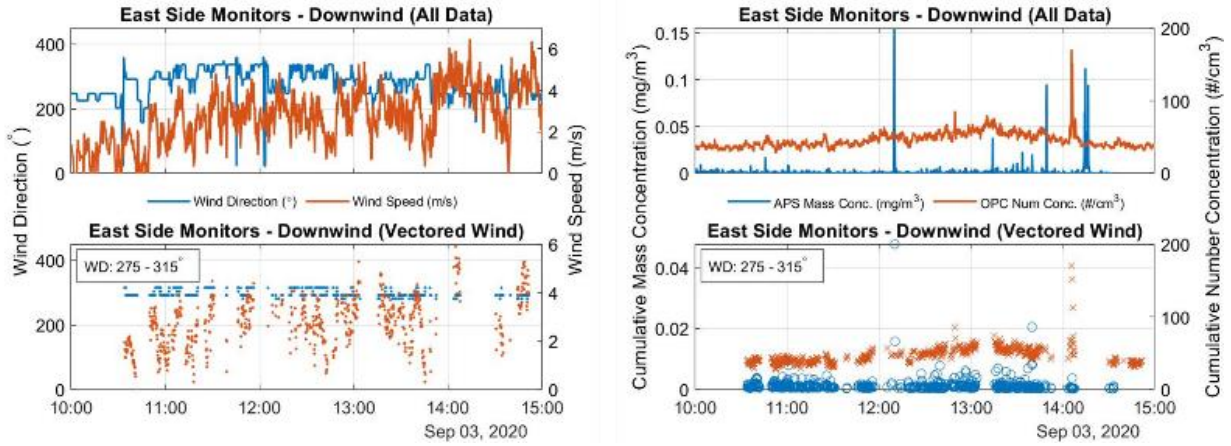

Figure 75: Downwind Wind Sector Analysis for the East Monitoring Locations Using Both the APS and OPCs.

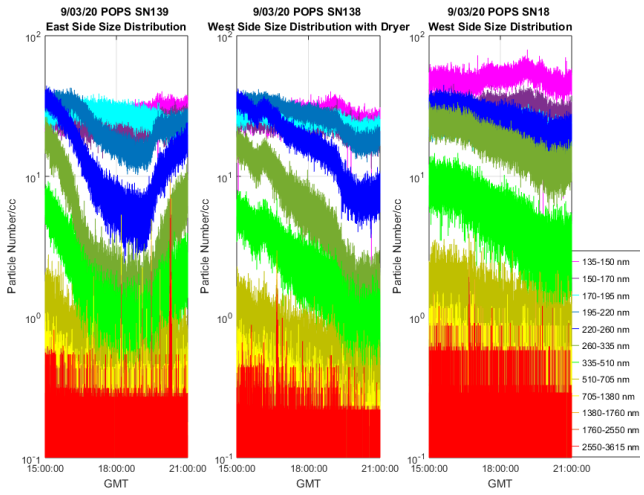

Figure 76: Number Size Distributions Measured by the POPS for Both the East and West Locations.

The aerosol size concentrations from 135 to 3615 nm collected by the POPS on September 3, 2020 are shown in Figure 76. The time series of these distributions indicate similar particle size distributions and total number concentrations on both the upwind and downwind sides of the solar receiver.

Aerosol size distributions as measured by the APS and OPC are shown in Figure 77 for the maximum concentration events shown in Figure 73 and Figure 74. The left panel shows the downwind east monitor and the right panel is the upwind west monitor. Data is taken from two different events, the OPC number distribution data is for a maximum concentration event occurring at 14:05 and the APS mass concentration data is from an event occurring at 12:10. As the figure shows there is a significant increase in the overall size distribution between the downwind and upwind with a mode diameter in the 1-2 μm for the number distribution and the mass distribution dominated by the larger particle sizes due to the relatively high density of CARBO HSP at 3,600 kg/m3.

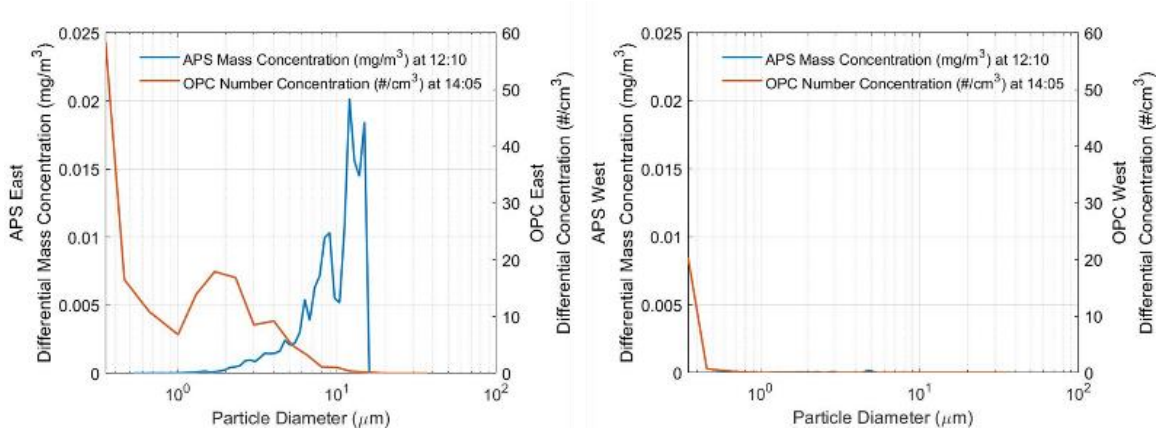

Figure 77: APS and OPC Aerosol Size Distributions Measured at Maximum Downwind Concentration Events.

4.1.2.2. Fall 2020 Data: One-Stair TBS Study

On November 3rd, 2020, a near-field study was conducted in conjunction with the first Tethered Balloon System (TBS) deployment with a "one-stair" receiver configuration. The additional stair was intend to direct the CARBO material closer the aperture opening. During this study, the POPS, OPC, and APS systems were set in place on top of the Solar Tower platform approximately 5m below the receiver. The APS and OPCs were placed on the northeast and northwest sides of the platform, while the POPS was placed on the northeast side of the platform. Wind speed and direction were recorded on the platform using a sonic anenometer, Figure 78. As indicated on the wind rose, the prevailing winds during November 3rd were from south-south-west at a speed greater than 6m/s.

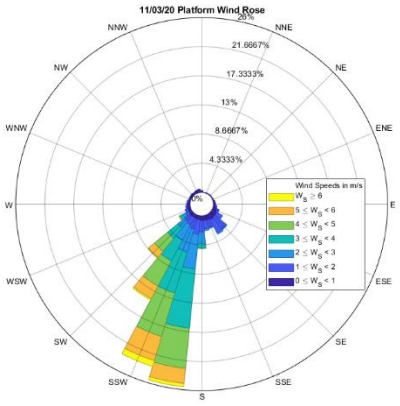

Figure 78: Wind Rose of Wind Speed and Direction during the TBS Study on November 3rd, 2020.

One stationary Portable Optical Particle Spectrometer (POPS, SN139) was placed 5m below the receiver, on the northeast side of the platform. The data collection from the POPS reported total concentration within a particle size range of 0.135-2.55µm. Figure 79 are plots of the concentration measured by the POPS during the study. In the data, the concentration increased during the start of the study and steadily decreased in concentration with the increased receiver temperature throughout the day. Additionally, the prevailing particle sizes were less than 260nm throughout the test.

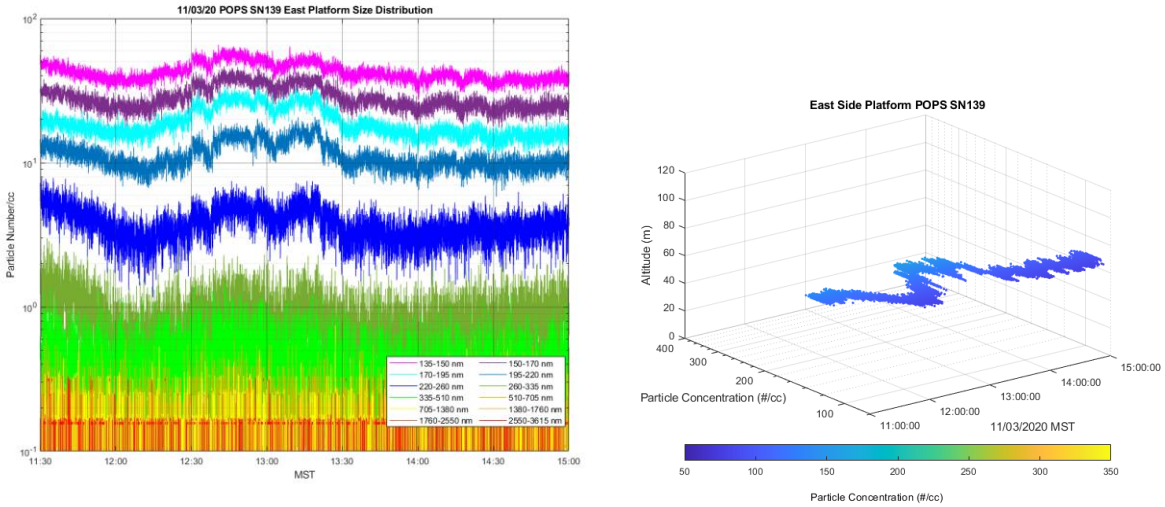

Figure 79: POPS Concentration and Size Data vs. Time (Left) and Total Concentration vs. Time (Right).

Two Optical Particle Counters (OPCs) were used during this study, however, only data from the northeast OPC showed promising results. The OPCs measure total concentration in the particle size range of 0.335-37µm. In Figure 80, the data shows steady concentrations over the study with slight increase of concentration of the >0.35µm particulates starting at 12:00 and decreasing around 13:30.

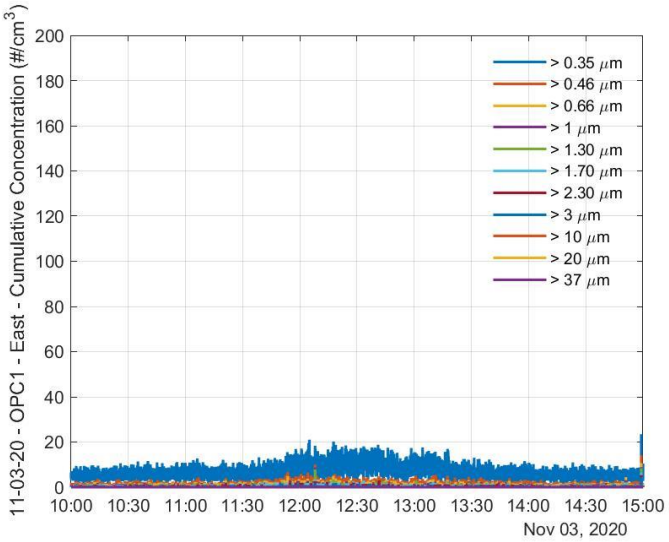

Figure 80: East OPC concentration vs. time from November 3rd.

The APS mass distributions are shown in Figure 81 for the east and west side locations on November 3. The data shows a number of spikes in concentration for particles smaller than approximately 5 µm on both sides of the tower. These spike events are likely to have occurred when the particles were falling from the receiver during calmer winds or when the air flow around the structure allowed for mixing of air to the platform level. The spikes shown increased concentrations to over six times the "nominal" background concentrations.

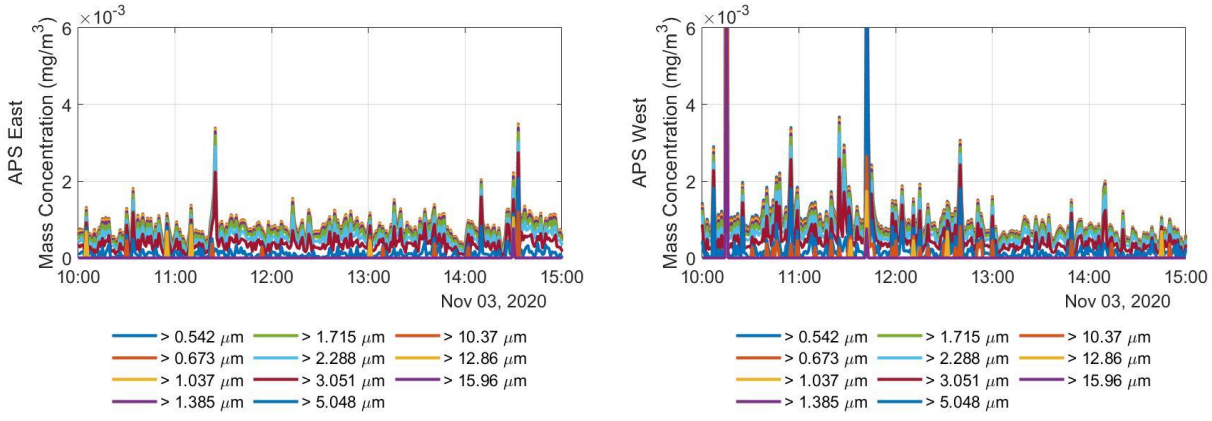

Figure 81. APS mass concentration distributions from the APS instrument (November 3, 2020).

4.1.2.3. Spring 2021 Data: Free-Falling TBS Study

On March 7th, 2021, a near field study was conducted in conjunction with the second Tethered Balloon System (TBS) deployment with a "free-falling/no-stair" receiver configuration. The "free-fall" configuration removed the additional stair that directed the CARBO material closer to the aperture opening, meaning the beads were farther inside the receiver. During this study, the POPS, OPC, and APS systems were set in place on top of the Solar Tower platform approximately 5m below the receiver. The APS and OPCs were placed on the northeast and northwest sides of the platform, while the POPS were placed on the north (downwind) and south (upwind) sides. Wind speeds and direction were recorded on the upwind and down wind balloons measured by an anenometers, Figure 82. From the wind data, prevailing wind was generally from the south-west and south-south-west directions under 6 m/s, meaning winds were lower on this day that then were in the fall. Additionally, wind speed was fairly stable throughout the day with a bit of directional shift from 12:30 to 14:00, which is also the time when the wind speed decreased, Figure 83.

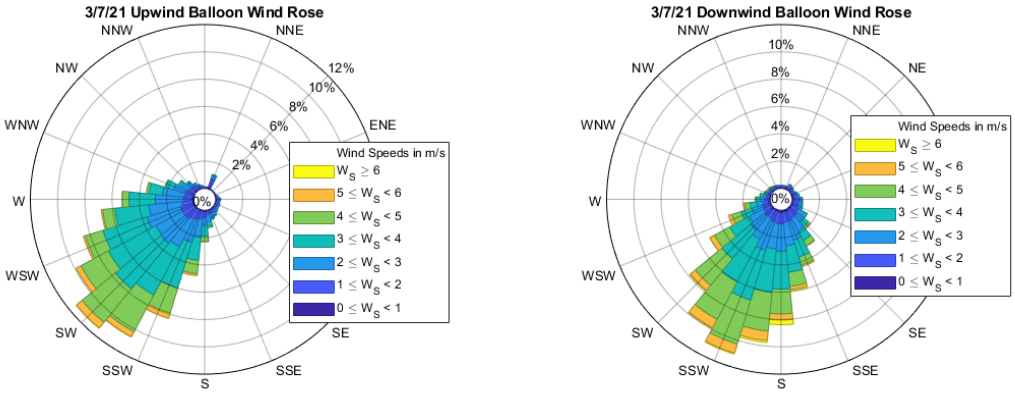

Figure 82: Wind Rose Depicting Wind Speed and Direction on March 7th, 2021.

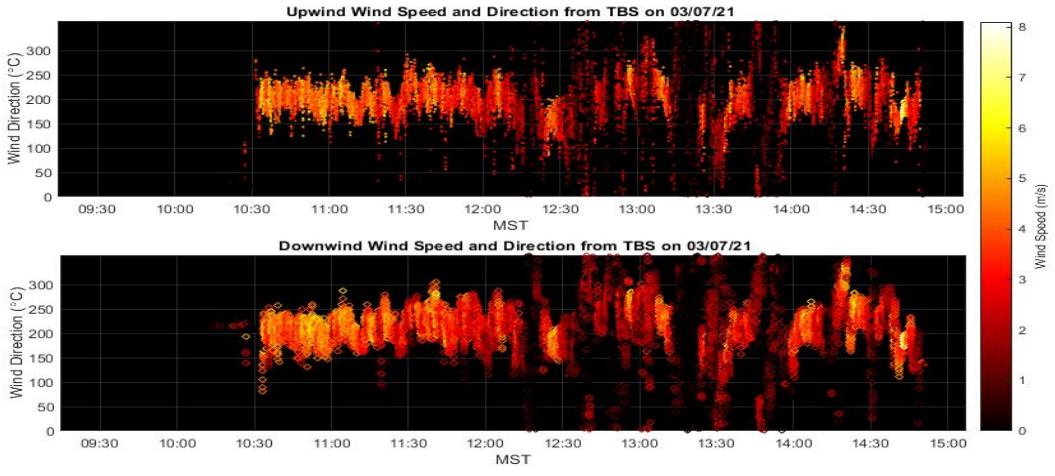

Figure 83: Upwind and Downwind Wind Speed and Direction vs. Time.

Two stationary Portable Optical Particle Spectrometer (POPS) were placed 5m below the receiver, on the north (downwind, SN138) and south (upwind, SN139) sides of the platform. The data collection from the POPS reported total concentration within a particle size range of 0.135-2.55μm.

Figure 84 is a plot of upwind and downwind total concentrations over time (top) and includes a plot of temperature of the receiver over time (bottom). In this figure, both POPS peaked in concentration at the beginning of the study around 10:00, which is consistent with measurements seen in other instruments. Additionally, the downwind POPS concentration minimum occurs immediately after the maximum receiver temperature is reached around 12:00, which was observed on 11/03/2020. Finally, both POPS concentrations converge at 13:30, 90 minutes after the receiver temperature peaks. It is important to note, this is also the time when winds were at its calmest during the study.

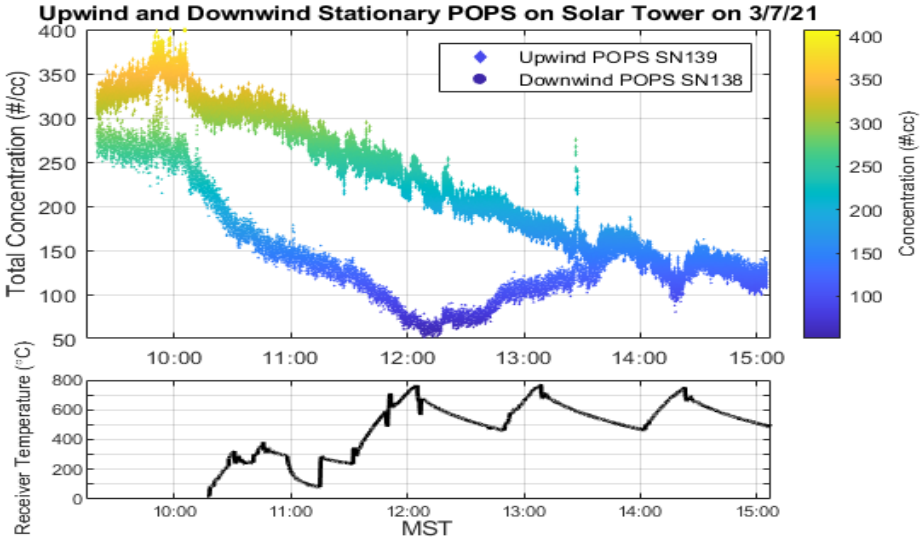

Figure 84: Upwind and Downwind POPS Concentrations vs. Time (Top) and the Receiver Temperature Measurements vs. Time (Bottom).

Two Optical Particle Counters (OPCs) were placed about 5m below the receiver, on the northwest and northeast sides of the platform. The OPCs measure total concentration in the particle size range of 0.335-37μm. Figure 85 are plots of the West (Left) and East (Right) OPC concentrations over time. From Figure 82, the prevailing winds were from south-west, meaning that trajectory of the particulates would likely follow the East side of the platform. As seen in the plots below, little to particulates were seen from the west side of the platform, whereas the east side saw in increased spike in concentration at the start of the study and relatively steady concentrations throughout the day.

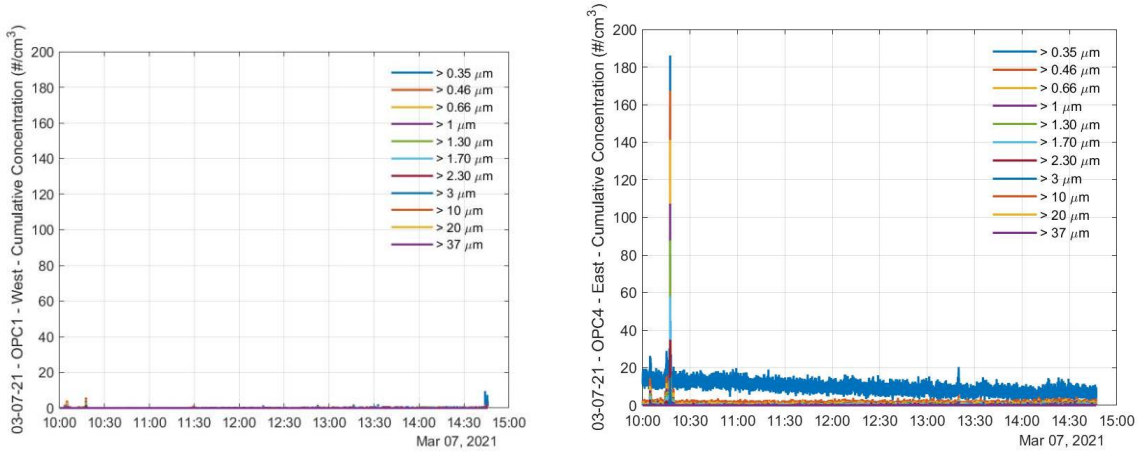

Figure 85: West and East OPC Concentrations vs. Time.

The APS mass distributions are shown in Figure 86 for the northwest and northeast sides of the platform. The data shows a number of spikes in concentration for particles smaller than approximately 5 μm on both sides of the tower. These spike events are likely to have occurred when the particles were falling from the receiver during calmer winds or when the air flow around the structure allowed for mixing of air to the platform level. This data, unlike that from November 3rd, does not show a spike in concentration at the start of the receiver, this might be due to position of the instruments or low wind speed conditions.

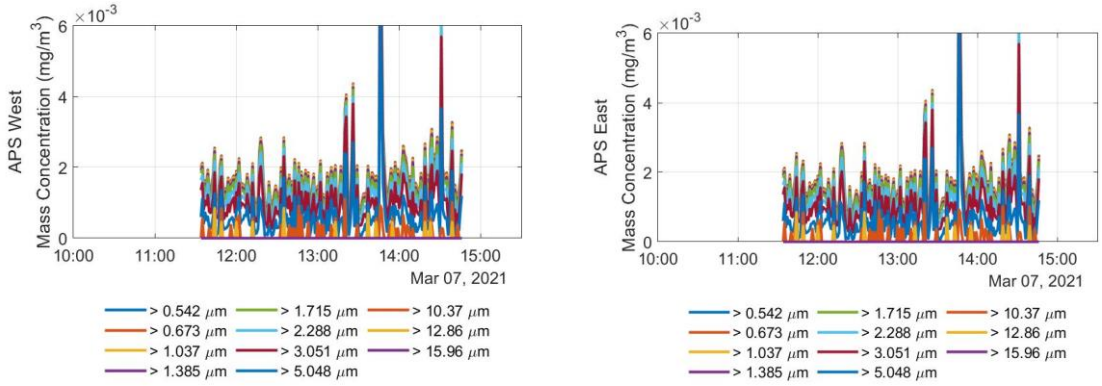

Figure 86: APS mass concentration distributions from the APS instrument (April 7th, 2021).

4.1.3. Tipping Buckets

In addition to real-time sampling of smaller particles advected by the wind, larger particle loss with sizes between 150 and 500 μm were collected using two versions of custom-designed tipping buckets. The size range of sampling with the tipping bucket was limited by the sieve mesh used to screen the collected particles post sampling. The prototype bucket was composed of a 10.1 cm diameter 3D-printed PLA (polylactic acid) cone which funneled particles into a tip mechanism that blocked an LED diode and photodetector circuit when tipped. Images of the prototype design, prototype unit and three full-scale tipping buckets can be seen from left-to-right in Figure 87. Each

tip contained 0.6 +/- 0.05 g of CARBO HSP. The second iteration of the bucket used a 58.4 cm diameter 3D-printed PLA cone and an identical tipping mechanism.

Figure 87: PLA Tipping Bucket Design, Preliminary Prototype and Full-Scale Setup.

The prototype tipping bucket was deployed during near-field testing on September 3 - 4, 2020 using a fully-extended scissor lift 0.3 m north and 0.3 m below the receiver aperture to collect falling particles. The detected tips on September 3rd were plotted against the total solar tower receiver hopper weight in Figure 88. The y-axis of the figure is the upper hopper total weight which is the amount of material loaded above the aperture. As the receiver is in operation the CARBO HSP particles fall from the upper hopper into the lower hopper through the aperture, the lower hopper is then recycled to the upper hopper through an elevator until a close to steady state condition of operation is met. The red data points are when the tipping bucket tips and counts 0.6 g of CARBO HSP particles. Each tip is summed to identify a cumulative mass measured for the day. The total weight of particles collected on each day under each receiver configuration was 11.5 and 23.6 g. Converting these total particle weights collected with the 10.1 cm-diameter tipping bucket results in an estimated 1.12 and 2.31 kg over a 1 m-diameter surface area on September 3rd and 4th.

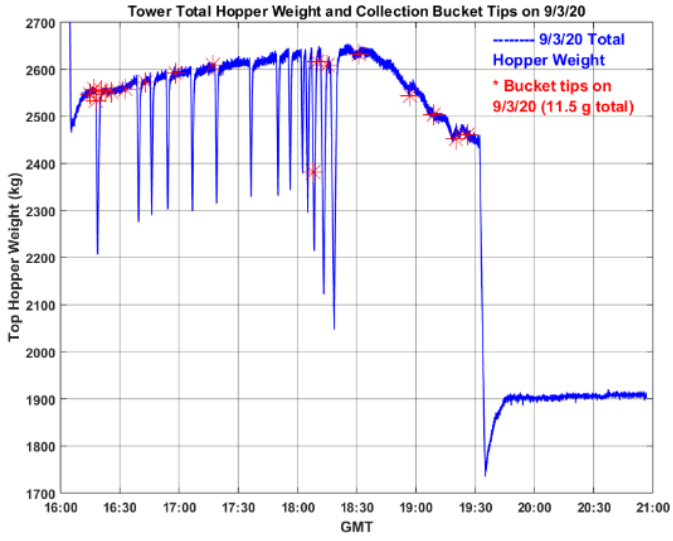

Figure 88: Tipping Bucket Weights vs. Time for September 3rd, 2020.

Three full-scale tipping buckets were across the scissor lift during near-field testing on October 23 and December 22, 2020 and during far-field testing on November 3, 2020 and March 7, 2021. Total collected particle masses the extrapolated particle masses over a larger area, primary wind direction, and solar tower configuration are shown for each tipping bucket deployment in Table 8.

Table 8: Full-Scale Tipping Bucket Results from Each Deployment.

Datetime (MT)	Bucket #	23" diameter total mass (g) MEASURED	5' diameter total mass (kg) ESTIMATED	Primary Wind Direction (°)	Receiver Configuration
10/23/2020 11:00 - 14:30	1 (East)	947	6.44	E	2-stair
10/23/2020 11:00 - 14:30	2	1696	11.53	E	2-stair
10/23/2020 11:00 - 14:30	3 (West)	2102	14.29	E	2-stair
11/03/2020 11:30 - 15:00	1 (West)	1400	9.54	SSW	PID
11/03/2020 11:30 - 15:00	2	4010	27.28	SSW	PID
11/03/2020 11:30 - 15:00	3 (East)	4900	33.34	SSW	PID
12/22/2020 12:15 - 14:00	1 (East)	21	0.14	S	Freefall
12/22/2020 12:15 - 14:00	2	19	0.13	S	Freefall
12/22/2020 12:15 - 14:00	3 (West)	27	0.18	S	Freefall
03/07/2021 11:00 - 15:00	1 (East)	36	0.25	SW	FPR
03/07/2021 11:00 - 15:00	2	31	0.21	SW	FPR
03/07/2021 11:00 - 15:00	3 (West)	14	0.09	SW	FPR

The particles collected with the three tipping buckets during the far-field test on November 3, 2020 were sieved to determine their size distribution and these results are shown in Figure 89. Over 90% of the particles in each bucket were between 300-500 µm, with almost all of the remaining particles measuring 150-300 µm.

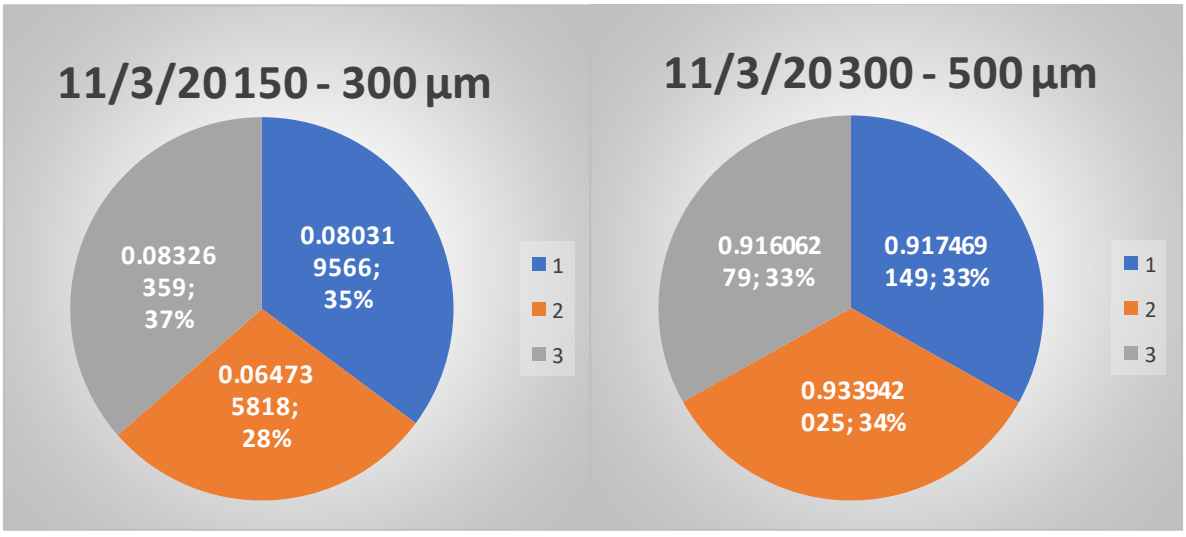

Figure 89: Percentage of Sieved Particle Size Weights from Three Full-Scale Tipping Buckets.

The frequency of tips within the buckets indicated that that majority of the particle emissions occur early-on in the solar receiver test. A tip is indicated by a '*' symbol in the plot of tipping frequency from November 3, 2020 shown in Figure 90.

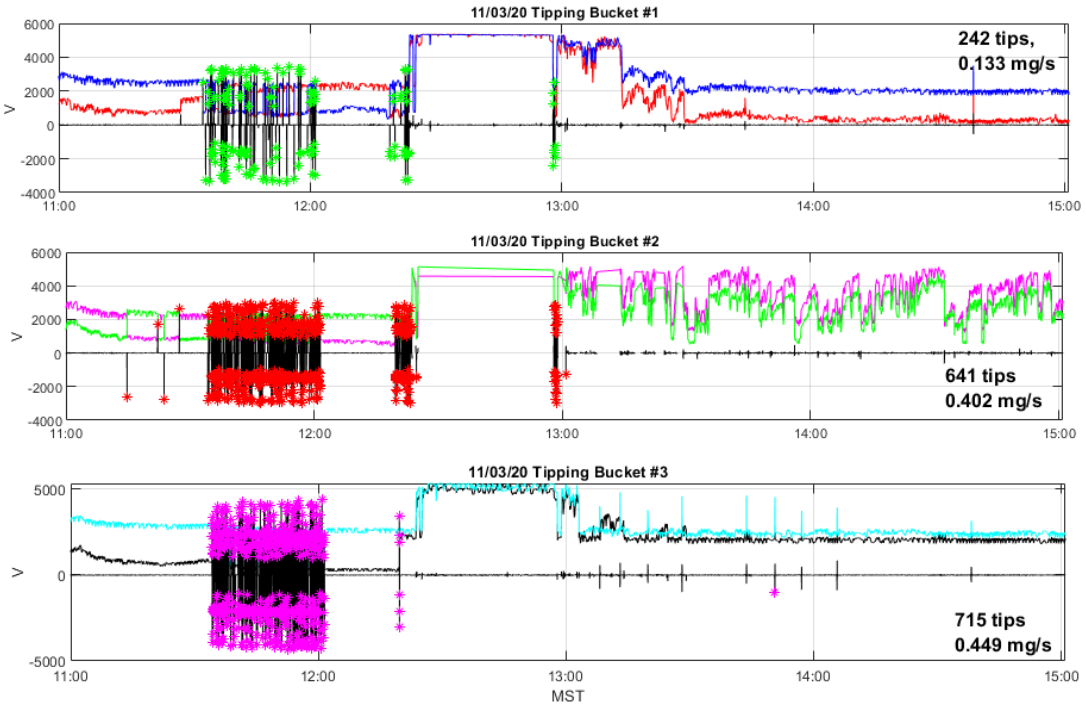

Figure 90: Frequency of Tips During September 3rd, 2020 Deployment.

4.2. Far-Field Sampling – Tethered Balloons

Tethered Balloon Systems (TBS) were used for assessing the far-field concentrations of aerosol released from the solar tower aperture. The TBS had four main instruments, in various configurations, onboard during the experimental study. These instruments were:

- CPC: Real-time measurement of aerosol concentration for particle diameters in the range of 0.01 μm < Dp < 1.0 μm.
- POPS: Real-time measurement of size resolved aerosol concentration for particle diameters in the range of 0.135 μm < Dp < 2.55 μm.
- OPC: Real-time measurement of size resolved aerosol concentration for particle diameters in the range of 0.335 μm < Dp < 37.0 μm.
- STAC: 4-Stage impactor measurement (0.1-5.0μm)

During the far-field measurements the Solar Tower Receiver had two different configurations for the particle receiver:

- One Stair – November 3, 2020
- Freefall (No Stair) – March 7, 2021

Three tethered balloon systems were deployed to undertake far-field sampling on November 3, 2020 as depicted in Figure 91. Winds were blowing from the south-south-west resulting in a compromised ability to deploy the balloons directly downwind of the solar tower. The instrumentation sited on the tower (APS, OPC) deployed during the near-field sampling was also deployed on the tower during the far-field sampling and additional OPC, POPS and CPCs were deployed on the tethered balloons. The payloads were suspended at approximately 100 m Above Ground Level (AGL) using the tethered balloons. The balloon designated "Downwind 1" was utilized as a profiler and oscillated in altitude from approximately 50 m to 140 m AGL.

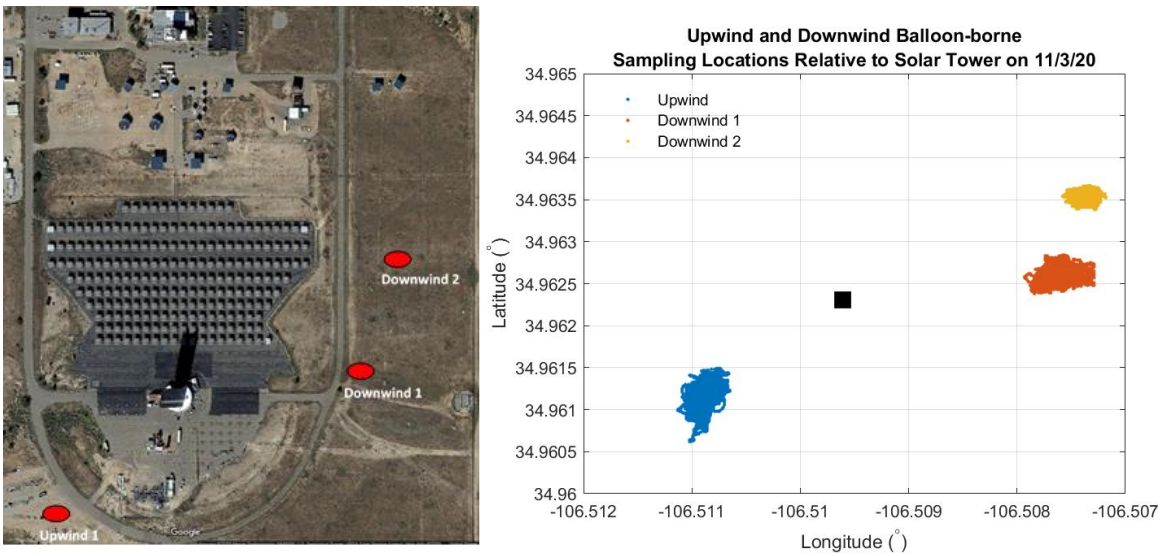

Figure 91. Measurement locations during November 3, 2020 TBS deployment.

Two tethered balloon systems were deployed again on March 7, 2021. During this subsequent deployment, the upwind balloon remained stationary in both altitude and position on the southwest side of the solar tower while the downwind balloon traveled around the northeast quadrant of the facility while intermittently ascending and descending in response to real-time data from the POPS in flight. The two-dimensional sampling locations of both balloons are shown in Figure 92.

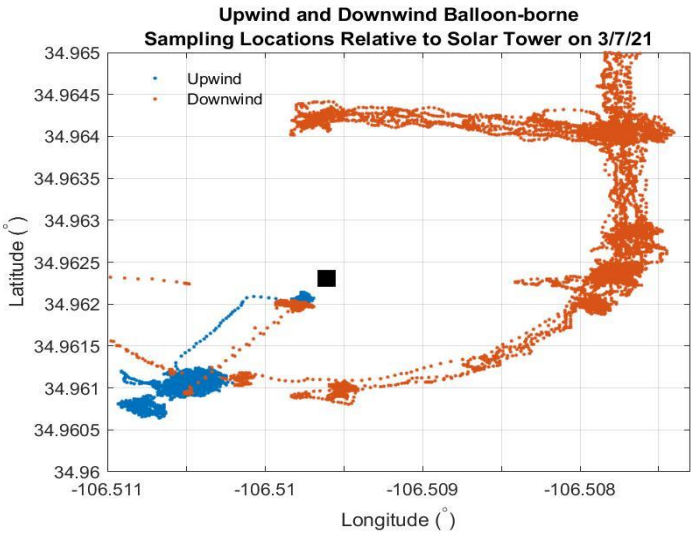

Figure 92: Two-Dimensional Sampling Locations on March 7th, 2021.

4.2.1. Condensation Particle Counter (CPC) Data

The CPC measures total number concentration of particles in the size range of 0.01 < Dp < 1.0 μm. As shown in Figure 93, on both far-field test days the downwind CPC measured an approximate 50% reduction in particle concentration when compared to the upwind CPC. The upwind CPC also measured an approximate 25% reduction in particle concentration approximately one hour after the receiver going on-sun.

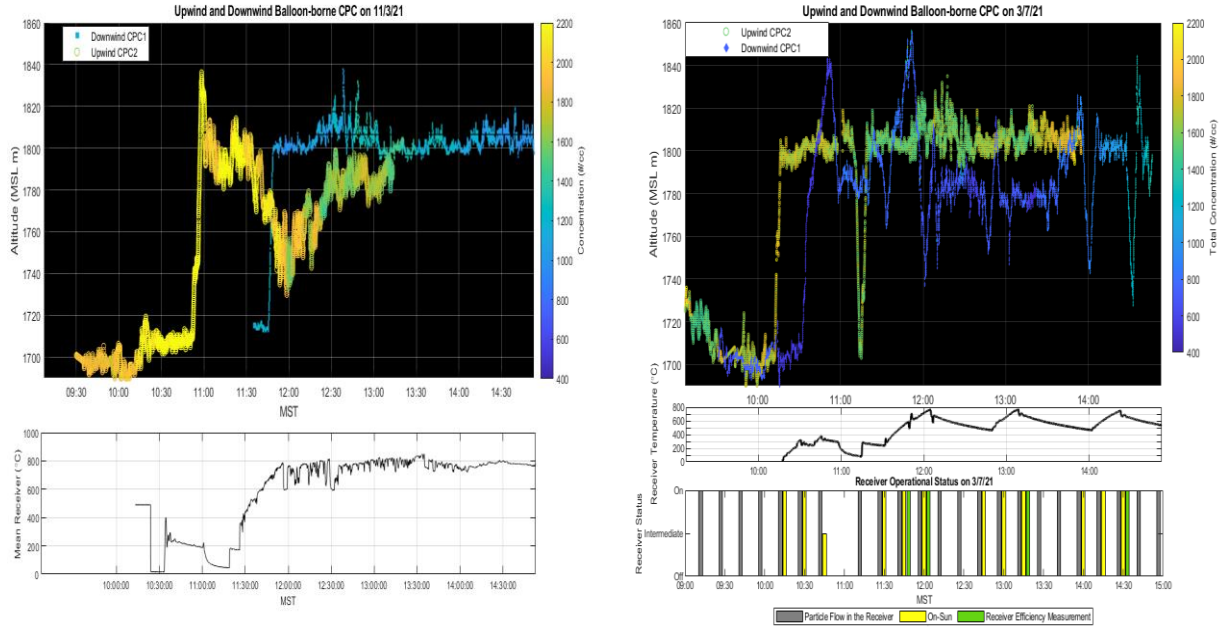

Figure 93: CPC Concentrations According to Altitude of Upwind and Downwind TBS on November 3rd, 2020 (Left) and March 7th, 2021 (Right).

Figure 94 depicts a 3D representation of CPC measurements from all of the locations sampled by both balloons on November 3rd (left) and March 7th (right) with the solar tower location depicted in

red. The overall reduction in particle concentration measured by the downwind balloon in comparison to the upwind balloon is apparent on both days. On March 7th, the highest concentrations measured by the downwind balloon occurred when the balloon was on the far western and southern edges of the measurement area, which were the areas furthest upwind relative to the southwesterly wind direction.

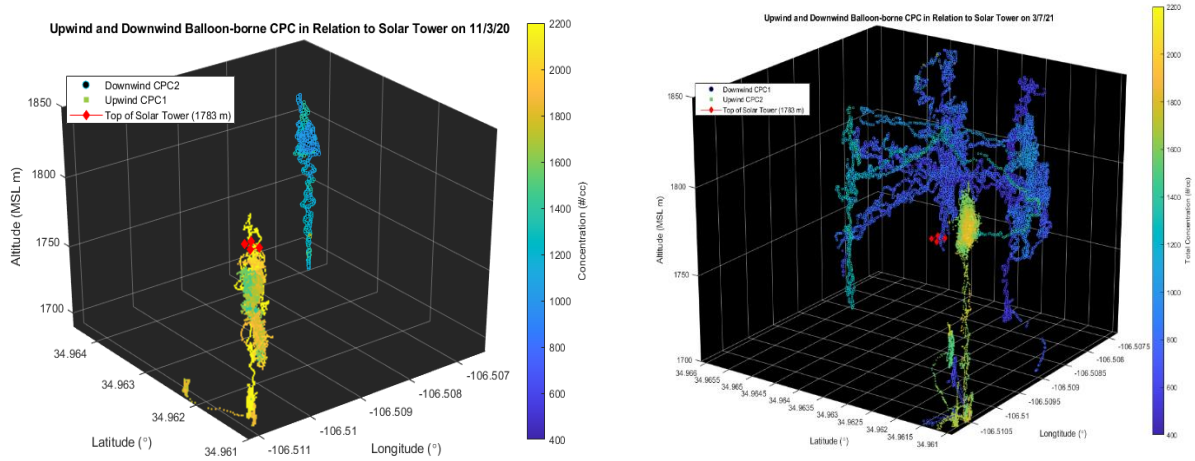

Figure 94: CPC Concentrations with Respect to Time from November 3rd, 2020 (Left) and March 7th, 2021 (Right).

The time of the measurement is plotted vertically against the 2D locations of the upwind and downwind balloon CPC measurements collected on November 3rd (left) and March 7th (right) in Figure 95. The gradual decrease with time in the upwind CPC concentration is observed on both test days, and the downwind CPC concentrations measured on March 7th do not depict a significant change with respect to time. The lack of change with time emphasizes that the location of the measurement, as depicted in the previous figure, typically has a greater impact on the downwind CPC concentration than the time that the samples were collected.

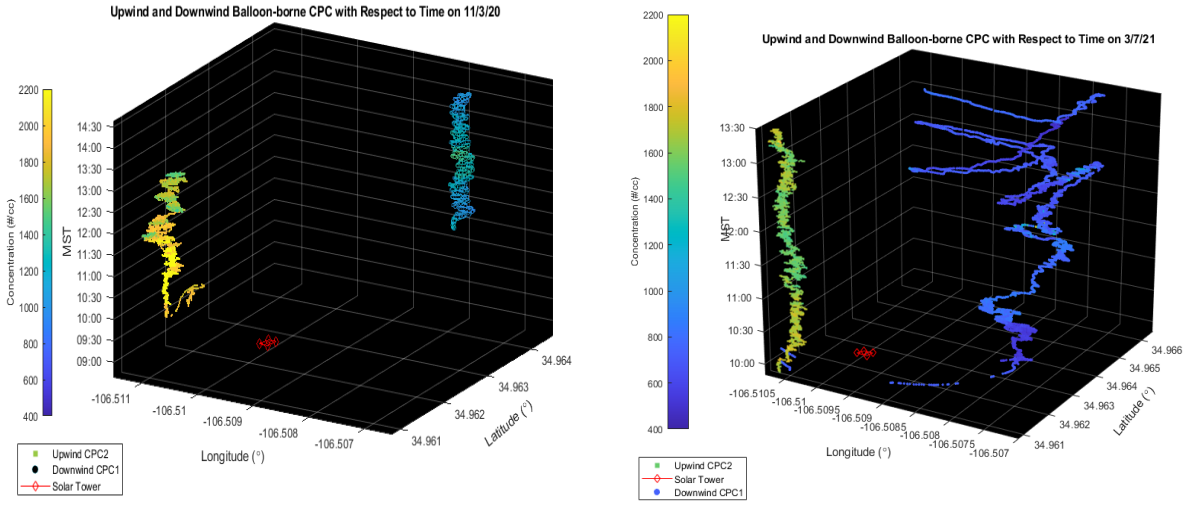

Figure 95: CPC Concentrations with Respect to Time from November 3rd, 2020 (Left) and March 7th, 2021 (Right).

4.2.2. Portable Optical Particle Sizer (POPS) Data

On November 3, the downwind POPS measured a shift to larger particle diameter, 1 – 1.5 micron, when the receiver temperature peaked around 12:00, Figure 96. This shift was not observed in the downwind balloon POPS data on March 7, and could be related to the increased particle emissions from the tower observed during the first far-field test.

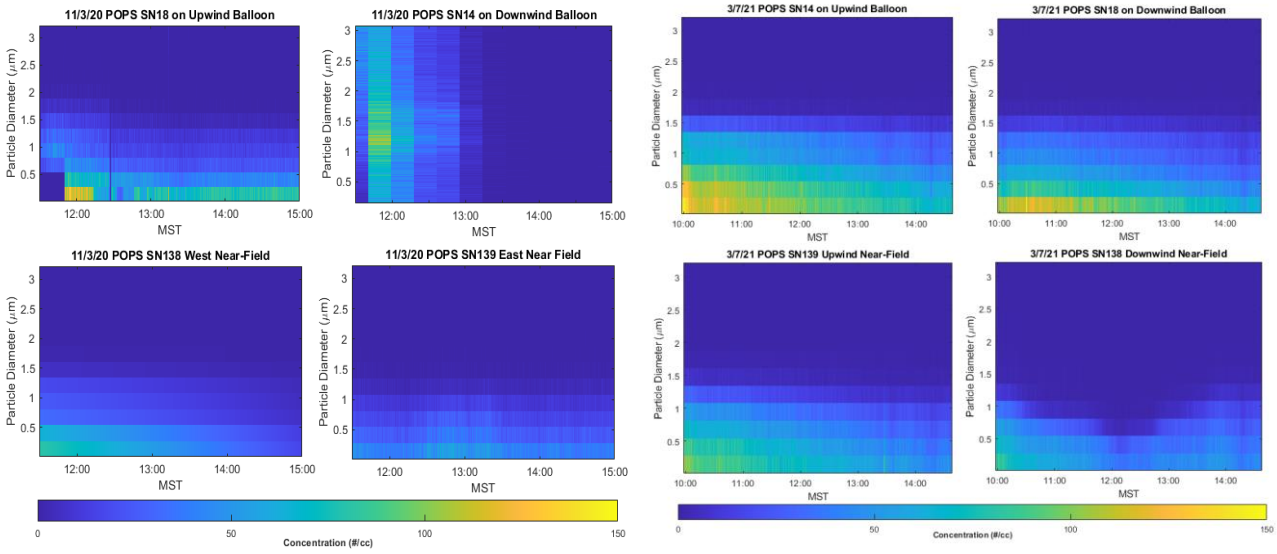

Figure 96: POPS Data from November 3rd, 2020 (Left) and March 7th, 2021 (Right).

On November 3, the downwind POPS measured approximately 30% higher concentration than the upwind POPS, with maximum concentration being measured by the upwind POPS for an approximate one-hour period from 12:30 – 13:30, roughly one hour after the receiver going on-sun, Figure 97. In comparison on March 7, both the upwind and downwind POPS reported similar concentration for the entire test period, and both observed a gradual decrease in particle concentration with time.

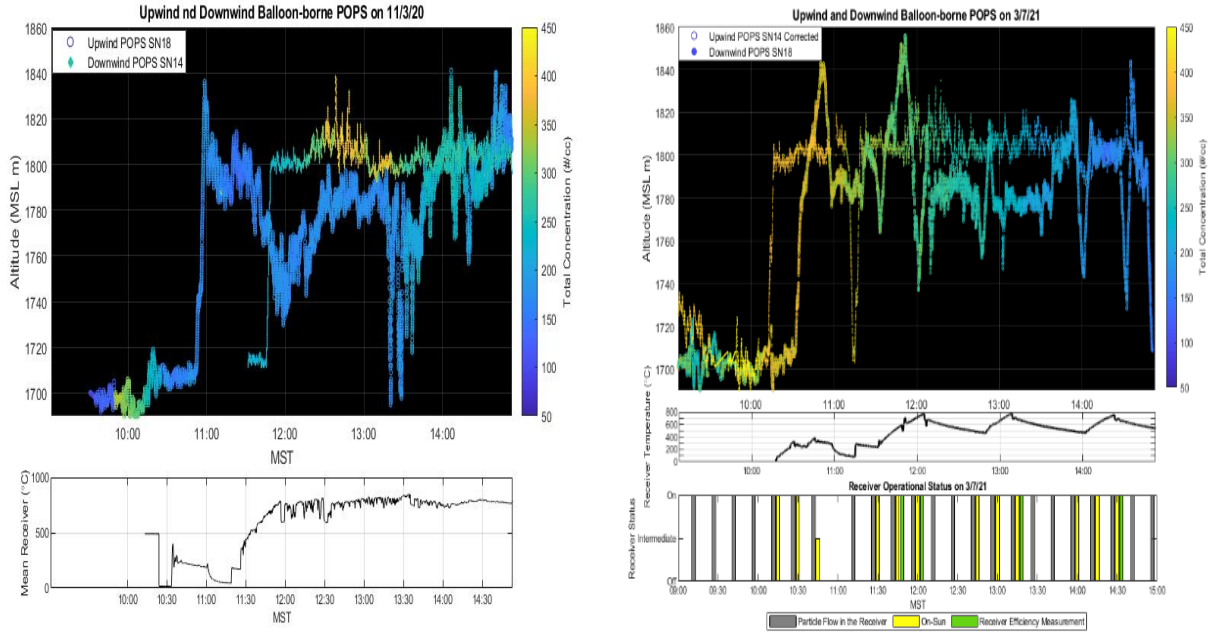

Figure 97: POPS Concentrations According to Altitude of Upwind and Downwind Tethered Balloon Systems (TBS) on November 3rd, 2020 (Left) and March 7th, 2021 (Right).

Figure 98 depicts POPS concentration measured by the upwind and downwind balloon with respect to the 3D spatial sampling location on November 3 (left) and March 7 (right). On November 3 when the downwind balloon was stationary the highest concentrations were measured at the maximum altitude of the balloon. This result is consistent with previous AERMOD models of particle emissions for the light winds (2-4 m/s) experienced on November 3 (Ho and Pattyn, 2020). The wind roses for each day are shown in Figure 99.

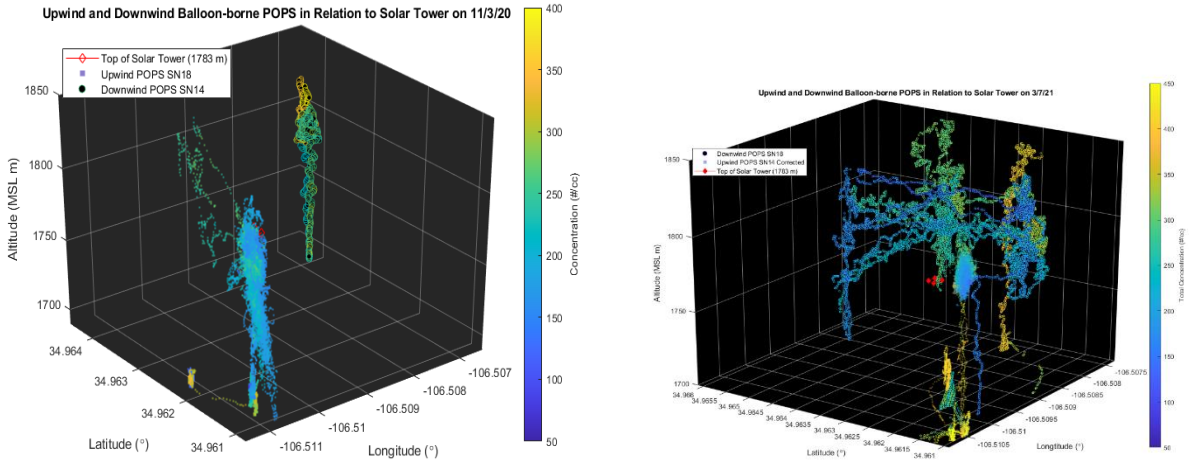

Figure 98: 3D Spatial TBS POPS Data Upwind and Downwind on November 3rd, 2020 (Left) and March 7th, 2021 (Right).

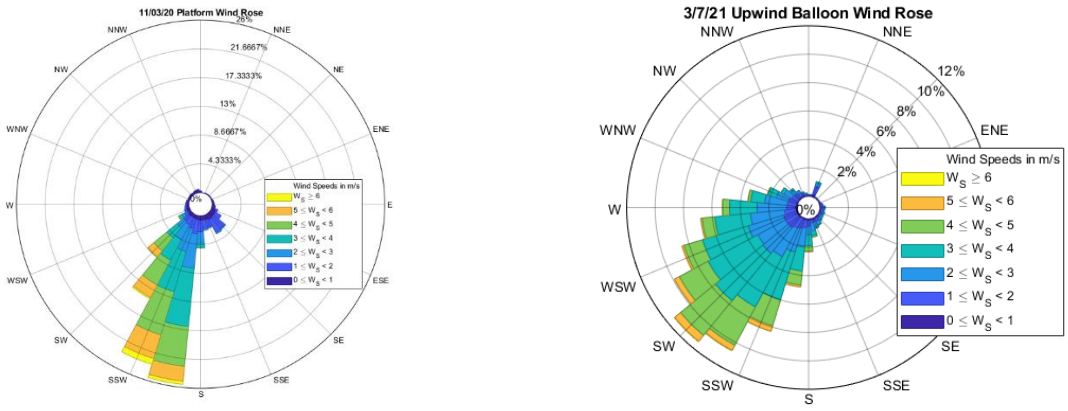

Figure 99: Wind Rose from November 3rd, 2020 (Left) and March 7th, 2021 (Right).

Figure 100 depicts POPS concentrations measured by the upwind and downwind balloon with respect to time on November 3 (left) and March 7 (right). On March 7 both POPS measured gradually decreasing particle concentration with respect to time. On November 3 the downwind particle concentration increased by 100% from 12:30 – 13:30, approximately one-hour after the receiver going on-sun. The particle masses collected by the tipping buckets on November 3 were up to 130 times greater than the masses collected by the buckets on March 7, and this relative increase in particle emissions from the tower is likely a contributing factor to why this increase was observed in the downwind POPS concentration on November 3 but not on March 7.

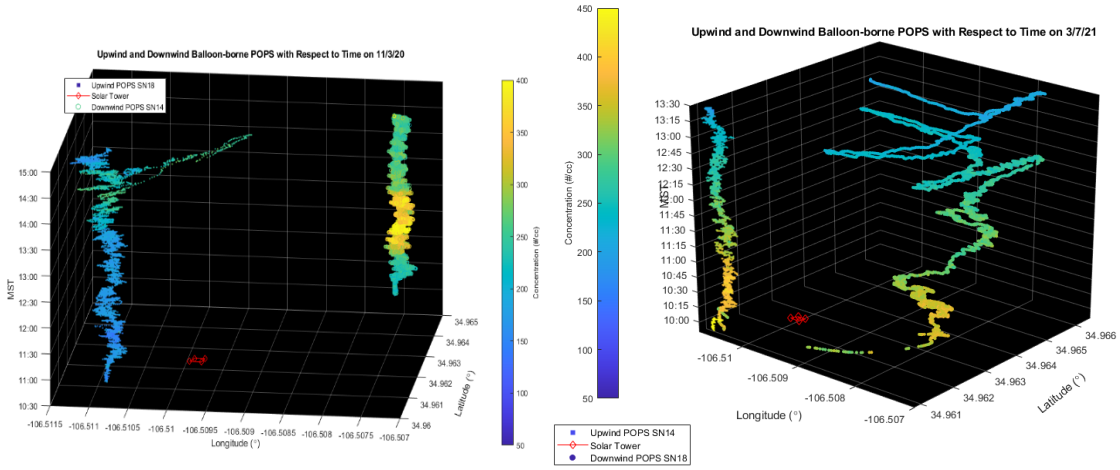

Figure 100: POPS Concentrations with Respect to Time from November 3rd, 2020 (Left) and March 7th, 2021 (Right).

4.2.3. Optical Particle Counter (OPC) Data

The OPCs deployed on the TBS systems were used to measure the larger particle size range from 0.35 µm to 37.0 µm Figure 101 shows a 3D profile of the total measured concentrations of particles larger than 0.35 µm during the November 3 and March 7 deployments.

During the November 3 TBS deployment an OPC was only located on the upwind and profiling balloon (Upwind and Downwind 1 in Figure 91). During this deployment the OPC observed some

higher concentrations associated with the plume advecting towards the east (indicated by yellow circles on left panel of Figure 101. The Downwind 1 OPC was utilized as a profiling balloon which allowed for the measurement of concentration at multiple altitudes.

As shown in Figure 101 for the March 3 deployment both the upwind and downwind concentrations during the measurement period were highly variable, with relatively high concentrations being observed at both locations.

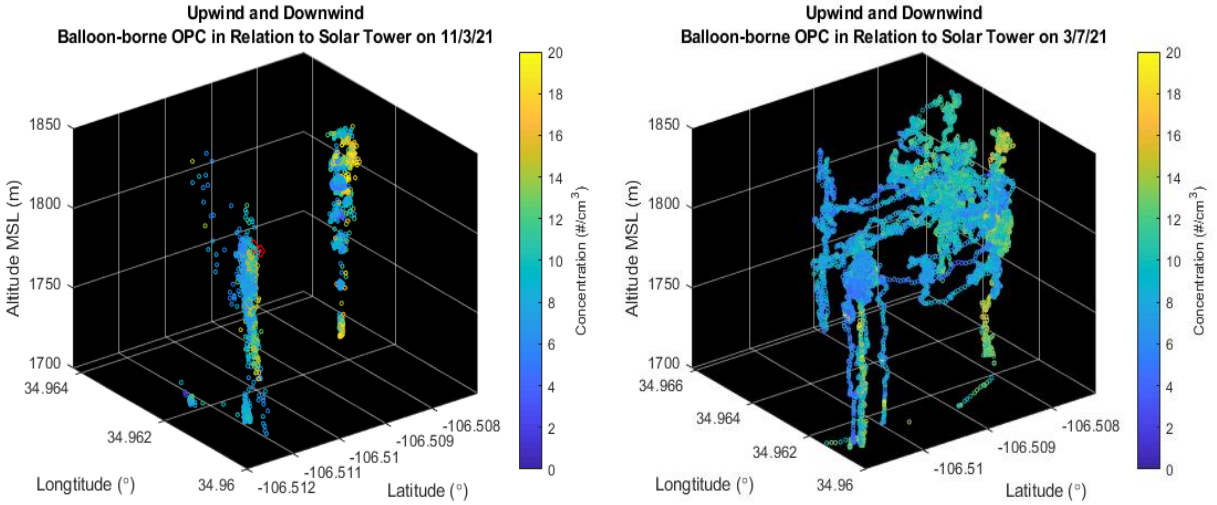

Figure 101: Upwind and Downwind OPC Concentrations on November 3rd, 2020 (Left) and March 7th, 2021 (Right).

The aerosol size distributions as measured by the OPCs onboard the Upwind and Downwind 1 TBS platforms are shown in Figure 102 for the One-Stair configured study on November 3. The data shows an increase in concentration in the smaller sized channels (< 1.0 μm) of the OPC at the downwind location compared to the upwind. This concentration increase is most evident during the period between 12:30 and 13:30.

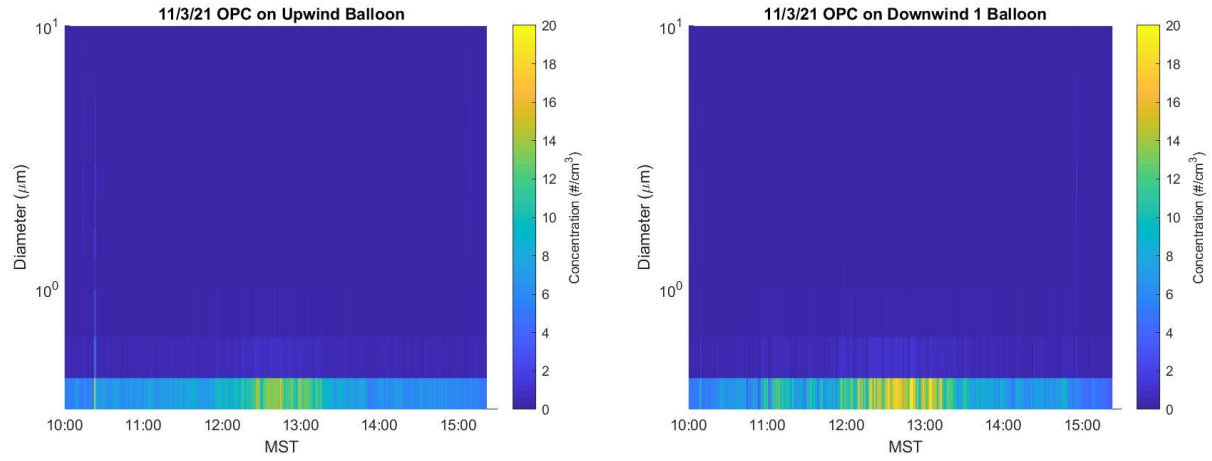

Figure 102: Aerosol size distribution evolution for balloon borne OPCs during the 11/3/21 study.

Similar aerosol size distributions are shown in Figure 103 for the March 7 study. The data collected from this day show some variability in size resolved concentration with time, however, there are no distinct differences between the upstream and downstream instruments and with less of a peak concentration observed than the November 3rd dataset.

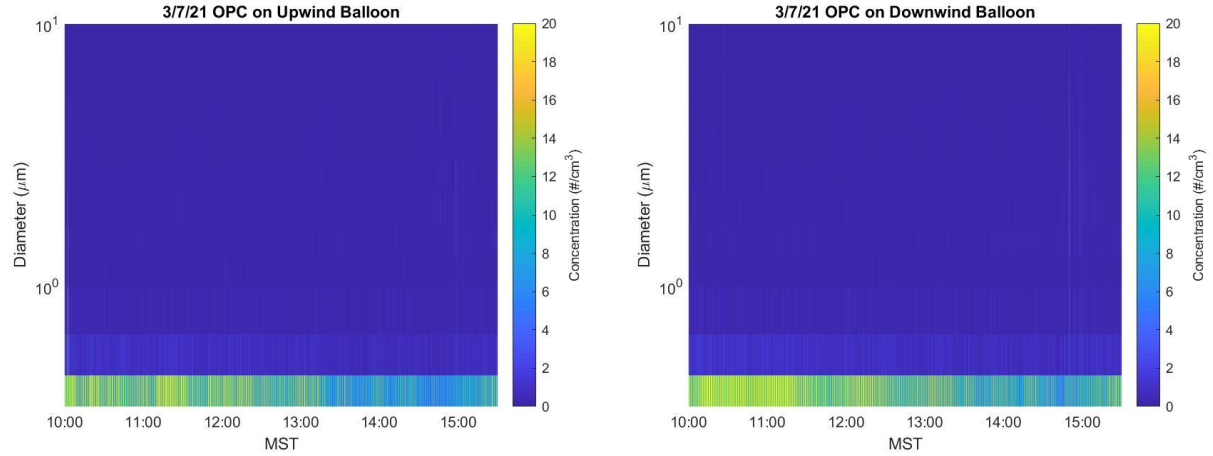

Figure 103: Aerosol size distribution evolution for balloon borne OPCs during the 3/7/21 study.

To quantify the perturbation in number concentration between the upwind and downwind OPC TBS measurements, the time resolved size dependent concentration measurements were averaged into 5 minute intervals. The average concentration for upwind, downwind and the difference between downwind and upwind was calculated and is plotted in Figure 104 for the OPC data collected on November 3 and Figure 105 for March 7. The November 3 data shows a positive perturbation (yellow line) in the concentrations measured downstream for particle sizes between 0.35 μm and 1.70 μm, indicating that additional aerosol are present at the Downwind 1 location compared to the Upwind location. The data collected on March 7, shows some perturbations for particles with diameters within the of 0.35 μm to 0.46 μm channel however, the relative difference is less pronounced, with only minimal relative difference observed at particle diameters greater than 1.0 μm.

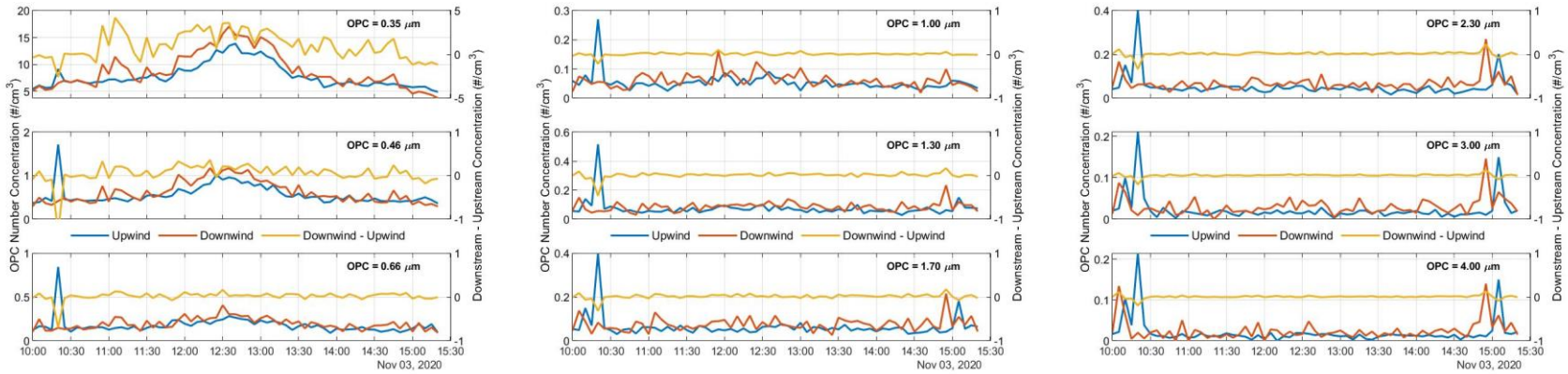

Figure 104: Size resolved aerosol concentration values and perturbations for the November 3, 2020 data.

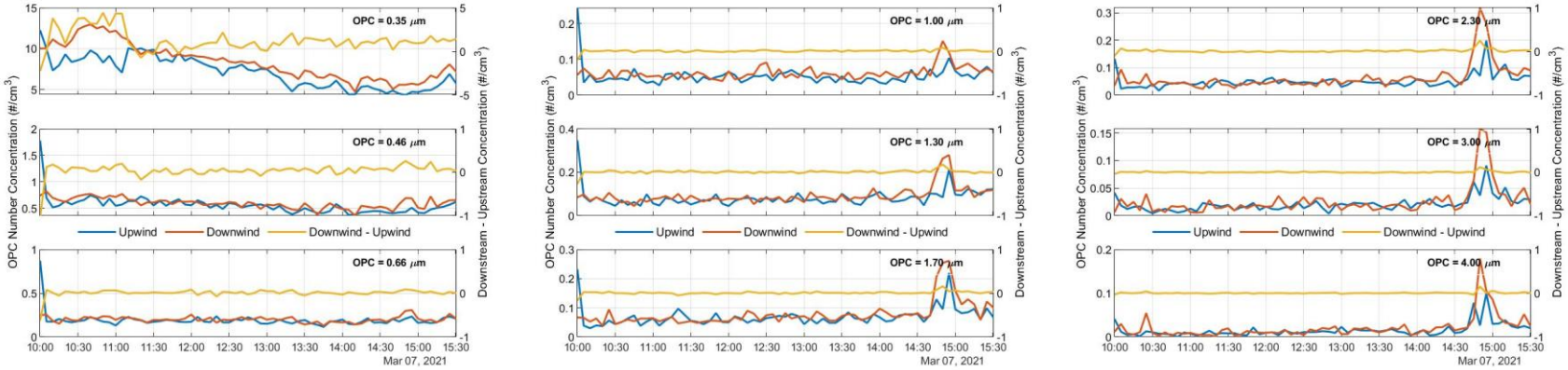

Figure 105: Size resolved aerosol concentration values and perturbations for the March 7, 2020 data.

4.2.4. POPS to OPC Comparison Data

The POPS and OPC both provide size resolved measurements of concentration. Based on the data collected during the March 7 TBS deployment. Figure 106 shows a comparison of the measured concentrations of POPS and OPC size bins (which are of comparable size) for the downwind balloon. As the figure shows there some differences in the concentrations measured in the smallest channel of the OPC (0.35 µm) and the 0.335 µm channel of the POPS, with the difference decreasing to larger sizes. The percentage difference and particle diameter threshold for each of the compared sizes can be seen in Table 9.

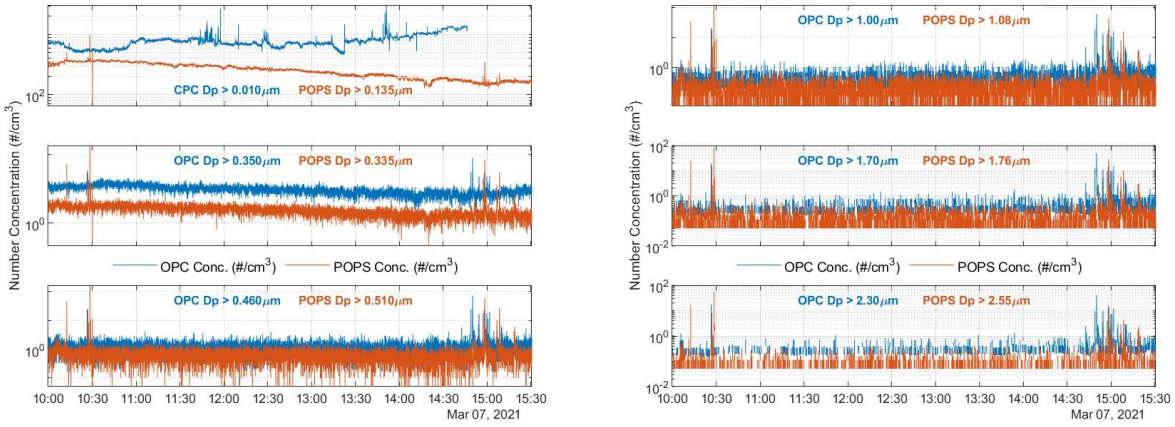

Figure 106: POPS and OPC Size Resolved Concentration Comparison.

Table 9: Instrument Concentration Comparison

OPC Diameter (µm)	POPS Diameter (µm)	Mean Percentage Difference ((OPC/POPS)-1)*100 (%)
0.35	0.335	295
0.46	0.510	62
1.00	1.08	56
1.70	1.76	60
2.30	2.55	119

The large percentage difference for the OPC at particle diameters of 0.35 µm is likely due to an instrument offset as this is the first size bin of the instrument, and uncertainty is expected to be higher.

4.2.5. Size and Time-Resolved Aerosol Collector (STAC) Data

Two time periods of interest were captured using a Size and Time-Resolved Aerosol Collector (STAC) developed by Pacific Northwest National Laboratories (PNNL) Environmental Molecular Science Laboratory (EMSL). The STAC was operated on March 7 on the downwind balloon only, and four 20-minute duration 4-stage particle impactor samples were analyzed. Stage D of the impactors collected particles with aerodynamic diameters between 0.1-0.5 µm, and stage C collected particles between 0.5-1.0 µm diameters. These two stages together collect particles over almost the entire effective particle diameter measurement range of the CPC, 0.01 - 1 µm, the lower to mid-range of the POPS and lower range of the OPC. Stage C on impactor #3 had insufficient particle

loading for chemical analysis, but carbonaceous particles dominated stage D, as shown in Figure 107.

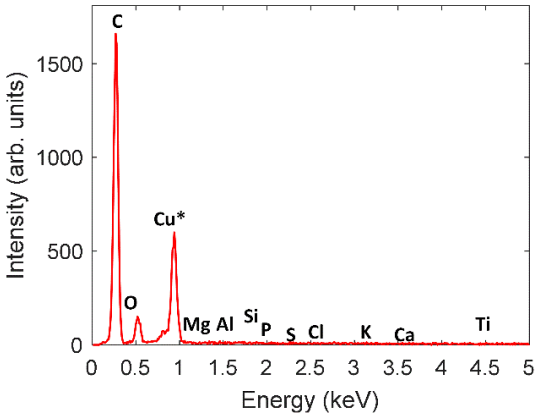

Figure 107: SEM/TEM Microscopy Image and Energy Dispersive X-Ray Spectra of Particles Collected with STAC.

Impactor #3 and impactor #6 were operated from 11:10- 11:30 and 12:10 -12:30, respectively. These time periods coincide with elevations in the CPC concentration on the downwind balloon, as shown in the red and green circles in Figure 108. Notably, impactors #4 and #5 which were operated from 11:30-11:50 and 11:50 – 12:10 had insufficient particle loading for any analysis. These periods coincide with times when relatively reduced particle concentrations were measured as depicted in Figure 108.

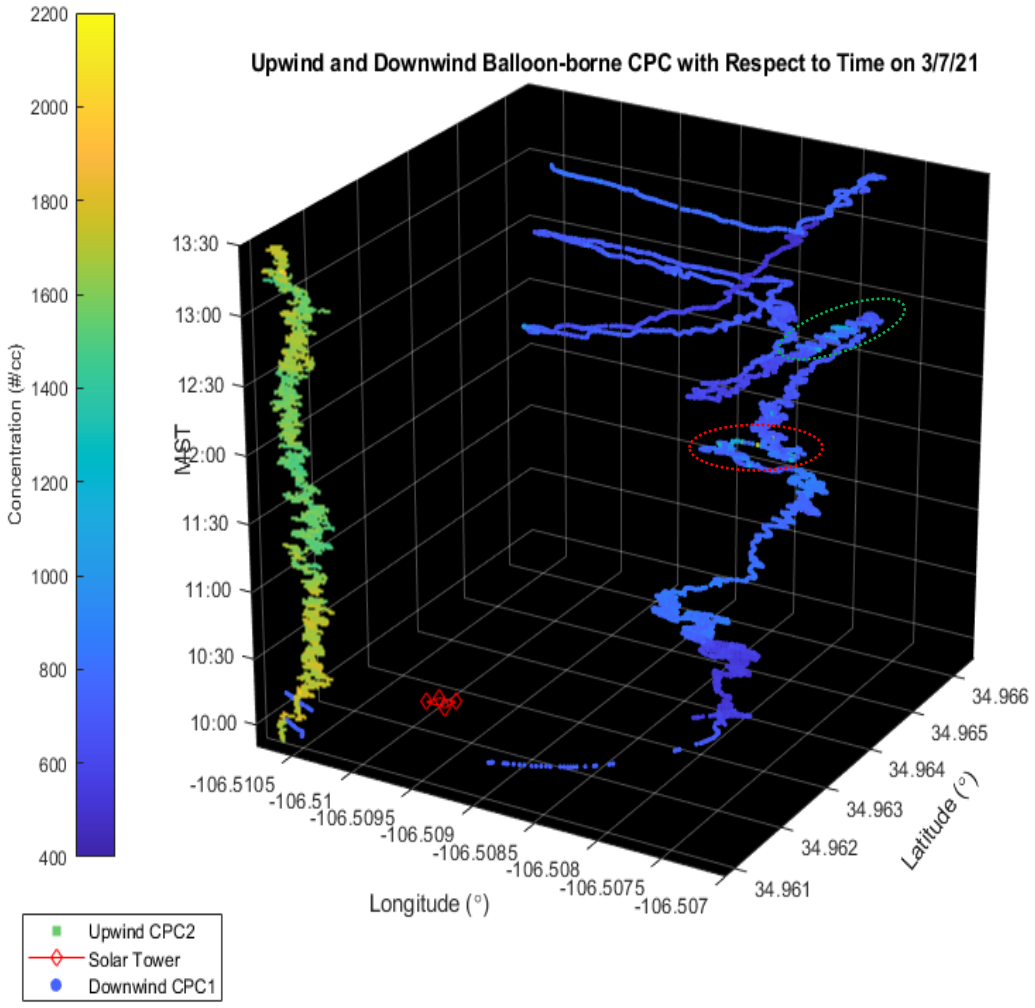

Figure 108: Temporal and Spatial CPC Data in Relation to Concentration.

Computer-Controlled Scanning Electron Microscope (CCSEM) analysis of impactor #6 stages C and D is shown below in Figure 109, and indicates that carbonaceous particles dominated in the CPC size range (0.01 – 1 μm), and that Ti-rich particles dominated in the larger particle diameter size range of 1 – 2.5 micron, which can be measured by the POPS (0.14 – 3μm measurement range) and OPC (0.35 – 2.5 μm measurement range). The 'other' particles measured in the CPC size range are visually consistent with being biological in origin. The carbonaceous particles are likely typical background atmospheric constituents, while the Ti-rich particles are consistent with the composition of CARBOHSP. In summary, the STAC CCSEM analysis indicates that the particles being measured by the CPC are not consistent with the composition of CARBOHSP, but that particles in the POPS and OPC measurement range are consistent with CARBOHSP composition. Impactor samples were also collected on November 3, but they have not yet been analyzed.

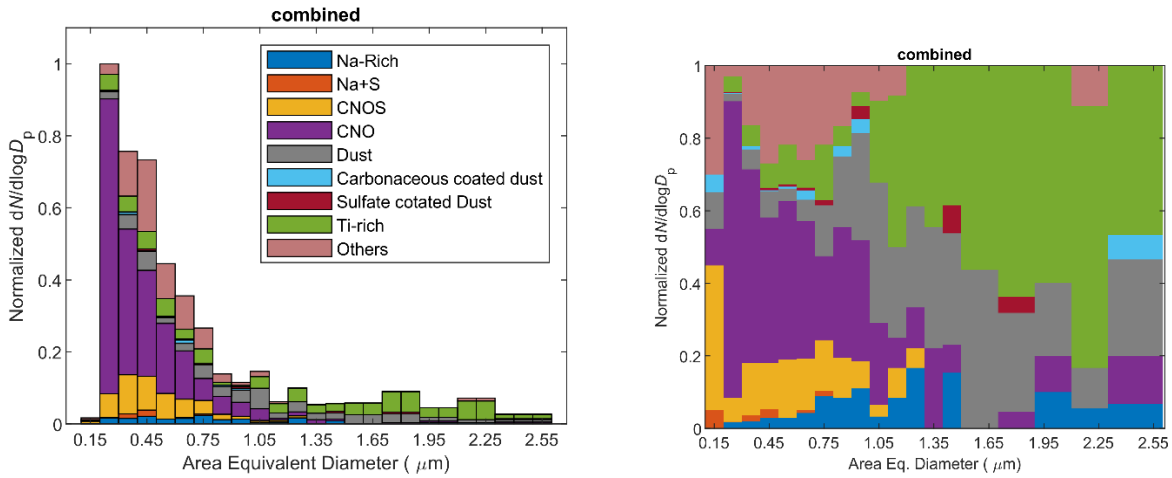

Figure 109: CCSEM chemical composition.

The STAC data indicates the presence of low concentrations of Ti rich particles within the 0.5 to 1.0 µm particle diameter range measured at the downwind balloon. These particles are most likely CARBO-HSP particles, however based on an estimation of the total mass concentration derived from the number distribution measured during the study period, there is no significant concentration increase associated with the advected plume from the solar tower aperture during this operational configuration. With the measured concentrations from upwind and downwind instruments being within expected measurement uncertainty.

4.3. Wind Sector Analysis

A wind sector analysis was conducted for both TBS flights to filter out wind conditions not conducive to transport of aerosol to the instruments. This type of analysis filters out data based on the preliminary wind direction and speed as measured by the local anemometers located on the TBS or solar tower. Wind sectors of interest were determined by identifying the direction of the monitor placements (east and west) of the aperture and the associated wind direction which would advect a plume to these locations. Figure 110 depicts the wind sectors of interest for both November 3 and March 7. Based on the location of the TBS or the location of the high POPS concentrations the data was filtered to provide wind sectors of the directions shown in Table 10. The total concentration data from the wind sector analysis were then filtered to identify trends.

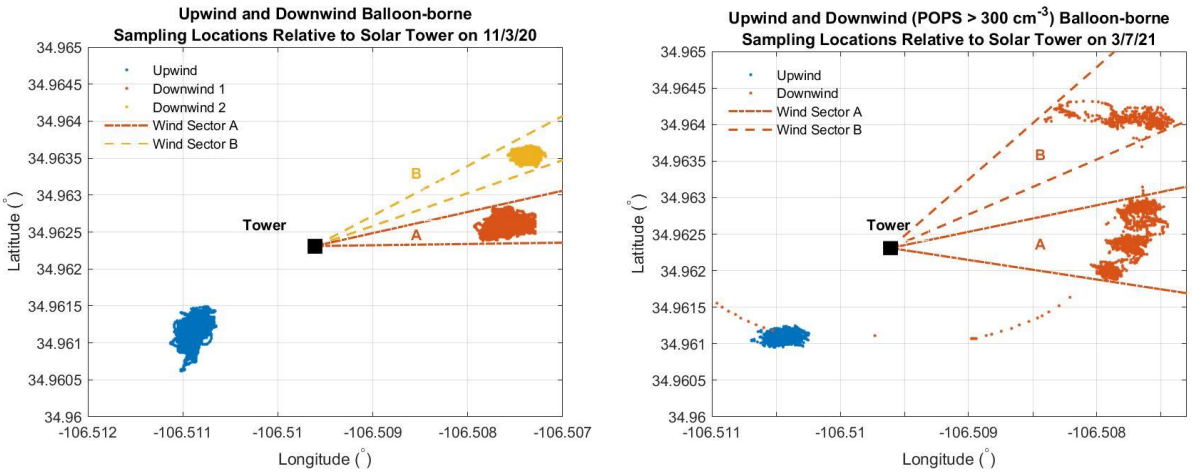

Figure 110: Wind Sector Analysis for November 3 and March 7.

Table 10: Wind sector analysis from November 3rd, 2020 and March 7th, 2021.

Date	Wind Sector	Balloon	Wind Sector (blowing from)
11/3/20	A	Downwind 1	254° - 269°
11/3/20	B	Downwind 2	236° - 246°
03/7/21	A	Downwind	250° - 285°
03/7/21	B	Downwind	213° - 233°

An example of a wind sector analysis for the March 7 data can be seen in Figure 111 for both wind sector A (left panel) and B (right panel). As the data shows the POPS and OPC concentrations shows a slow decrease over time during the wind directions of interest, however, there are a number of discrete spikes in the CPC data during the wind directions of interest.

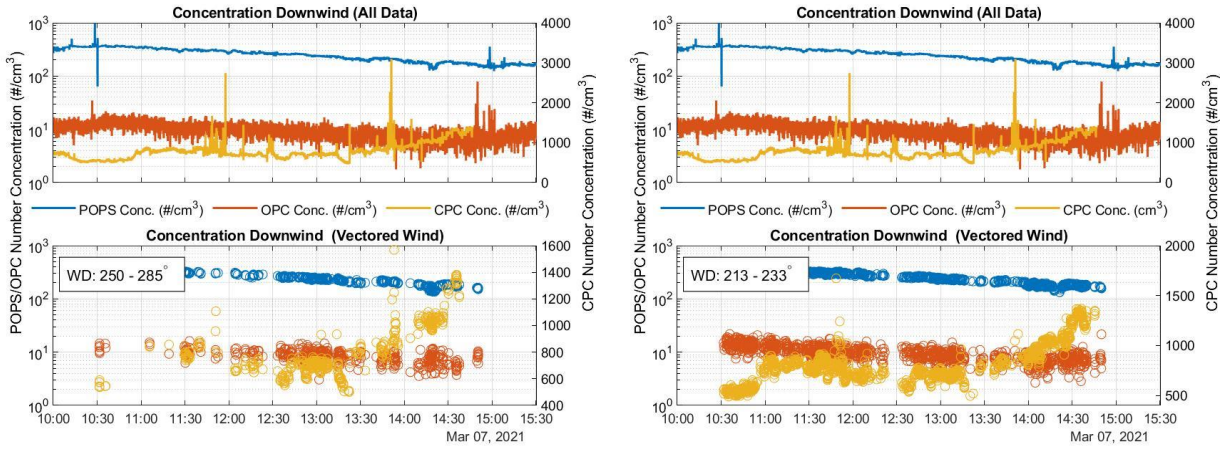

Figure 111: Resulting concentrations for the wind sector analysis applied to March 7 data.

4.4. Occupational and Environmental Impact

To assess the occupational and environmental impacts of emissions from the solar tower receiver an assessment of the mass concentration contribution was completed. The near-field data is comparable

to OSHA Occupational Permissible Exposure Limits (PEL) and the far-field is more akin to EPA National Ambient Air Quality Standards. (NAAQS).

4.4.1. NAAQS Comparison

Using the perturbations in number concentration, (subtracting the upwind concentrations from the downwind concentrations) on November 3rd and March 7th, seen in Figure 104 and Figure 105 for the OPC data, and assuming the particle density (3,600 kg/m^3) a size resolved mass distribution perturbation over the sampling periods can be calculated. The size resolved mass concentration is calculated by finding the midpoint diameter (D_p) of the OPC channels of interest (0.35 μm to 10 μm), and the associated average mass of a particle at that size (m_p). The average particle mass is then multiplied by the perturbation in the number concentration over time (N_p):

$$DiameterMidpoint = \left[\overline{D_p}\right]_{10\mu m}^{0.35\mu m} = \frac{Dp_{upper} - Dp_{lower}}{2}$$

$$AverageParticleMass = \left[\overline{m_p}\right]_{10\mu m}^{0.35\mu m} = \frac{4}{3}\pi\rho\left(\frac{\overline{D_p}}{2}\right)^3$$

$$MassConcentrationper[M_P]_{10\mu m}^{0.35\mu m} = \overline{m_p} \times N_p$$

Once the mass concentration per size channel of the OPC are established, a concentration for $PM_{2.5}$ and PM_{10} as a function of time can be calculated with the following methods:

$$PM_{2.5} = \sum_{i=0.35\mu m}^{2.5\mu m} \left[M_p(t)\right]_i$$

$$PM_{10} = \sum_{i=0.35\mu m}^{10\mu m} \left[M_p(t)\right]_i$$

Figure 112 and Figure 113 are the mass concentration values for the number concentration perturbation (shown in Figure 104 and Figure 105) for the November 3 and March 7 far-field studies respectively. As the figures show there are higher mass concentrations measured during the November 3 measurements compared to March 7 study. Each panel in the figures lists the total mass concentration per size channel of the OPC, based on the midpoint diameter for particle sizes ranging from 0.35 μm to 10 μm.

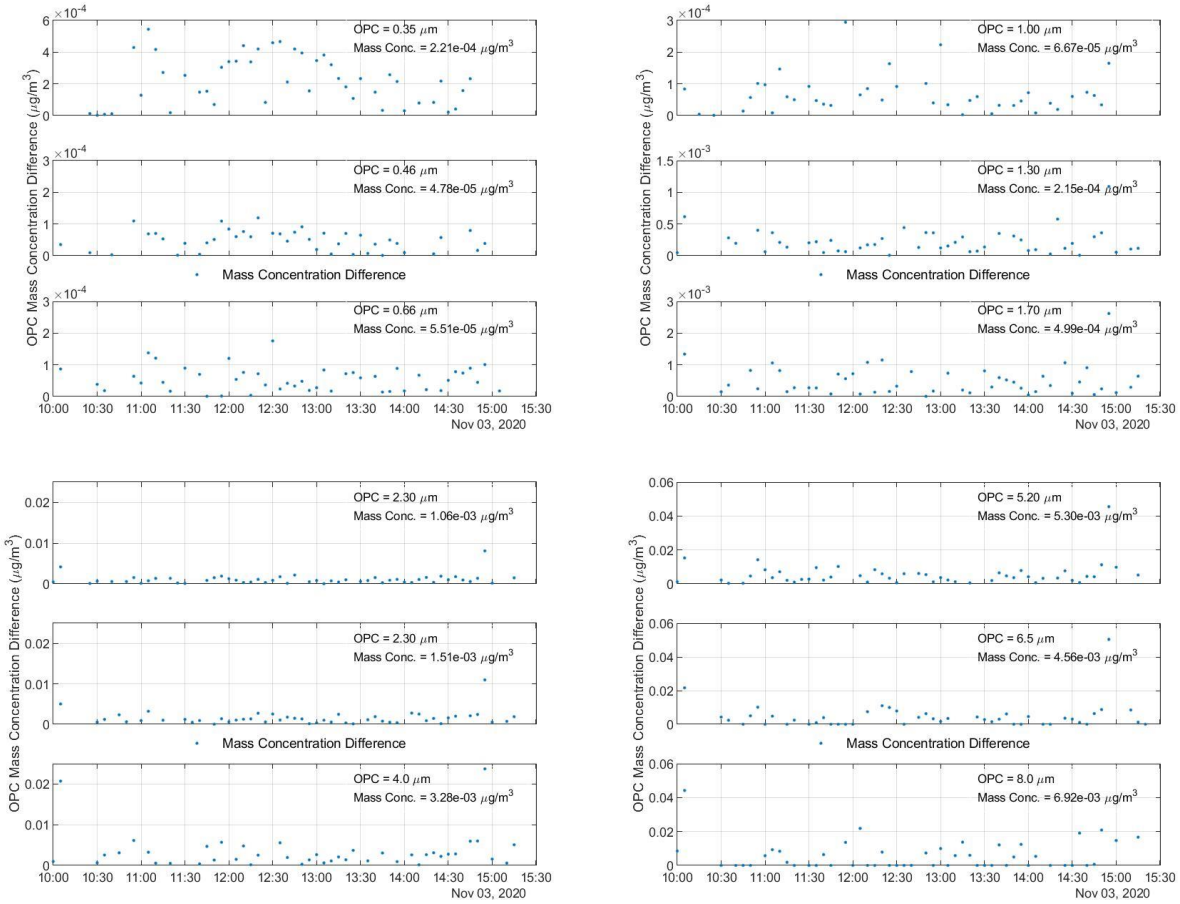

Figure 112: Mass concentration differences based on the number distribution shown in Figure 104.

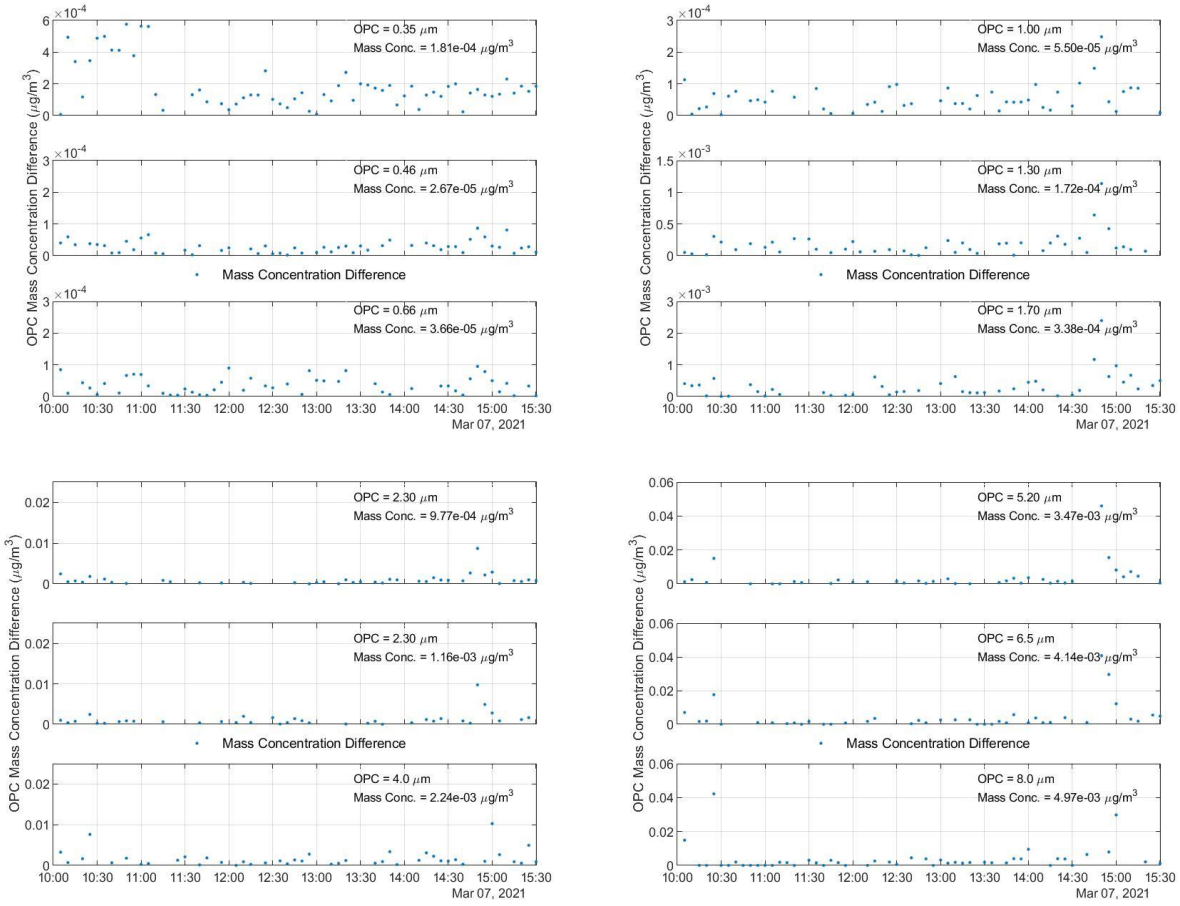

Figure 113: Mass concentration differences based on the number distribution shown in Figure 105.

A summary of the $PM_{2.5}$ and PM_{10} average concentrations over the sampling period is shown in Table 11. The measured concentrations were collected over 5.5 hours per study and it is assumed that these concentrations can be conservatively applied to the 24-hr averaging period, with caveats discussed below. Applying the $PM_{2.5}$ and PM_{10} concentration values estimated from the OPC measurements, the aperture configuration appears to have an impact on the total concentration generated, with an order of magnitude increase in concentration measured for the One-Stair configuration for $PM_{2.5}$. The PM_{10} values are of similar magnitude with only a slight increase on overall average concentration for the One-Stair configuration. These values are well below the Significant Impact Levels (SIL) utilized in regulatory air dispersion models.

Table 11: Summary table of far-field concentration data compared to NAAQS.

Date	Aperture Configuration	(5.5 hr) OPC Mass Contribution (μg/m³)		24-hr NAAQS Standard (μg/m³)		Percentage of NAAQS	
		$PM_{2.5}$	PM_{10}	$PM_{2.5}$	PM_{10}	$PM_{2.5}$	PM_{10}
Nov 3, 2020	One-Stair	0.022	0.024	35	150	0.06 %	0.016 %
Mar 7, 2021	Free-Fall	0.0018	0.018	35	150	0.005 %	0.012 %

The direct comparison of measured concentrations to the NAAQS standards cannot be used for regulatory analysis or decisions as the measurements shown here did not use approved measurement methods as discussed in 40 CFR 50 Appendix L. Additionally, the data was not collected over a full 24-hour period and therefore was extrapolated from the average conditions seen over the sampling period to generate a conservative estimate. As the NAAQS are designed to protect the ambient air quality outside of an emissions source domain at ground level, the use of measurements from the tethered balloon platform are preferential as the emissions from the source will be naturally diluted away from the source through air dispersion. Additionally, a facility such as the solar tower would only be operational during daylight hours and as such would not have expected emissions during night, which would also reduce the overall 24-hr design values.

4.4.2. PEL Comparison

The PEL is a regulatory limit in the United States for exposure of an employee to a chemical substance. The applicable PEL for Particulate Matter (PM) is an 8-hour Time Weighted Average (TWA) of 15 mg/m^3 for Total Dust and 5 mg/m^3 for the Respirable Fraction. The measurements most applicable to compare to this standard are from the near-field data as this is the higher concentration values for an individual to be exposed to near the source. Two methods were used to estimate concentrations to compare to the PEL.

The first method was an overly conservative estimate of the airborne concentration based on the worst-case concentration seen in all the collected data. This was done using the September 3 near-field dataset to compare to the PEL using the following method. The worst-case maximum concentration was observed on the east side of the solar receiver at 14:05 by the OPC. The data collected during this event was averaged over a ten-minute interval to provide a worst-case number concentration. The size distribution of particles at the time of this event was used to provide particle mass concentration, using the CARBO HSP density. The mass concentration was then assumed to be present for the full 8-hour period that the TWA is calculated over. The result of this calculation show a concentration of 0.45 mg/m^3 and 0.61 mg/m^3 which is 9.0 % and 4.1% of the respirable and total dust fraction PEL respectively.

A more representative method was also used which utilized data from the OPCs for all the near-field data collected. This method uses the same methodology as discussed in the equations above and assumes the average concentration occurs over the 8-hour period. The results are shown in Table 12 and are all negligible compared to the PEL standard of 15 mg/m^3 and 5 mg/m^3 for Total Dust and Respirable Fraction respectively.

Table 12: Estimated PEL Values based on OPC measured data.

Date	Location	Estimated 8-hr PEL (mg/m^3)
08/17/20	East	1.34e-5
08/17/20	West	9.67e-5
08/18/20	East	2.23e-5
08/18/20	West	5.55e-5
09/03/20	East	4.60e-5
09/03/20	West	4.43e-5
09/04/20	East	5.89e-5
09/04/20	West	2.89e-5
11/03/20	East	2.15e-5
03/07/21	East	7.01e-7
03/07/21	West	2.42e-5

5. MODELING

Modeling was performed by Ho and Pattyn [13] to evaluate particle emissions and resulting concentrations relative to regulatory standards. Two models were developed to simulate particle plume concentrations from the particle receiver. A detailed computational fluid dynamics (CFD) model was developed to simulate both large and small particle emissions and to evaluate plume shape as a function of wind speed. An EPA-recommended plume modeling software (AERMOD) was also used to simulate and evaluate averaged plume concentrations over longer periods of time for comparison to EPA standards. Benchmarking of the two models was performed.

5.1. Computational Fluid Dynamics Modeling

A computational fluid dynamics (CFD) model of the emission and dispersion of particles from Sandia's 1 MW_t particle receiver was developed using Solidworks Flow Simulation. The particle trajectories and plume concentration were modeled as a function of wind speed, wind direction, and particle emission rate. Two particle sizes were investigated: 350 microns (which is the initial, as-received nominal size for 40-70 mesh CARBO HSP ceramic particles) and ≤ 10 microns (for comparison to inhalation and pollution standards for particle fines that may be generated). Particle sizes on the order of 10 microns or less were found to be essentially buoyant and followed the flow lines of the wind velocity. Therefore, for comparison to EPA National Ambient Air Quality Standards (NAAQS) for particulate matter (PM) 2.5 and PM 10 (i.e., particles equal to or less than 2.5 and 10 microns, respectively), small particles were simulated as a gas having the same molecular weight (0.11 kg/mol), specific heat (1200 J/kg-K), and thermal conductivity (2 W/m-K) as the CARBO HSP particles. The dynamic viscosity was assumed to be the same as air. The aperture of the falling particle receiver was assumed to emit particle fines (<10 microns) at a rate estimated to be ~1e-5% of the particle mass flow rate for small particle generation, which was estimated from previous tests [14]. For a particle mass flow rate of 5 kg/s, which provides 1 MW_t of power with a ΔT of 200 °C and a specific heat of 1200 J/kg-K, the emission rate was calculated to be 5e-7 kg/s. The mass fraction of the particle emissions was assumed to be one so that only particles would be generated (and not air) from the aperture, which was located on top of the 61 m (200 ft) tall tower. The temperature of the particle gas emitted from the aperture was assumed to be 700 °C, which is approximately the average of the design temperatures of the particles entering and exiting the receiver.

5.2. AERMOD (EPA Particle Dispersion Modeling Software)

Additional modeling was performed using the EPA-recommended modeling software, the American Meteorological Society / EPA Regulatory Model (AERMOD), for a commercial-scale (100 MW_e) particle receiver system. AERMOD was designed to support the EPA regulatory programs and, as such, is considered the most appropriate model to perform air dispersion modeling analysis for continuous or intermittent emission sources.

AERMOD is a steady-state plume modeling software that is designed to model dispersion and deposition of six common air pollutants, designated as "criteria air pollutants" by the EPA; these pollutants are ozone (O_3), carbon monoxide (CO), lead (Pb), sulfur dioxide (SO_2), nitrogen dioxide (NO_2), and particulate matter (PM). Particulates are the only pollutant emitted from the tower, so equations in AERMOD not pertaining to particulate dispersion and deposition were omitted in the analyses. The Appendix contains a description of the particle deposition model in AEROMOD. A description of all the equations governing AERMOD, as well as program development documents,

can be found in the "Model Supporting Documents" section on the EPA's Air Quality Dispersion Modeling site.[1]

AERMOD requires specification of source parameters (size, pollutants emitted, emission temperature, emission rates, and aperture size) which are then analyzed in hourly increments using meteorological data provided by the user. These hourly increments are then averaged over user-requested time periods and can then be used in 3D visualization software to create a volumetric or isometric surface of the particle concentrations representative of the averaged time periods. In addition to local meteorological data, AERMOD also considers the planetary atmospheric boundary layer(s) when calculating pollutant dispersion.

The mass fractions of the particles emitted in the two size ranges of PM 2.5 and PM 10 are assumed to be equal (50% each) for the AERMOD simulations. The emission source for a 100 MW_e falling-particle receiver is assumed to be a north-facing circular aperture (22.6 m in diameter; equivalent to a 20 m x 20 m square aperture) located 285 m above the ground. Particles with a density of 3,300 kg/m^3 are emitted from the aperture at a temperature of 700 °C with a mass flow rate of 2.8e-4 kg/s (~1 kg/hour). The mass flow rate of the emitted particles is based on an assumed flow rate of particles through the receiver of 2000 kg/s (to achieve 100 MW_e). Previous testing has estimated that the small particle generation rate (<10 microns in size) is 1.4e-5% of the total particle flow rate through the receiver.

The tower is assumed to be in a geologically flat area located near the NSTTF. The closest public receptor for evaluating the EPA standards was assumed to be located 1,500 m away (at the perimeter or "fence line" of the plant as required by EPA standards). For comparison, the heliostat field at the 110 MW_e molten-salt CSP plant (with 10 hours of storage) has a heliostat field that extends approximately 1,600 m from the tower. Peak ground-level particulate concentrations at various radial distances in the vicinity of the tower were also investigated to determine potential hazards to on-site workers.

Meteorological data was taken from the NSTTF site. This data reflected the hourly conditions of the site over a five-year window spanning from 2013 to 2017. This dataset was generated using data from the sitewide meteorological tower network at Sandia National Laboratories. The regional climate is dry and sunny, with an annual average precipitation of 20 cm (8 in) and an average of nearly 300 sunny days annually.

For this model a three-dimensional cartesian receptor grid was created centered around the tower. The grid was 3,000-meters north-south by 3,000-meters east-west by 500-meters vertically. Receptors were spaced every 100-meters circumferentially around the tower (at a radial distance of 1,500 m) and every 25-meters vertically at the nearest Cartesian coordinate. The grid was populated with over 20,000 discrete receptors at which concentrations were directly calculated.

Separate models were created to analyze the behavior of both the PM-2.5 emissions and the PM-10 emissions individually, then a final model was created for the purposes of analyzing the combined emissions simultaneously. This final model accounts for the varying particle sizes in the plume and their interactions and yields the concentrations for the total suspended particulates (TSP). The TSP may be different than the sum of the individually calculated PM-2.5 and PM-10 results due to particulate interactions.

Finally, a simulation was performed to calculate the maximum allowable particle emission rate that could be sustained before the concentrations were longer in compliance with the most stringent of

[1] https://www.epa.gov/scram/air-quality-dispersion-modeling-preferred-and-recommended-models#aermod

federal and state standards. Between federal (NAAQS) and state (NMAAQS) standards the most stringent requirements necessitate that a source not cause the 24-hour average ground-level pollutant concentrations to exceed the following thresholds 35 $\mu g/m^3$ for PM 2.5 and 150 $\mu g/m^3$ for PM 10. Additionally, these standards necessitate that an annual average of ground-level PM 2.5 not exceed 12 $\mu g/m^3$.[2,3] The maximum particle emissions rate was determined by running several iterations of the initial models until ground-based receptors returned a violation of any of the air quality standards.

5.3. Modeling Results

5.3.1. Benchmarking (CFD vs. AERMOD)

A sample of the results of the CFD modeling of particle emissions from the existing particle receiver at the NSTTF are shown in Figure 114. For a west wind of 2 m/s (~5 mph), the steady-state results using the input parameters described earlier yield a plume that extends horizontally downstream from the aperture on top of the tower. The plume exhibits a slightly non-uniform shape due to the impact of the geometry of the tower and particle receiver on the wind, which creates a swirling pattern that extends slightly upward downstream of the tower. The extent of the plume with a maximum particle mass fraction of 1e-9 kg/kg (1 ppb) extends less than 100 m from the aperture. The maximum particle mass fraction of 1e-8 kg/kg (10 ppb), which corresponds to the EPA annual average concentration limit for PM 2.5 of 12 $\mu g/m^3$ under ambient air conditions, extends only ~20 m from the aperture. This indicates that the likelihood of exceeding the EPA metrics for a receptor located outside of the boundaries of the CSP plant are very low.

Different wind speeds were simulated in the CFD model, and results showed that higher wind speeds diluted the particle concentrations. For example, for a 10 m/s west wind speed, the maximum particle concentration of 1e-9 kg/kg (1 ppb) extended only about 30 m downstream of the aperture, less than half the distance with a 2 m/s wind speed. In addition, different particle emission rates were simulated. Higher particle emissions from the aperture led to larger and more extensive plumes, which was expected. Finally, different wind directions were simulated, but the impact on the particle plume shape and concentrations was small relative to the impact from wind speed and particle emission rates.

[2] U.S. EPA NAAQS Table: https://www.epa.gov/criteria-air-pollutants/naaqs-table
[3] Albuquerque Bernalillo County: http://164.64.110.134/parts/title20/20.011.0008.html

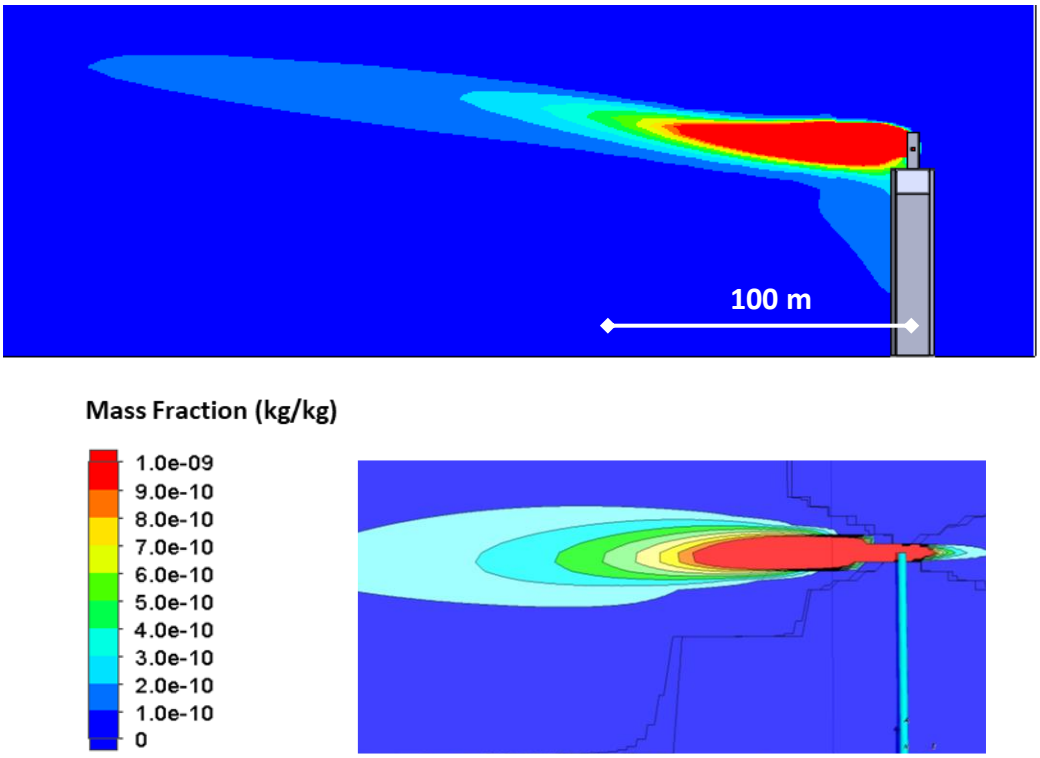

Figure 114. Simulated small particle (<10 μm) mass fractions in air with a west wind speed of 2 m/s using CFD (top) and AERMOD (bottom).

Figure 114 also shows the simulated particle concentrations from an equivalent AERMOD model of particle emissions from a particle receiver at the NSTTF. The same boundary conditions and properties were used in the AERMOD model for benchmarking purposes. Results show that the AERMOD model yields similar results to the CFD model. The particle plume extends horizontally downstream from the aperture with a 2 m/s west wind. The AERMOD plume is more symmetric about the horizontal plane because the impact of the tower and receiver geometry are not included in the AERMOD model. Also, the assumption of buoyant particles (for sizes < 10 μm) in the CFD model appears to be supported by the AERMOD dispersion model. A discrepancy between the CFD and AERMOD results was observed at different wind speeds. At higher wind speeds, AERMOD yielded larger particle plumes, which was counter to the dilution effect observed in the CFD results. At higher wind speeds, the extent of a plume with prescribed isopleths should be smaller if all other factors and boundary conditions are the same. This issue was raised with the developers of AERMOD, and investigations are ongoing.

5.3.2. Large Particle Emissions

Figure 115 shows the results of a CFD particle simulation in which 350 micron particles were emitted from the 1 MW_t particle receiver aperture ~70 m above ground at the NSTTF at a rate of 0.003 kg/s (the maximum rate estimated in past on-sun tests [2]). The simulation shows that these larger particles fall downward under the force of gravity and are not carried significantly in the presence of a relatively low wind speed of 2 m/s (~5 mph). This was further confirmed by analyzing the terminal velocity of these 350 μm particles. Assuming a spherical shape, the terminal

velocity of individual particles was found to be ~2 m/s. This means that the average suspended time of these particles would be ~35 seconds from the receiver to ground level (and less than 3 minutes for a 300-m tall tower in a commercial-scale system), further confirming that they would not be carried a significant distance given normal terrestrial wind conditions.

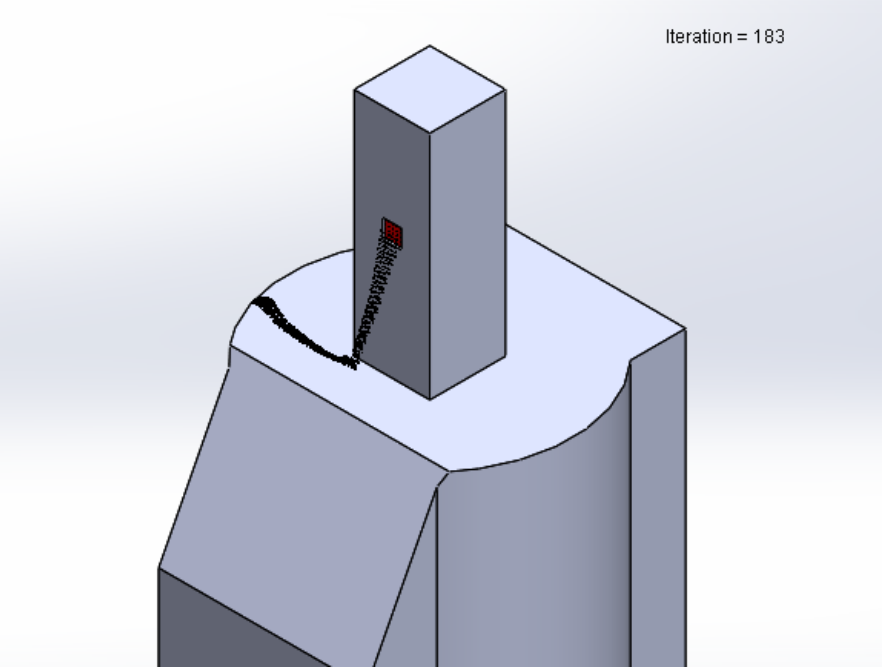

Figure 115. CFD simulation of 350 μm particles emitted from receiver aperture at the NSTTF (0.003 kg/s, 2 m/s west wind).

5.3.3. Small Particle Emissions

Figure 114 showed results of simulated small particle emissions from the 1 MW_t particle receiver at the NSTTF for both the CFD and AERMOD models at fixed wind speeds for purposes of benchmarking and comparison. In this section, results from the AERMOD model of a commercial-scale 100 MW_e ~300-m tall tower are presented using time-varying meteorological data. AERMOD reports time-averaged particle concentrations (e.g., 24 hours or annually) for comparison to the metrics prescribed in the NAAQS. Figure **116** shows the 24-hour maximum PM-10 concentrations. The results reflect the maximum possible extent to which particulate concentrations may extend on any given day. The highlighted bubble in the center (red), indicates the maximum permissible ground level 24-hr average concentration of PM 2.5 (35 $\mu g/m^3$). This region of elevated particle concentrations barely extends vertically and horizontally beyond the aperture before it dissipates and does not risk reaching ground level.

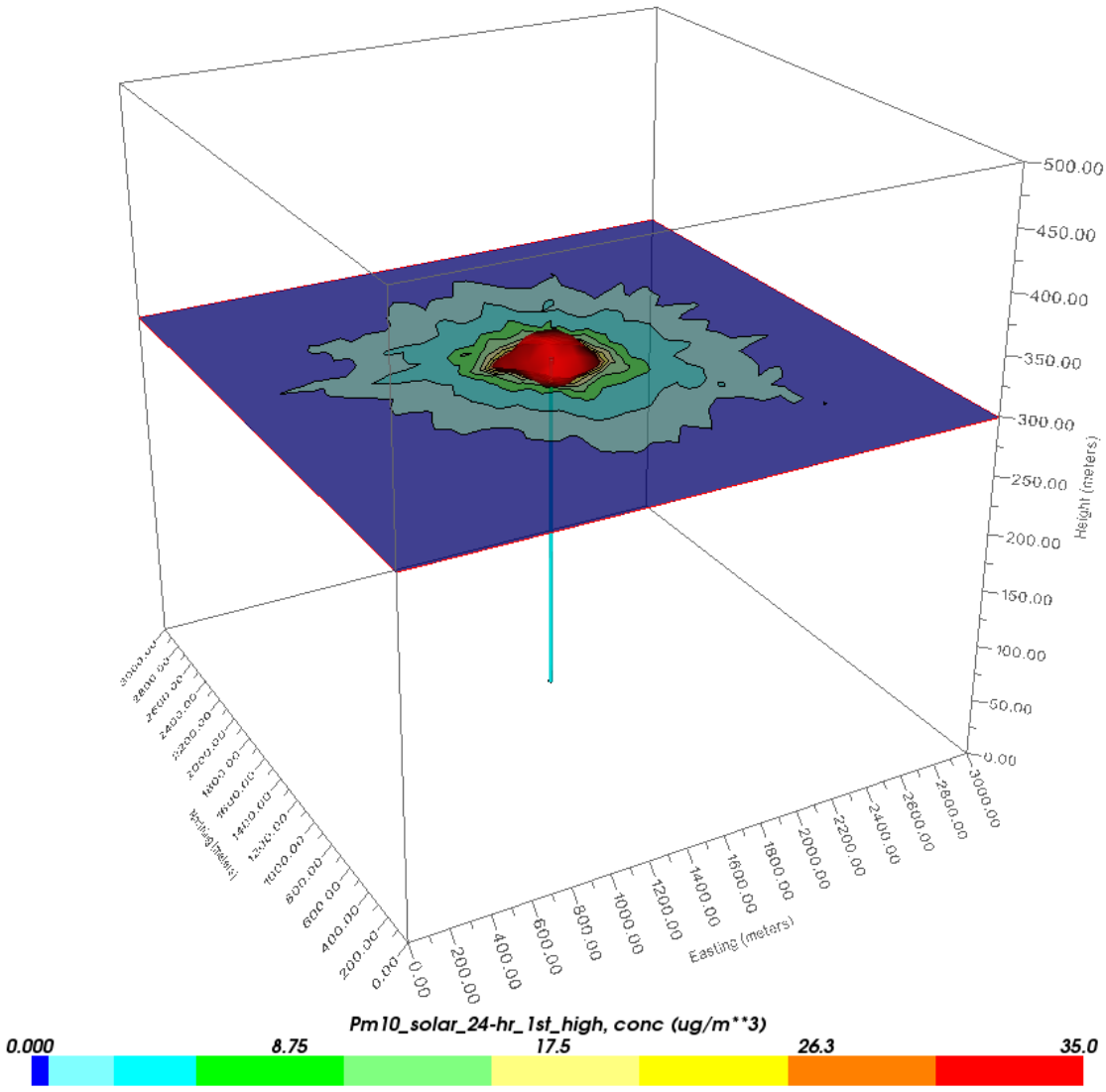

Figure 116**. 24-hour maximum emission results from initial AERMOD modeling.**

Results from the AERMOD model are summarized in Table **13**, which presents the annual and 24-hour averaged particle concentrations of PM-2.5, PM-10, and total suspended particulates at the ground (for comparison to standards) and plume (peak). The results show that the simulated ground-level particle concentrations are all significantly less than the EPA and NM standards.

Since these initial simulations resulted in no violation of standards, additional modeling was performed to determine the particle emission rate that would violate the ambient air standards. The particle emission rate was continually increased until the ground-based particle concentrations approached the ambient air quality standards. The results of this secondary run are summarized in Table 14. Results showed that the particle emission rate could be increased by a factor of 400 before the ground-based particle concentrations began to approach the standards. This emission rate of ~0.11 kg/s or ~400 kg/hour corresponds to 5e-3% of the total particle mass flow rate through the receiver. It is interesting to note that Albrecht et al. estimated that a total particle loss rate of 1e-3%

(including both large and small particles) was the maximum that could be sustained before a significant impact on the levelized cost of electricity was observed.

Table 13. Simulated small-particle plume concentration for a 100 MW_e plant using AERMOD with estimated emission rates from tests [14].

Modeled Parameter			Model Results ($\mu g/m^3$)	NAAQS and NMAAQS ($\mu g/m^3$)	Result
PM-2.5	Annual	Ground	0.006	12	PASS
		Plume	4.479		---
	24-hr	Ground	0.034	35	PASS
		Plume	117.2		---
PM-10	Annual	Ground	0.006	150	PASS
		Plume	4.544		---
	24-hr	Ground	0.043	150	PASS
		Plume	145.8		---
Total	Annual	Ground	0.012	12	PASS
		Plume	9.024		---
	24-hr	Ground	0.160	35	PASS
		Plume	290.4		---

Table 14. Simulated small-particle plume concentrations for a 100 MW_e plant using AERMOD with maximum emission rates.

Modeled Parameter			Model Results ($\mu g/m^3$)	NMAAQS ($\mu g/m^3$)	Result
PM-2.5	Annual	Ground	2.400	12	PASS
		Plume	1,792		---
	24-hr	Ground	13.50	35	PASS
		Plume	46,896		---
PM-10	Annual	Ground	2.431	150	PASS
		Plume	1818		---
	24-hr	Ground	17.20	150	PASS
		Plume	58,334		---
Total	Annual	Ground	4.831	12	PASS
		Plume	3,609		---
	24-hr	Ground	34.10	35	PASS
		Plume	116,118		---

6. APPLICATION TO COMMERCIAL CSP PLANTS

The on-sun tests perform at the NSTTF required us to place the Nikon and IR cameras at a distance of 5 meters away from the aperture as mentioned on the previous section. The horizontal (H) and vertical (V) distances of the field of view can be calculated using the relationships of eq. 6.1 and eq 6.2, where L is the distance from the target to the camera and $HFOV$ and $VFOV$ are the horizontal and vertical angular fields of view. It is important to note that the configurations for both cameras will be applicable for the FPR at Sandia.

$$H[mm] = 2xL[mm]xtan\left(\frac{HFOV[°]}{2}\right) \tag{6.1}$$

$$V[mm] = 2xL[mm]xtan\left(\frac{VFOV[°]}{2}\right) \tag{6.2}$$

As mentioned before, ImageIR8300 has a resolution of 640x512 pixels and placing the camera 5 meters away from the target yields a pixel size of 0.75-1.5 mm based on the lens used, see Table 15. Although the pixel size is larger than the nominal particle diameter (0.33 mm), the opacity that a single particle generates is higher than the critical opacity 0.12%. The critical opacity is the minimum opacity required to yield a pixel temperature above the temperature resolution of ±1°C, and it is obtained by setting the pixel temperature to 1°C in equation 2 along with particle temperature of 700°C and background sky temperature of -10°C.

Table 15. IR camera dependence on lens chosen for UNM's test rig.

Using a 50 mm lens (FOV: 11°x8.8°)	Using a 100 mm lens (FOV: 5.5°x4.4°)
$H = 2x5000xtan(5.5°) = 960mm$ $V = 2x5000xtan(4.4°) = 768mm$ $PS = \frac{960mm}{640px} = 1.5\frac{mm}{px}$ $\omega = \frac{\pi x140^2}{1500^2} = 2.74\%$	$H = 2x5000xtan(2.75°) = 480mm$ $V = 2x5000xtan(2.2°) = 384mm$ $PS = \frac{480mm}{640px} = 0.75\frac{mm}{px}$ $\omega = \frac{\pi x140^2}{750^2} = 10.95\%$

$$\epsilon_{px}T_{px}^4 = (1-\omega_p)\epsilon_B T_B^4 + \omega_p \epsilon_p T_p^4 \tag{6.3}$$

On the other hand, for the Nikon camera, with a 6000x4000 resolution, it is required to account for the variability due to the lens and focal length as observed on the graph in Figure 117. The settings used in our setup are described in Table 16. These settings are calculated using the curve fitted values from Figure 117 for simplicity.

Table 16. Field of view of the Nikon camera used at UNM's test rig.

Using a 250 mm focal lens
$H = \frac{23.343x5000mm}{250m} = 466.9mm$

$$PS = \frac{466.9mm}{6000px} = 77.8\frac{\mu m}{px}$$

$$V = PSx4000px = 311.2mm$$

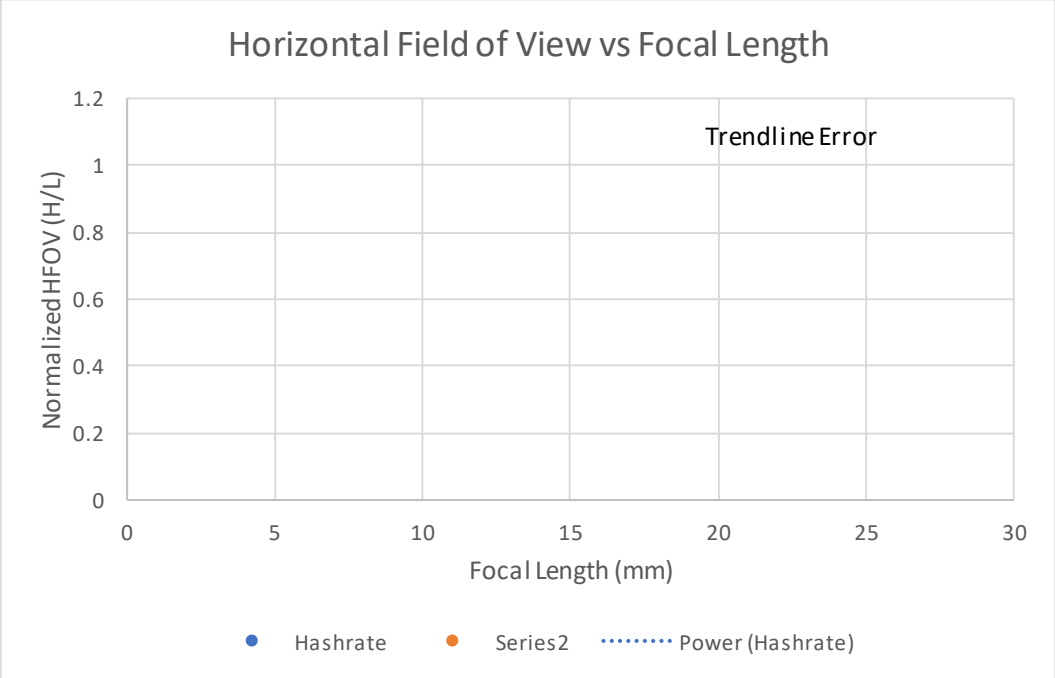

Figure 117. Variation of normalized FOV with respect to the focal length.

100 MWth Falling Particle Receiver

Using the estimated dimensions of a 100 MWth FPR configuration, we can propose suitable configurations for the cameras considering the aperture size of the cavity as shown in Figure 36.

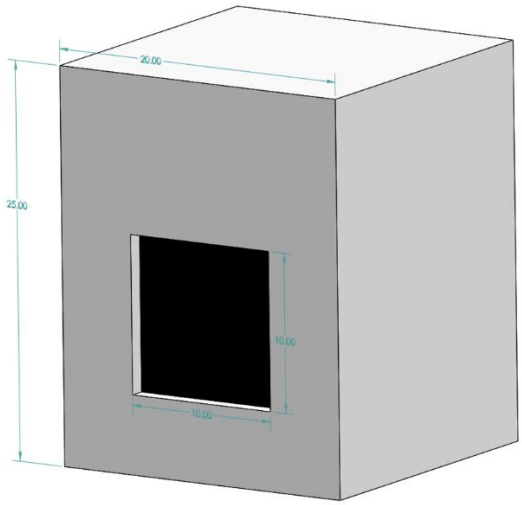

Figure 118. Estimated dimensions of a 100 MWth FPR with a 10m x 10m aperture.

If it is decided to use a single ImageIR8300 camera with a horizontal FOV of 10 m, the camera will need to be placed 104 m away from the aperture which will yield a 15.625 mm pixel size as seen on Table **17**. In order to yield a higher opacity value, we would need to incorporate more IR cameras; however, it is important to keep in mind that each camera is $100,000.

Table 17. IR camera with 100 mm lens used to visualize a 10 m HFOV.

Using a 100 mm lens (FOV: 5.5°x4.4°)
$H = 10{,}000mm$ $V = 8{,}000mm$ $PS = \frac{10{,}000mm}{640px} = 15.625\frac{mm}{px}$ $\omega = \frac{\pi x 140^2}{15625^2} = 0.025\%$

Accounting for the total cost of a camera or a set of cameras, we propose to use a larger array of FLIR One Pro IR (160 x 120 resolution) cameras. Each of these cameras costs $400 and will require a special integration within Android to operate and stitch together the individual thermograms from the IR camera array. Placement of these IR cameras is crucial as they can cover approximately 1 meter of the aperture if they are place 1 meter away from the aperture (Table 18). In this case, we could arrange 10 of them to cover the 10 meters of the aperture if they can be placed about 1 meter away from the aperture.

Although this can pose a challenge with the spilled heat flux, it can yield better results comparing the FOV of the cameras as seen in Figure 119. In terms of distance away from the aperture, the ImageIR8300 will cover 8 meters, while the FLIR One Pro covers less than 1 meter. We believe this is a more affordable and efficient alternative.

Table 18. IR camera with 100 mm lens used to visualize a 10 m HFOV.

Using a FLIR One Pro (FOV: 55°x43°))
$H = 1{,}000mm$ $V = 750mm$ $L = \frac{1{,}000mm}{2xtan(27.5°)} = 960.5mm$ $PS = \frac{1{,}000mm}{160px} = 6.25\frac{mm}{px}$ $\omega = \frac{\pi x 140^2}{6250^2} = 0.158\%$

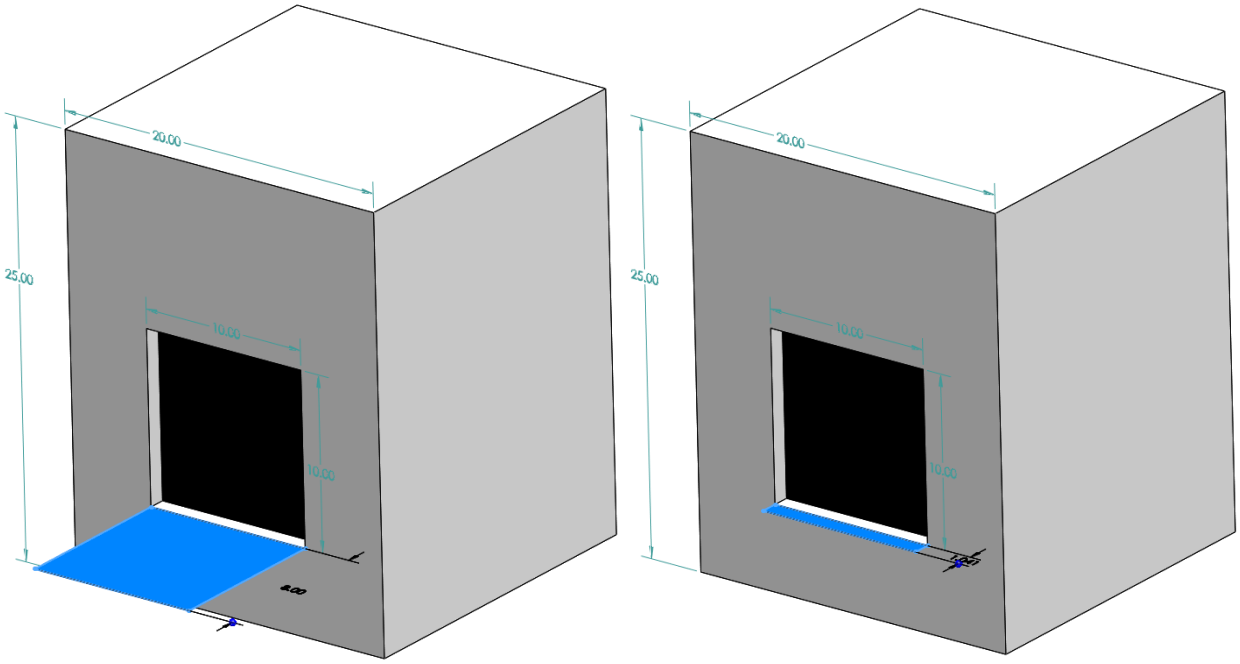

Figure 119. Comparison of FOV based on the camera system used. Left: ImageIR8300. Right: FLIR One Pro array.

ImageIR8300 w/100 mm lens (640 x 512) FLIR One Pro (160 x 120)

Figure 120. IR Cameras consider for the scaled-up system.

In terms of the visible-light camera, the Nikon D3500 can be used in an array to cover the 10 m aperture size. We have two options in terms of configuration. If we want to use a single camera to capture the aperture size, using the same relationship of Figure 117, we can see that it yields a pixel size of 1.667 mm. On the other hand, if we want to limit the maximum pixel size to be equal to the nominal particle diameter, each camera has a horizontal FOV of 1.68 m; this will require 6 cameras to cover the 10 m aperture. Even employing 6 cameras, at $500 apiece, it will only be $3000 total. Combinations of focal length with camera distance from aperture are summarized in Table 19.

Table 19. Configuration of the Nikon camera used for the scaled-up system.

If H = 10,000 mm (single camera)	If PS = 0.28 mm/px
$PS = \frac{H}{6000px} = \frac{10{,}000mm}{6000px} = 1.667\frac{mm}{px}$ $V = PSx4000px = 1.667\frac{mm}{px}x4000px = 6666.7mm$ $L = \frac{H}{23.343}xFL = 428.4xFL$ For a FL = 18 mm, L = 7,711.2 mm For a FL = 55 mm, L = 23,562 mm For a FL = 70 mm, L = 29,988 mm For a FL = 300 mm, L = 128,520 mm	$H = 0.28\frac{mm}{px}x6000px = 1{,}680mm$ $V = PSx4000px = 0.28\frac{mm}{px}x4000px = 1{,}120mm$ $L = \frac{H}{23.343}xFL = 71.97xFL$ For a FL = 18 mm, L = 1,295.5 mm For a FL = 55 mm, L = 3,958.4 mm For a FL = 70 mm, L = 5,037.9 mm For a FL = 300 mm, L = 21,591 mm

Finally, two configurations are shown in Figure 121. The first one used only the ImageIR8300 camera along with the Nikon D3500 with 70-300 mm lens mounted together with a very similar FOV. The cost for the cameras on this configuration will be ~$100k only accounting for the equipment. In the second case, a novel configuration with a better resolution could address some of the issues of mounting the cameras 100+ meters away from the aperture. In this case, we can mount 10 FLIR One Pro cameras along with 2 Nikon cameras with a 10-20 mm lens. The total cost for the equipment will be in the range of ~$4k.

Cameras jointly mounted to maintain a similar FOV. ImageIR8300 with 100 mm lens and Nikon D3500 with 240 mm Focal length.

Cameras mounted separately to maintain a similar FOV. 10 FLIR One Pro and 2 Nikon D3500 with 16 mm Focal length.

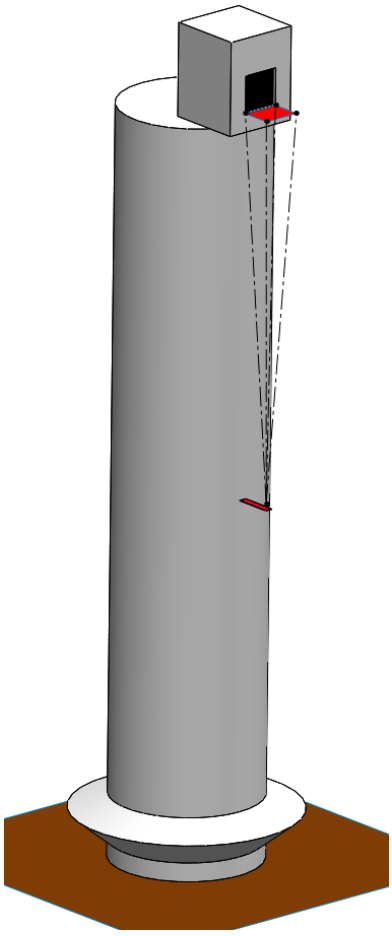

Cameras located 104m away from the aperture with a 10m x 8m FOV.

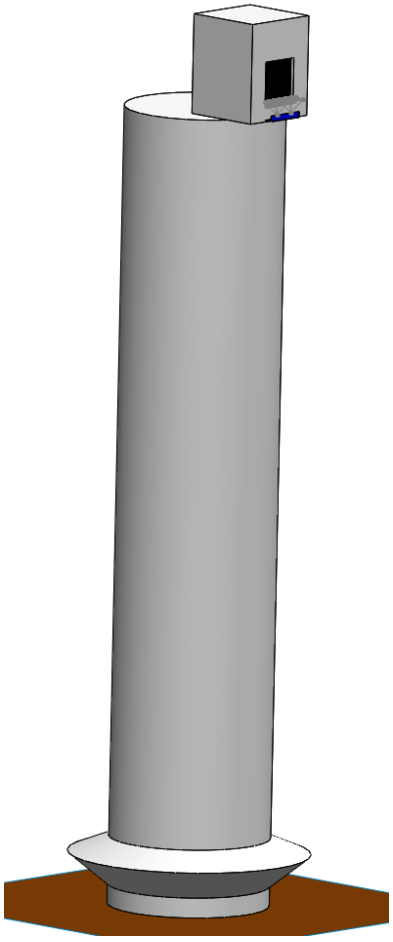

Cameras located 1-3m away from the aperture with a 10m x 3m FOV.

Figure 121. Configurations of cameras with respect to the 100 MWth FPR mounted on 200-meter tower. Left: Configuration with a single IR and Visible-light cameras. Right: Configuration with a 10 IR and 2 Visible-light cameras.

7. CONCLUSION AND RECOMMENDATIONS

7.1. Particle Imaging

A particle imaging technique to estimate the particle egress rate and corresponding advective heat losses has been developed. The temperatures and mass flow rate estimated using the IR camera and Matlab software have been compared with the lab-scale and on-sun experiments. Results and Matlab scripts are publicly available at this web site.

While there are some discrepancies with some estimates, we believe that these variations are due in part to some measurement errors during the high-temperature experiments. Nonetheless, this post-processing methodology provides a fundamental step towards the development of a real-time in-situ monitoring technique. The technique was evaluated using both CARBO ceramic beads and sand in lab-scale tests, and CARBO beads during on-sun tests. An analysis of variance was performed on a number of on-sun tests that revealed that average particle temperature was the most significant parameter correlated to particle egress from the open aperture. The interactions of wind speed with heat flux, wind speed and particle temperature, and particle mass flow rate and wind direction were also found to be statistically correlated to particle egress.

While the current version of the post-processing script has been completed, there are some suggested additions that may improve the accuracy of the methodology:

- Verify and validate the effect of any reflected emissions from the particles for hot-flow experiments
- Validate the influence of the incident heat flux on the particle curtain and plume
- Introduce the error propagation estimation on the mass flow rate calculation
- Introduce error propagation on the total time-dependent plots

Similarly, the team recommends the introduction of a camera which is able to match the sampling frequency of the IR camera. This will provide an image-to-image calculation which can reduce the number of samples required and the amount of time to post-process the data as more discrete samples can be selected instead of collecting data during specific time intervals.

Lastly, the team has recommended imaging and characterization systems and methods that can be implemented for larger commercial systems with lower-cost imaging equipment (see Section 6).

7.2. Particle Sampling

Particle sampling methods were deployed during on-sun tests to record near-field (several meters) and far-field (tens to hundreds of meters) concentrations of aerosol particles within emitted plumes. The objective was to quantify the particulate emission rates and loss from the falling particle receiver in relation to OSHA and EPA National Ambient Air Quality Standards (NAAQS). Near-field instrumentation placed on the platform in proximity to the receiver aperture included several real-time aerosol size distribution and concentration measurement techniques, including a TSI Aerodynamic Particle Sizers (APS), TSI DustTraks, Portable Optical Particle Spectrometers (POPS), Alphasense Optical Particle Counters (OPC), Condensation Particle Counters (CPC), Cascade Particle Impactors, 3D-printed prototype tipping buckets, and meteorological instrumentation. Far-field particle sampling techniques utilized multiple tethered balloons located upwind and downwind of the particle receiver to measure the advected plume concentrations using a suite of airborne aerosol and meteorological instruments including POPS, CPCs, OPCs and cascade impactors. The

combined aerosol size distribution for all these instruments spanned particle sizes from 0.02 μm – 1000 μm. Results showed a strong influence of wind direction on particle emissions and concentration.

The TBS deployment allowed for the far-field detection of aerosol concentrations away from the solar tower receiver. The location of the balloons was based on the predicted prevailing winds and observed winds during the study. Two configurations of the solar aperture were considered during the study periods. A summary of the data is discussed below:

7.2.1. One-Stair – November 3, 2020

The data from the CPC instruments show that the aerosol concentration of smaller particles (0.01μm to 1.0 μm), is lower for the downwind location when compared to the upwind location. The mid-range particle sizes measured by the POPS show a general 30% higher concentrations when compared to the upwind monitors which increases to 100% higher concentrations during a period between 12:30 and 13:30. This increase in concentration is likely due to the instruments measuring increased aerosol concentrations from the advected plume originating from the aperture.

The OPC measurements also show higher concentrations of downwind aerosol measured at the Downwind 1 location compared to the upstream instrument, particularly in the period between 12:30 and 13:30. The increase in aerosol concentration during this period is observed at particle sizes less than 1.5 μm as measured by the OPC which is consistent to the POPS data.

The near field measurements of very large particles as measured by the tipping buckets also show an increased mass loading of 130x for the one-stair configuration compared to the free-fall configuration.

The concentrations measured by the near-field OPC instruments also show negligible concentrations when compared to the PEL values under the free-fall and one-stair aperture conditions.

7.2.2. Free-Fall (No Stair) – March 7, 2021

During the free-fall study the CPC data showed a consistent trend to the one-stair dataset with concentrations of small particles (0.01μm to 1.0 μm) lower than the measured concentrations at the upwind balloon. Based on SEM analysis of STAC impactor measurements, the composition of these particles are carbonaceous in nature and are likely a product of secondary organic aerosol (SOA) formation. The mid-range particle sizes measured by the POPS upwind and downwind show similar concentrations for most of the experimental period with a few isolated elevated events. The OPC data shows similar concentration profiles at both the upstream and downstream locations during the measurement period.

Based on OPC measurements the estimated $PM_{2.5}$ concentrations under the free-fall condition is an order of magnitude lower than the one-stair configuration. However, under both scenarios the observed concentrations for $PM_{2.5}$ and PM_{10} are well under the significant impact levels utilized in regulatory air dispersion modeling. The concentrations measured by the near-field OPC instruments also show negligible concentrations to the PEL values under the free-fall and one-stair aperture conditions.

REFERENCES

[1] Ho, C.K., 2016, A Review of High-Temperature Particle Receivers for Concentrating Solar Power, *Applied Thermal Engineering*, **109**(Part B), p. 958-969.

[2] Ho, C.K., J.M. Christian, J. Yellowhair, S. Jeter, M. Golob, C. Nguyen, K. Repole, S.I. Abdel-Khalik, N. Siegel, H. Al-Ansary, A. El-Leathy, and B. Gobereit, 2017, *Highlights of the High-Temperature Falling Particle Receiver Project: 2012 - 2016*, in *SolarPaces 2016: International Conference on Concentrating Solar Power and Chemical Energy Systems*, Abu Dhabi, UAE, October 11 - 14, 2016. <Go to ISI>://WOS:000380374600050.

[3] Ho, C.K., J.M. Christian, J. Yellowhair, N. Siegel, S. Jeter, M. Golob, S.I. Abdel-Khalik, C. Nguyen, and H. Al-Ansary, 2015, *On Sun Testing of an Advanced Falling Particle Receiver System*, in *SolarPACES 2015*, Cape Town, South Africa, October 13 - 16, 2015.

[4] Ho, C.K., J.M. Christian, J. Yellowhair, N. Siegel, S. Jeter, M. Golob, S.I. Abdel-Khalik, C. Nguyen, and H. Al-Ansary, 2016, On-Sun Testing of an Advanced Falling Particle Receiver System, *Solarpaces 2015: International Conference on Concentrating Solar Power and Chemical Energy Systems*, **1734**.

[5] Ho, C.K., J.M. Christian, J.E. Yellowhair, K. Armijo, W.J. Kolb, S. Jeter, M. Golob, and C. Nguyen, 2019, On-Sun Performance Evaluation of Alternative High-Temperature Falling Particle Receiver Designs, *Journal of Solar Energy Engineering-Transactions of the Asme*, **141**(1).

[6] Ho, C.K., S. Kinahan, J.D. Ortega, P. Vorobieff, A. Mammoli, and V. Martins, 2019, *Characterization of Particle and Heat Losses from Falling Particle Receivers*, in *Proceedings of the ASME 2019 13th International Conference on Energy Sustainability*, ES2019-3826, Bellevue, WA, July 15 - 18, 2019.

[7] Schroeder, N.R. and C.K. Ho, 2020, *Ceramic Proppant Dust Generation in Falling Particle Receiver Applications*, in *SolarPACES 2020*, Virtual, September 28 - October 2, 2020.

[8] Ho, C.K., N.R. Schroeder, H.F. Labuscher, L. Yue, B. Mills, R. Shaeffer, J.M. Christian, and K.J. Albrecht, 2020, *Receiver Design and On-Sun Testing for G3P3-USA*, in *SolarPACES 2020*, Virtual, September 28 - October 2, 2020.

[9] Kim, K., N. Siegel, G. Kolb, V. Rangaswamy, and S.F. Moujaes, 2009, A study of solid particle flow characterization in solar particle receiver, *Solar Energy*, **83**(10), p. 1784-1793.

[10] Ho, C.K., J.M. Christian, D. Romano, J. Yellowhair, N. Siegel, L. Savoldi, and R. Zanino, 2017, Characterization of Particle Flow in a Free-Falling Solar Particle Receiver, *Journal of Solar Energy Engineering-Transactions of the Asme*, **139**(2).

[11] Mills, B. and C.K. Ho, 2018, *Simulation and Performance Evaluation of On-sun Particle Receiver Tests*, in *SolarPACES 2018*, Cassablanca, Morocco,

[12] Mei, F., G. McMeeking, M. Pekour, R.-S. Gao, G. Kulkarni, S. China, H. Telg, D. Dexheimer, J. Tomlinson, and B. Schmid, 2020, Performance Assessment of Portable Optical Particle Spectrometer (POPS), *Sensors (Basel, Switzerland)*, **20**(21), p. 6294.

[13] Ho, C.K. and C.A. Pattyn, 2019, *Investigating Environmental Impacts of Particle Emissions from a High-Temperature Falling Particle Receiver*, in *SolarPACES 2019*, Daegu, South Korea, October 1 - 4, 2019.

[14] Ho, C.K., S. Kinahan, J.D. Ortega, P. Vorobieff, A. Mammoli, and V. Martins, 2019, *Characterization of Particle and Heat Losses from Falling Particle Receivers*, in *Proceedings of the ASME 2019 13th International Conference on Energy Sustainability, ES2019-3826*, Bellevue, WA, July 15 - 18, 2019, Bellevue, WA, USA.

APPENDIX A. PROJECT INFORMATION

Agency/Office/Program	DOE/EERE/Solar Energy Technology Office	
Award Number	Gen3 CSP Lab Support (CPS #33869)	
Project Title	Characterization of Radiative, Convective, and Particle Losses in High-Temperature Particle Receivers	
Principal Investigator	Clifford K. Ho, Sr. Scientist, (505) 844-2384, ckho@sandia.gov	
Business Contact	Andrew Kassir, (505) 844-7534, akassir@sandia.gov	
Submission Date	5/4/2021	
Recipient Organization	Sandia National Laboratories	
Project Period	**Start:** 3/1/2018	**End:** 5/31/2021
Project Budget	$1,031,070.00	

APPENDIX B. MILESTONE SUMMARY AND PERFORMANCE EVALUATION CRITERIA

Table 20. Summary of milestones.

I. Major Task/Milestone Schedule							
SOPO Task # M.S. #	Task Title and Milestone Description	Performer	Task Start Date	Milestone Completion Date			Progress Notes
				Original	Actual	Percent Complete	
Year 1							
1.2	Imaging tool / design acceptance						
M1.1	Design and acceptance of Measurement tools and operational set up	UNM/SNL	3/1/18	5/31/18	5/31/18	100%	Completed table of requirements and camera specifications
1.3,1.4	Demonstration of imaging-based methods in lab tests						
M1.2	Tool calibration and particle loss measurement	UNM	6/1/18	2/28/19	5/31/20	100%	Completed suite of hot-flow tests for evaluation of particle-imaging method and algorithm.
2.1	Deployment of tower-top air monitoring station and ground-based air monitoring stations						
M2.1	Build and deploy air monitoring system using existing methods	SNL	3/1/18	2/28/19	2/28/19	100%	Completed tests using particle sampling instruments during on-sun tests (ahead of schedule). Evaluated measurement methods and documented in ASME paper.
Year 2							
1.5	Deployment of in-situ imaging system at tower top and on-sun commissioning						
M1.3	Measurement of particle and convective losses in on-sun environment over range of conditions	SNL/UNM	3/1/19	8/31/19	3/31/21	100%	Began collecting on-sun data in August 2020 and collected on-sun data through fall.
1.3-1.5	Assessment of convective heat loss using in-situ imaging system						
M1.4	Corroboration of convective heat losses with lab tests	UNM/SNL	3/1/19	12/1/19	5/31/21	100%	Validation studies using lab-scale tests will be performed in BP2 Q4 and Q5. Solar simulator tests were halted due to COVID-19 but may resume after on-
1.6	Scaling of imaging methods to 100 MWe plant						
M1.5	Develop designs for using the imaging methods on a 100 MWe plant	UNM/SNL	3/1/19	12/1/19	7/31/20	100%	Commercial-scale implementation and designs for particle imaging system were developed in BP2 Q3 - Q5.
2.2	Modeling of particle dispersion in air						
M2.2a	Develop models of particle dispersion in air with comparison to EPA standards. Assess impact of wind and plant-operation duration on particle concentration and DNI.	SNL	3/1/19	2/28/20	5/31/19	100%	Added 3/5/19. Models of particle dispersion in air have been performed using both CFD and EPA's preferred model, AERMOD. Results have been obtained and are being published in a SolarPACES 2019 paper.
2.2b	Collection and analysis of samples during on-sun in tests						
M2.2b	Perform test in high-fidelity environment. Compare results to safety standard	SNL	3/1/19	2/28/20	3/31/21	100%	The results of the models in M2.2a will inform locations for sampling during next on-sun tests. If the results of the sampling at these locations is equal to or less than the model results that yield acceptable concentrations per EPA metrics, the particle emissions will be deemed acceptable. In BP2Q5, we worked with staff in Sandia's aerosol sciences group to design and prepare particle-sampling equipment. In BP2Q6, we collected data during on-sun tests. In the spring of 2021, we plan on completing the tethered balloon testing.
1.6	Public dissemination of results for use in Gen 3						
M1.5	Information retained in transferable manner (Report, publication, etc)	UNM/SNL	3/1/19	2/28/20	3/31/21	100%	Published a number of peer-reviewed conference papers from this work.

Table 21. Summary of performance evaluation criteria.

Year # Task# Milestone #	Milestone Name / Description	Criteria	Section Addressed
Y1 T1.2 M1.1	Imaging tool / design acceptance	1. Frame rate and spectral range of visible and IR cameras 2. Detection limits of imaging tools (frame rate, spectral characteristics, resolution, etc.) match requirements to measure both particle losses (1 – 10 kg/hour; up to 5 m/s) and particle temperature (~400 – 750 °C with ~0.9 emissivity) 3. Tabulated comparison of camera specifications against values determined from modeling or past videos of particle velocities (to determine frame rate) and temperatures (to determine spectral range).	3.1

Year # Task# Milestone #	Milestone Name / Description	Criteria	Section Addressed
Y1 T1.3, 1.4 M1.2	Demonstration of imaging-based methods in lab tests	**1**. Lab-based quantification of particle losses using calibrated imaging methods **2.** Slope of parity plot of image-based measurements vs. gravimetric measurements of particles loss is between 0.9 and 1.1 (±10% error) with R ≥ 0.9. **3.** Use parity plot to compare particle-loss measurement methods with particle mass flow rates ranging from ~1 – 10 kg/hour (0.3 – 3 g/s), which was measured in previous on-sun tests, with at least three replicates of 3 different mass flow rates	3.2, 3.3
Y1 T2.1 M2.1	Deployment of tower-top air monitoring station and ground-based air monitoring stations	**1**. Number of tower-top air monitoring stations and ground-based air monitoring stations **2.** At least 1 tower-top and at least 2 ground-based air monitoring stations **3.** Complies with Sandia's Industrial Hygiene department requirements to calibrate and operate systems per NIOSH standards**	4.1
Y2 T1.5 M1.3	Deployment of in-situ imaging system at tower top and on-sun commissioning	**1.** Number of on-sun tests performed with quantification of particle and heat losses **2.** At least 1 on-sun test (mass flow rate ≥ 5 kg/s; irradiance ≥ 500 suns; T_{in} ≥ 550 °C) with measurement of particle and convective losses **3.** Measured particle and convective heat losses are commensurate with expected trends based on results from past tests and models, wind conditions, and particle mass flow rate	3.4
Y2 T1.3-1.5 M1.4	Assessment of convective heat loss using in-situ imaging system	**1.** Comparison between in-situ measured and expected† convective heat loss **2.** Slope of parity plot of measured vs. expected† heat loss is between 0.8 and 1.2 (± 20%) for different parameter values impacting convective heat loss (e.g., particle mass flow rate, wind). **3.** Parity plot of measured vs. predicted convective heat losses. Compare measured convective heat loss using imaging methods with at least two different mass flow rates while keeping the particles at the same temperature; evaluate expected change in convective heat loss vs. mass flow rate (and other parameters) using CFD. Evaluations can be done at both the lab-scale and on-sun †Expected values can be measurements derived from lab tests and from CFD simulations for on-sun tests.	3.4

Year # Task# Milestone #	Milestone Name / Description	Criteria	Section Addressed
Y2 T1.7 M1.6	Scaling of imaging methods to 100 MW_e plant	**1.** Design criteria for imaging methods to be used on 100 MW_e particle receiver including focal distance, field of view, resolution, and number of cameras to be used **2.** Established design criteria for cameras shall be met by commercially available cameras **3.** Present designs for 100 MW_e particle receiver and illustrate how imaging methods will be used. Include specifications from commercially available cameras.	6
Y2 T2.2 M2.2a	Modeling particle emissions and dispersion in air	**1.** Comparison of modeling results to EPA standards and impact on DNI with wind speeds ranging from 2 – 10 m/s **2.** Results show that particle concentrations will be compliant with EPA National Ambient Air Quality Standards for PM2.5 and PM10 and will not impact DNI on heliostat field by more than 1% **3.** https://www.epa.gov/criteria-air-pollutants/naaqs-table	5
Y2 T2.2 M2.2b	Collection and analysis of samples during on-sun tests	**1.** Collection and analysis of samples during on-sun tests, from a minimum number of tests **2.** Collection and analysis of samples during at least 3 on-sun tests with comparison to acceptable safety standards. **3.** Sampling and analysis will follow NIOSH standards. If safety standards are exceeded, mitigation measures will be implemented.	4.4
Y2 T1.6 M1.5	Public dissemination of results for use in Gen 3	1. Public dissemination of key findings 2. At least one paper is reviewed and accepted for publication 3. Publish results in journal article or conference proceedings that show in-situ imaging methods can be used to quantify particle and convective heat losses from directly irradiated particle receivers	Appendix D. List of Publications from this Work

APPENDIX C. BUDGET SUMMARY

As of May 2021

III. Spending Summary by Budget Category							
	Approved Budget per SF-424A				Actual Expenses		
Budget Categories per SF-424a	**BP 1**	**BP 2**	**BP 3**	**Total**	**This Quarter**	**Cumulative**	**%**
a. Personnel	$ 122,522	$ 94,899	$ -	$ 217,421	$ 15,506	$ 163,496	75.20%
b. Fringe Benefits	$ -	$ -	$ -	$ -		$ -	0.00%
c. Travel	$ -	$ 8,689	$ -	$ 8,689		$ 400	4.60%
d. Equipment	$ -	$ -	$ -	$ -		$ -	0.00%
e. Supplies	$ 127,393	$ 17,377	$ -	$ 144,770	$ 565	$ 139,510	96.37%
f. Contractual	$ 141,145	$ 102,544	$ -	$ 243,689	$ 28,835	$ 308,790	126.71%
g. Construction	$ -	$ -	$ -	$ -		$ -	0.00%
h. Other	$ 23,731	$ 15,883	$ -	$ 39,614		$ 19,845	50.09%
i. Total Direct Charges	**$ 414,791**	**$ 239,392**	**$ -**	**$ 654,183**	**$ 44,905**	**$ 632,041**	**96.62%**
j. Indirect Charges	$ 216,705	$ 160,182		**$ 376,887**	$ 23,143	$ 311,361	82.61%
k. Total Charges	**$ 631,496**	**$ 399,574**	**$ -**	**$ 1,031,070**	**$ 68,048**	**$ 943,402**	**91.50%**
DOE Share	$ 631,496	$ 399,574	$ -	$ 1,031,070	$ 68,048	$ 943,402	91.50%
Cost Share	$ 6,375	$ 6,375	$ -	$ 12,750	$ -	$ 12,750.00	100.00%
Cost Share Percentage	1.0%	1.6%	0.0%	1.2%	0.0%	1.4%	1.35%

APPENDIX D. LIST OF PUBLICATIONS FROM THIS WORK

Full Author List	"Article Title"	Paper Number	Conference/ Proceedings Title	Conference Location	Dates
Jesus Ortega, Peter Vorobieff, Andrea Mammoli, Clifford Ho	Characterization of particle and heat losses of a lab-scale solid particle receiver.	-	APS Division of Fluid Dynamics Conference 2018	Atlanta, Georgia	November 18-20, 2018
Clifford Ho, Sean Kinahan, Jesus Ortega, Peter Vorobieff, Andrea Mammoli, Vanderlei Martins	Characterization of particle and heat losses from falling particle receivers.	ES2019-3826	ASME Energy and Sustainability Conference 2019	Bellevue, Washington	July 14-17th 2019
Clifford K. Ho and Christian Pattyn	Investigating Environmental Impacts of Particle Emissions from a High-Temperature Falling Particle Receiver	-	SolarPACES 2019	Daegu, South Korea	October 1 – 4, 2019
Guillermo Anaya, Jesus Ortega, Irma Vazquez, Adrian Cederberg, Peter Vorobieff, Clifford Ho	Velocity vector field extraction from high speed thermograms through particle image velocimetry tools.	-	APS Division of Fluid Dynamics Conference 2019	Seattle, Washington	November 23-26 2019
Jesus Ortega, Guillermo Anaya, Irma Vazquez, Adrian Cederberg, Peter Vorobieff, Clifford Ho	Particle temperature extraction from thermograms and mass flow measurements.	-	APS Division of Fluid Dynamics Conference 2019	Seattle, Washington	November 23-26 2019
Jesus Ortega, Guillermo Anaya, Peter Vorobieff	Bulk Velocity Extraction from Time-Resolved Thermogram Sequences through PIVlab	-	UNM STEM Symposium 2020	Albuquerque, NM	February 29, 2020
Jesus Ortega, Guillermo Anaya, Peter Vorobieff	Particle Curtain Temperature Estimation Using Imaging Methods	-	UNM STEM Symposium 2020	Albuquerque, NM	February 29, 2020
Jesus Ortega, Guillermo Anaya, Peter Vorobieff, Gowtham Mohan, Clifford Ho	Imaging Particle Temperatures and Curtain Opacities Using an IR Camera	ES2020-1688	ASME Energy and Sustainability Conference 2020	Virtual, Online	June 16-18, 2020
Ortega, J.D., C.K.Ho, G. Anaya, P. Vorobieff, G. Mohan	A Non-Intrusive Particle Temperature Measurement Methodology using Thermogram and Visible-light Image Sets	ES2021-63791	Proceedings of the ASME 2021 15th International Conference on Energy Sustainability	Virtual	June 16-18, 2021
Ortega, J.D., C.K.Ho, G. Anaya, P. Vorobieff, G. Mohan	Particle Plume Velocities Extracted from High-Speed Thermograms through Particle Image Velocimetry	ES2021-63336	Proceedings of the ASME 2021 15th International Conference on Energy Sustainability	Virtual	June 16-18, 2021
Glen, A., D. Dexheimer, A. Sanchez, C.K. Ho, S. China, F. Mei, N. Nahar	Near-Field and Far-Field Sampling of Aerosol Plumes to Evaluate Particulate Emission Rates from a Falling Particle Receiver During On-Sun Testing	ES2021-63466	Proceedings of the ASME 2021 15th International Conference on Energy Sustainability	Virtual	June 16-18, 2021

DISTRIBUTION

Email—Internal

Name	Org.	Sandia Email Address
Technical Library	01977	sanddocs@sandia.gov

Sandia
National
Laboratories